UNIVERSITÉ DE MONTRÉAL

24 GHZ FREQUENCY MODULATION CONTINUOUS WAVE
RADAR FRONT END SYSTEM ON SUBSTRATE

ZHAOLONG LI

DÉPARTMENT DE GÉNIE ÉLECTRIQUE

ÉCOLE POLYTECHNIQUE DE MONTRÉAL

THÈSE PRÉSENTÉE EN VUE DE L'OBTENTION

DU DIPLÔMEDE DE PHILOSOPHIAE DOCTOR (Ph.D.)

(GÉNIE ÉLECTRIQUE)

Canada

UNIVERSITÉ DE MONTRÉAL

ÉCOLE POLYTECHNIQUE DE MONTRÉAL

Cette thèse intitulée :

24 GHZ FREQUENCY MODULATION CONTINUOUS WAVE
RADAR FRONT END SYSTEM ON SUBSTRATE

Présenté par: ZHAOLONG LI

en vue de l'obtention du diplôme de: PHILOSOPHIAE DOCTOR (Ph. D.)

a été dûment accepte par le jury d'examen constitué de :

M. CHRISTOPHE CALOZ, Ph. D., président

M. KE WU, Ph. D., membre et directeur de recherche

M. CEVDET AKYEL, D. Sc. A., membre

M. FRANÇOIS GAGNON, Ph. D., membre externe

M. L'HOCINE YAHIA, Ph. D., représentant du doyen

To my families.

ACKNOWLEDGEMENT

I would like to thank all the people who have helped me to complete my thesis.

Most of all, I want to express my deepest gratitude to my advisor, Professor Ke Wu, for his guidance, support and patience leading to the completion of this thesis. His decision of accepting me as his student has opened a new world to me. His inspiring ideas and valuable suggestions shaped my thoughts and his generous support and encouragement in all aspects will benefit me for a lifetime. All in all, this thesis would not be possible without his persistent help. Spending past years doing research under his supervision is one of the best times in my life.

I thank my other committee members, Professor Cevdet Akyel, Professor Christophe Caloz and Professor Francois Gagnon for reviewing my thesis and giving me valuable comments, as well as Professor Renato Bosisio and Professor Mathieu Bourry for being on my qualification examination committee.

I appreciate greatly all the help from our technology specialists including Jules Gauthier, Steve Dubé and Roch Brassard, who actually fabricated the prototypes in this work; Jean-Sébastien Décarie and Ginette Desparois, who successfully maintain the the computer network and the offices.

I thank Professor Jean-Jacques Laurin and Professor Tayeb Denidni for an opportunity to improve my antenna and measurement knowledge.

I also want to thank all the colleagues and friends in Poly Grames, who encouraged me and helped me with my research and life in different aspects.

Finally, I am always grateful to my families and friends both in China and North America, who are always by my side.

RÉSUMÉ

Le but de cette recherche est de mettre en œuvre un système radar «front-end» intégré au substrat à modulation de fréquence à ondes continue (frequency-modulation continuous-wave, FMCW) pour des applications à courte portée. Les principaux éléments de ce travail sont l'intégration et l'interaction entre les différents éléments constitutifs, y compris les antennes, les mélangeurs, les amplificateurs et les diviseurs de puissance.

Une approche hybride d'intégration planaire à non planaire, c'est-à-dire ce qu'on appelle les circuits intégrés au substrat (CIS), est la méthodologie adoptée pour accomplir ce travail. On arrive à la conclusion que la différence géométrique entre les structures guide d'ondes non-planaires, comme les guides d'ondes métalliques classiques, et les structures guides d'ondes planaires, comme les lignes microrubans, n'est plus une restriction de cette stratégie d'intégration. En intégrant différentes structures guide d'ondes sur le même substrat, les mérites des différents modules peuvent être combinés ensemble, tandis que les limites peuvent être éliminées, en partie au moins, sinon totalement. Cette déclaration est justifiée par un mélangeur CIS utilisant une approche d'intégration hybride «surface-volume». En se basant sur les résultats des mesures strictes, il est démontré que le mélangeur CIS a une performance globale supérieure comparativement aux mélangeurs conçus avec une approche d'intégration monotone.

La conception et la mise en œuvre d'un tel système front-end sont étudiées en détail dans ce travail, après l'achèvement d'un radar FMCW utilisant des puces-modules

multiples commerciales. La fonctionnalité du système front-end implémenté ainsi que son application dans un radar FMCW pour les mesures de la portée ont soigneusement été expérimentées.

La conclusion de ce travail est que cette technologie CIS offre une plateforme intégrée, souple, polyvalente et caractérisée par de bonnes performances, une haute densité d'intégration et dont les coûts de fabrication relativement faibles de l'approche système sur substrat pour sont prometteurs pour l'avenir de l'industrie des micro-ondes.

ABSTRACT

The purpose of this research is to implement a completely integrated frequency-modulation continuous-wave (FMCW) radar front-end system-on-substrate (SoS) for short range applications. The main foci of this work are the integration and interaction of various building blocks, including antennas, mixers, amplifiers, and power dividers.

A planar/non-planar hybrid integration approach, i.e. the so-called substrate-integrated-circuits (SICs) is the adopted methodology to accomplish this work. It is concluded that the geometry difference between non-planar waveguiding structures such as classic metallic waveguide, and planar waveguiding structures such as microstrip lines, is no longer distinctive under the roof of this integration strategy. By hybrid integration of different waveguiding structures on the same substrate, the merits of different building blocks can be combined together, while the limitations may be eliminated, partly at least if not completely. This statement is justified by a proposed SICs mixer using a "surface-volume" hybrid integration approach. Based on strict measurement results, this SICs mixer demonstrates superior overall performance compared with mixers designed with a monotonous integration approach.

The design and implementation of such a front-end SoS are investigated in detail in this work, after the completion of an FMCW radar using commercial multiple-chip-modules. The functionality of the implemented front-end SoS as well as its application in a FMCW radar for range measurement are carefully experimented.

The conclusion of this work is that such a SICs technology provides a flexible and versatile integration platform characterized by good performances, high integration-density and relatively low fabrication cost SoS approach for modern and future microwave industry.

CONDENSÉ EN FRANÇAIS

Historique et motivation

Les technologies micro-ondes et en ondes millimétriques sont essentielles pour les futurs systèmes de communication sans fil et les applications électromagnétiques, comme les réseaux haute vitesse pour environnement personnel et les capteurs radars. La technologie du guide d'ondes métallique conventionnel est arrivée à maturité et est largement acceptée par l'industrie. Des composantes performantes sont offertes grâce à cette technologie, notamment pour certaines applications à haut facteur de qualité telles que les antennes, les cavités et les duplexeurs entre autres. Néanmoins, les composantes en guide d'onde sont souvent volumineuses et exigent généralement un usinage précis, ce qui rend l'ensemble des systèmes micro-ondes très chers et leur usage limités à des applications militaires telles que les radars, ou à des applications commerciales très spécifiques telles que les satellites. Au fil du temps, la demande continue de l'industrie pour une plus grande performance des dispositifs, des circuits de taille plus compacte, la baisse des coûts de fabrication ainsi que le développement rapide des demandes du marché civil comme la nécessité d'avoir des radars automobiles à faibles coûts, stimule sensiblement la recherche sur les circuits intégrés monolithiques micro-ondes (monolithic microwave integrated circuits, MMICs). Basée sur les lignes de transmission micro-ondes planaires, cette technologie est bien adaptée à la fabrication à grande échelle. Elle intègre les dispositifs actifs comme les transistors et les diodes sur des matériaux semi-conducteurs. Jusqu'à ce jour, quelques MMICs transmetteurs

intégrés, que ce soit pour des applications radars ou de télécommunications, ont été démontrés.

En examinant l'industrie des micro-ondes, une des applications commerciales importantes est les capteurs radars à courte portée, avec des fonctions typiques comme la mesure du niveau de l'automobile ou le régulateur de vitesse. Toutefois, le déploiement d'un système intégré de hautes performances, à faible coût, produit en masse est tout un travail à réaliser. De nombreuses composantes au facteur de qualité élevé sont difficiles à intégrer à la technologie MMIC, notamment les antennes et les filtres. Beaucoup de ces systèmes sont construits avec une puce intégrée émettrice et des antennes 3D fabriquées séparément, comme l'antenne cornet, la lentille ou l'antenne parabolique. La limite fondamentale du niveau d'intégration du système est que le système d'antennes à haute directivité, haute efficacité et haut gain n'est pas disponible pour les matériaux semi-conducteurs résistifs. Par conséquent, une approche plus pratique consiste à fabriquer une antenne à haute performance séparément et ensuite de la connecter à un transmetteur monolithique par le biais d'une structure permettant la transition planaire à non planaire, comme il est montré à la figure 1.
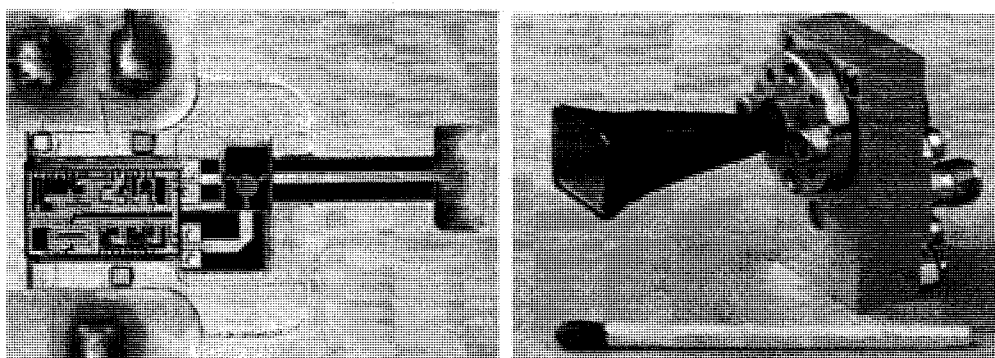

Figure 1. Circuits MMIC avec radar FMCW et antenne cornet externe [8].

Cependant, les transitions nécessaires entre puces MMIC planaires et antennes non planaires compliquent souvent le design et l'installation de l'ensemble du système et aussi augmentent le coût du système, ce qui vient contrer les avantages de l'utilisation des MMICs intégrés. Une approche d'intégration qui combine l'avantage de la technologie des guides d'ondes de posséder un facteur Q élevé et l'avantage de la technologie MMICs de permettre la production de masse, est indispensable pour pousser plus loin l'étude de systèmes micro-ondes.

Afin de répondre à ce problème, les circuits intégrés au substrat (CIS) sont utilisés dans ce travail. L'objectif est de concevoir et de mettre en œuvre un radar frontal intégré au substrat, en utilisant l'approche de l'intégration CIS.

Méthodologie

Cette technologie d'intégration CIS offre une occasion unique d'intégrer des structures à guides d'ondes géométriquement dissemblables de façon uniforme sur un substrat. Le principe de base des CIS est la conception ou la synthèse des structures classiques non planaires sous forme de "circuits planaires", de sorte que les structures planaires et non planaires peuvent être réalisées sur un seul substrat avec les techniques de fabrication existantes. Pour ce faire, les techniques de synthèse du substrat sont utilisées, elles confinent les ondes guidées le long du substrat avec l'aides de canaux métallisés percées dans le substrat ou en utilisant des trous remplis de diélectrique à faible indice de réfraction afin de créer un canal diélectrique grâce au contraste de la constante diélectrique équivalente, comme on peut le voir à la figure 2.
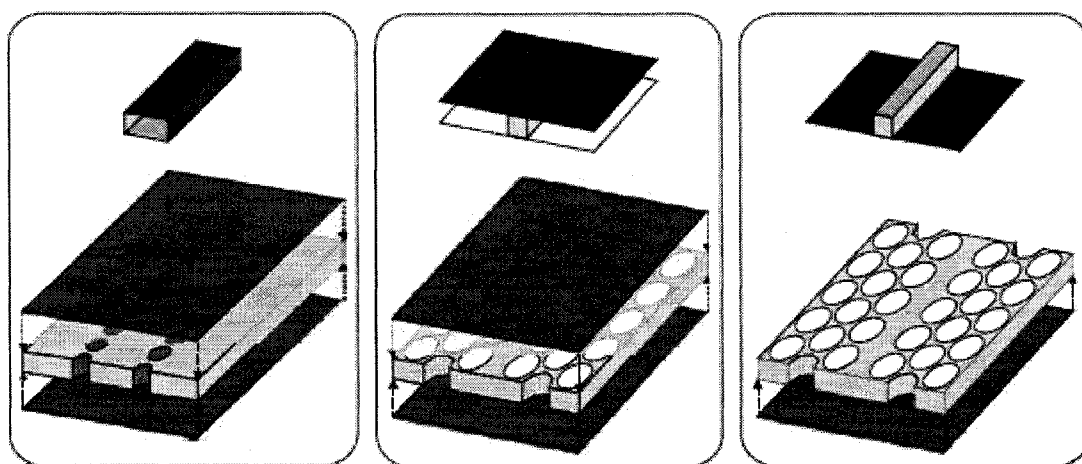
Figure. 2. Exemples du concept des circuits intégrés au substrat. [11]

En agissant de la sorte, certaines structures guides d'ondes non planaires conventionnelles peuvent être intégrées sur seul un même substrat. C'est pourquoi un certain nombre de composantes au facteur Q élevé comme les antennes ou cavités peut être intégrées avec d'autres MICs.

Un membre de la famille des CIS, c'est-à-dire le guide d'ondes intégré au substrat (GIS) est largement utilisé dans ce travail. Puisqu'il y a des similitudes entre les GIS et les guides d'ondes classiques, cette approche d'intégration est très adaptée à la conception d'antennes basées sur les guides d'ondes.

Étapes du projet de recherche –

Conception au niveau du système

Avant de procéder à la conception au niveau des composantes, le système complet est conçu en se basant sur les modèles des «boîtes noires». La topologie du système ainsi

que le système IF doivent être définis en premier lieu, ce qui est le problème fondamental en termes de conception du système. La performance du système désiré résulte de l'interaction entre les différents blocs mis ensemble. Différentes composantes «front-end» sont caractérisées par leurs spécifications individuelles. Pour étudier les interactions multiples entre les différents blocs placés en cascade, l'écart du gain du système en cascade causé par de multiples réflexions dues à l'adaptation imparfaite au port correspondant, doit être pris en compte. Ceci est complété par le calcul de gain net vers l'avant entre les différents modules. En assumant un gain constant pour les deux signaux fondamentaux ainsi que les produits non-linéaires d'intermodulation, le point d'intersection de la non linéarité de troisième ordre est calculé entre deux modules consécutifs. La chaîne complète du système en cascade est obtenue par l'addition de tous les produits non-linéaires ayant passé ce niveau.

Conception au niveau des composantes: les antennes

Différentes solutions d'antennes sont étudiées dans ce travail. Une antenne cornet dans le plan H, présentée à la figure 3, fut le premier prototype de l'antenne pris en considération pour le système radar intégré.
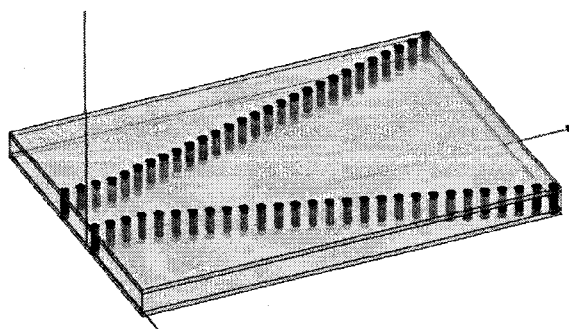
Figure.3. Antenne cornet dans le plan H intégré au substrat. [29]

L'ouverture effective de rayonnement de cette antenne est construite en plaçant une couche de mousse à faible permittivité entre deux couches de substrat. Ainsi, une ouverture de 0.66λ sur plan E peut être formée, et le plan H a une ouverture de 7.21λ. Le principe d'équivalence de Huygens peut être appliqué à l'ouverture à travers la fente afin d'obtenir le courant équivalent sur l'ouverture. La conception de l'antenne est similaire au design d'une antenne cornet classique dans le plan H. L'entrée mesurée S_{11} de l'antenne présente une large bande où l'adaptation est bonne, ce qui s'explique par le fait que cette antenne est presque un guide d'ondes. Le diagramme de rayonnement mesuré démontre une largeur du faisceau à demi-puissance de 16,0 ° dans le plan H et de 59,5 ° dans le plan E. Deux contraintes nous limitent pour ce type d'antenne dans le cas d'une application intégrée «front-end». D'abord, parce que l'antenne est reliée à une alimentation coaxiale à l'aide d'une transition coaxiale guide d'ondes, la véritable source d'alimentation de l'antenne doit être considérée comme un port guide d'ondes, c'est-à-dire une entrée d'alimentation non planaire. L'intégration de cette antenne avec d'autres circuits planaires GIS nécessite une transition GIS guide d'ondes. Cependant, un diagramme de rayonnement large dû à l'étroite ouverture dans le plan E pourrait être un inconvénient pour les applications radars où un faisceau de rayonnement relativement étroit est généralement souhaité afin d'éviter d'encombrer l'environnement.

Pour dépasser ces limites, une antenne cornet pyramidale est proposée, exposée à la figure 4. En raison d'un passage SIW-guide d'ondes nécessaire afin d'assurer l'interconnexion des circuits imprimés SIW avec l'antenne, une ouverture de rayonnement peut être formée par l'évasement continu de l'interface du guide d'ondes,

obtenant ainsi une grande ouverture. Pendant ce temps, puisque que la plupart des circuits micro-ondes et intégrés nécessitent un boîtier métallique, cette structure peut être construite et attachée à l'extérieur de ce boîtier comme la visière d'une casquette, quelle que soit la technologie d'intégration.
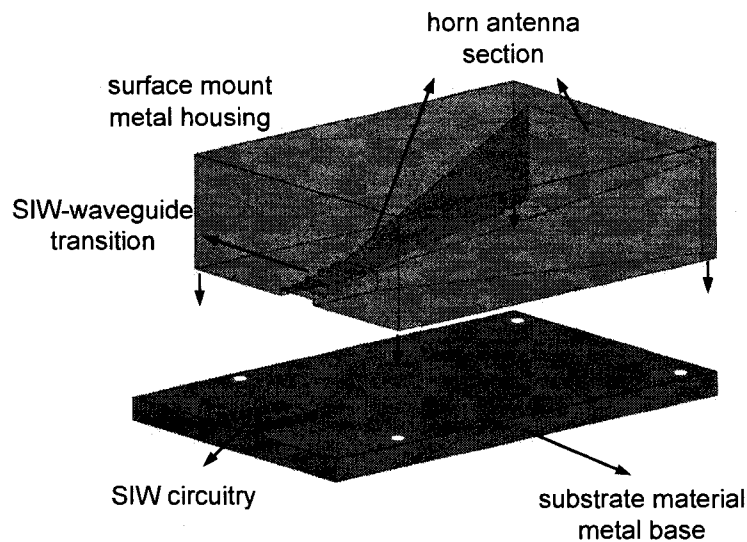

Figure. 4. Antenne cornet pyramidale avec un guide d'ondes SIW à l'entrée [30].

La transition de la technologie GIS au guide d'onde rectangulaire opérant en mode fondamental TE_{10} requiert un transformateur d'impédance quart d'onde en guide d'ondes. Un prototype dos-à-dos de troisième ordre de type Tchebychev est conçu où l'impédance définie par la puissance et le courant est utilisée pour la synthèse de la fonction de transfert.

Bien qu'elle soit adaptée pour une large bande et qu'elle ait de bons diagrammes de rayonnement, cette structure proposée doit toujours faire face au défi de son intégration avec profil planaire «front-end». Si l'objectif de l'intégration au niveau du système

devient une priorité plus élevée, une structure complète GIS avec l'antenne pourrait être une meilleure solution. Un réseau de fentes d'alimentation GIS, présenté à la figure 5, est conçu dans ce travail pour atteindre cet objectif.

Metallized channels

20 mils
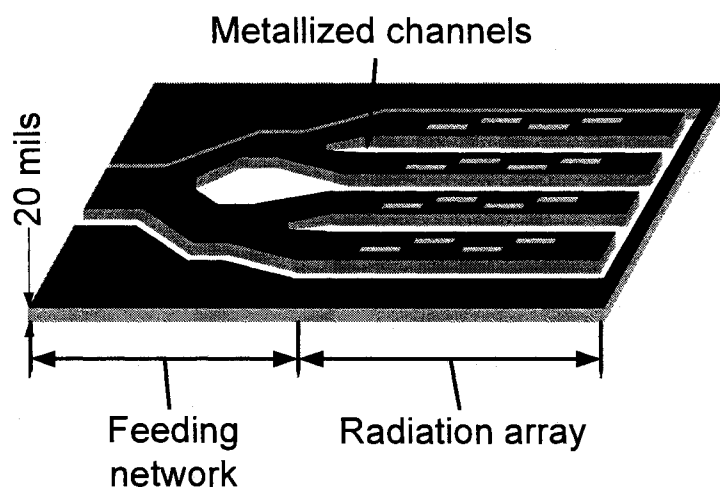
Feeding
network

Radiation array

Figure 5. Réseau d'antennes fentes GIS [72].

La procédure de base de la conception d'un tel réseau de fentes est d'extraire l'information de l'admittance résonante d'une seule fente sur GIS premièrement. Lors de la synthèse du rayonnement, la distribution équivalente des tensions sur chaque élément peut être calculée. Avec pour objectif l'adaptation du port d'entrée, l'admittance exigée de chaque élément peut être aussi obtenue. Par conséquent, l'emplacement et la longueur de la fente peuvent être ainsi déterminés.

Un réseau de fentes GIS qui possède un profil planaire complet est approprié pour un processus de fabrication standard de circuit imprimé. Pour cette raison, cette antenne est choisie finalement comme prototype «front-end». La bande de fréquences des pertes

de retour de 10 dB pour le réseau de fentes GIS est mesurée à 650 MHz, ce qui est suffisant pour les applications radars FMCW. Le diagramme de rayonnement mesuré maintient un seul faisceau directif sur toute la largeur de cette bande de fréquences.

Conception au niveau des composantes: les mélangeurs

En plus de l'antenne intégrée, un autre élément important dans un radar FMCW «front-end» est le mélangeur, c'est-à-dire un convertisseur vers le haut utilisé dans les transmetteurs et convertisseur vers le bas utilisé dans les récepteurs. Deux types de mélangeurs sont proposés dans ce travail. L'un est mélangeur SIW 90 degrés, l'autre est un mélangeur hybride microruban GIS 180 degrés. Le mélangeur 90 degrés GIS, montré à la figure 6, utilise un coupleur ayant un couplage de côté de 3dB comme jonction hybride de puissance. Lorsque les lignes microrubans planaires sont utilisées dans le design d'une jonction hybride de puissance de 3dB, la limite du coupleur est généralement en dessous de 20 GHz. Ceci s'explique par les limites de la taille des circuits à hautes fréquences, où la longueur de la ligne diminue avec l'augmentation de la fréquence, devenant comparable à sa largeur. Par conséquent, les discontinuités de la jonction deviennent dominantes, ce qui se traduit par une baisse du rendement et rend le coupleur microruban à quadrature presque inemployable aux hautes fréquences. Cependant, en utilisant des structures GIS, les fréquences d'opération de cette classe de jonction hybride sont bien étendues dans la gamme des ondes millimétriques.
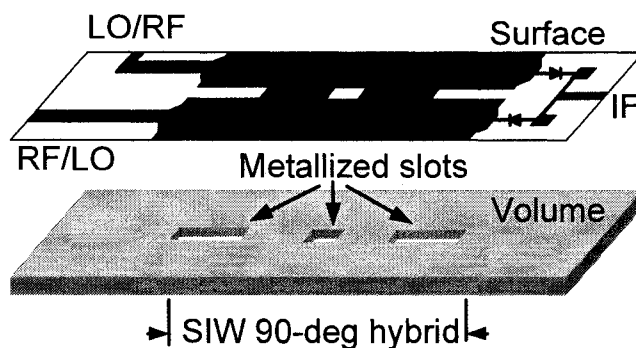
Figure 6. Mélangeur 90 degrés GIS [72].

L'approche de conception est de modéliser les effets de sommation des modes TE10 et TE20 afin de déterminer les décalages de phase de 90 degrés et le couplage de puissance de 3 dB entre des deux ports de sortie (ports 2 et 3) du coupleur. Une paroi capacitive métallisée est positionnée le long de l'ouverture pour compenser la réactance parasite introduite par l'ouverture. Deux diodes Schottky sont utilisées comme jonction de conductance variable dans le mélangeur au lieu des diodes GaAs, afin de fournir des hauteurs de barrière plus basses et un meilleur TOS au port LO. Avec une fréquence RF de 24,1 GHz et une fréquence de l'oscillateur local (LO) de 22,6 GHz, le gain maximal de conversion mesuré à fréquence de -6,7 dB est obtenu.

Pour obtenir une meilleure isolation LO-RF et une meilleure performance du rejet des erreurs, un mélangeur CIS 180 degrés est proposé et illustré à la figure 7. Le design de ce mélangeur CIS est une intégration hybride des GIS et des lignes microrubans conventionnelles. Les ports RF et LO sont conçus à l'aide de SIW tandis que la puissance hybride en phase et hors-phase est obtenue au moyen d'un anneau hybride microruban. L'utilisation de microruban dans ce mélangeur vise essentiellement à

faciliter l'intégration des diodes et de réduire au minimum la taille du circuit entier du mélangeur en même temps. Cela est dû au fait que l'anneau hybride SIW 3dB occupera une superficie du substrat plus grande, ce qui se traduit par un profil de circuit plus large. L'utilisation de la technologie GIS dans les ports RF et LO vise à réduire les pertes associées à la transmission des lignes microrubans à hautes fréquences.
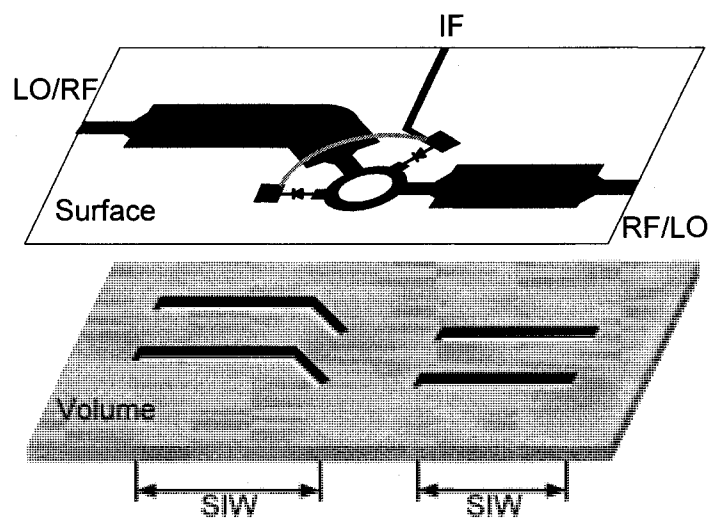

Figure. 7. Mélangeur CIS 180 degrés de surface et de volume [72].

Du point de vue de la fabrication des MICs, la fabrication des lignes de transmission planaires conventionnelles, comme les lignes microrubans, n'implique seulement que la surface du substrat; donc les circuits microrubans peuvent être considérés comme des "circuits de surface". Le processus de fabrication des guides d'ondes synthétisés sous forme planaires, comme la technologie GIS, n'implique pas seulement la surface d'un substrat, mais également la transformation ou la gravure du volume du substrat. Ainsi, les circuits GIS peuvent être considérés comme des "circuits de volume". Englobant la

simplicité d'intégration avec les dispositifs semi-conducteurs tels que les diodes classiques planaires pour les lignes de transmission, tout en exploitant les mérites du facteur Q élevé, le confinement efficace des ondes EM pour les guides d'ondes synthétisés, cette intégration "surface-volume" optimise et maximise l'utilisation du substrat électriquement et matériellement. Par exemple, le mélangeur CIS "surface-volume" devrait avoir un gain de conversion à fréquence plus élevée comparé au mélangeur microruban similaire géométriquement. C'est parce que la totalité de l'enceinte du SIW confinera mieux les ondes EM dans le substrat et donc réduira les inévitables pertes de rayonnement et de transmission typiques des lignes microrubans à hautes fréquences. Cette affirmation est confirmée par les résultats des mesures. Le mélangeur CIS montre une amélioration du gain de conversion d'environ 3 dB par rapport à celui conçu complètement avec des lignes microrubans. Évidemment, cette approche d'intégration hybride surface-volume démontre en effet un rendement supérieur comparé à la conception en utilisant un design monotone. Simultanément, comparé au mélangeur GIS mentionné ci-haut, cette stratégie d'intégration hybride surface-volume nécessite moins de surface du substrat (163,8 mm^2) par rapport au mélangeur GIS (270,0 mm^2), ce qui peut être particulièrement intéressant pour la conception MMIC utilisant des semi-conducteurs GaAs.

Intégration au niveau du système

Différentes composantes GIS ou CIS et dispositifs peuvent être intégrés ensemble sur le même substrat, mais certains problèmes d'intégration uniques aux systèmes intégrés sur un substrat doivent être soigneusement examinés. Par exemple, en tant que membre

de la famille des radars CW, le radar FMCW est également confronté au défi du phénomène de fuite entre l'émetteur et le récepteur qui est inhérent à tout radar CW. Cette fuite pourrait causer de graves problèmes pour le récepteur radar FMCW en saturant le récepteur amplificateur à faible bruit de premier stade ou en dégradant la performance du radar en réduisant la portée dynamique, dépendamment du niveau de puissance de fuite et de l'emplacement de la fuite. C'est pourquoi la plupart des radars FMCW sont limités à des applications à courte portée, où une haute puissance de transmission n'est pas requise et le niveau de puissance de fuite est faible.

Dès que la construction du modèle générique du récepteur radar FMCW homodyne employant un système d'antenne utilisant la technologie GIS fut réalisée, les fuites dans l'espace libre et leurs effets sur les performances du récepteur radar FMCW ont été étudiées dans ce travail. Le niveau de dégradation du ratio signal sur bruit, qui est causé par l'augmentation du niveau de bruit en raison des fuites en espace libre est soigneusement mesuré. La conclusion est qu'avec le niveau de puissance disponible transmissible, les fuites en espace libre seules entraînent une diminution de la sensibilité du récepteur d'environ 10 dB.

Le système complet «front-end» sur substrat est fabriqué sur diélectrique ayant les caractéristiques suivantes : RT6002, ε_r = 2,94 et tanδ = 0,0012 à 10 GHz. Le processus de fabrication est similaire à celui des circuits imprimés classiques. Tout d'abord, les parois latérales du GIS, qui nécessitent une coupure dans le substrat, sont faites. Un laser Nd-YAG à impulsions est utilisé pour remplir cette tâche. Puis, la métallisation de ces parois latérales se fait par pulvérisation d'une fine couche de cuivre suivie d'une

galvanoplastie. Un procédé standard de photolithographie est utilisé dans la phase finale

pour créer le schéma des circuits sur la surface du substrat présenté à la figure 8
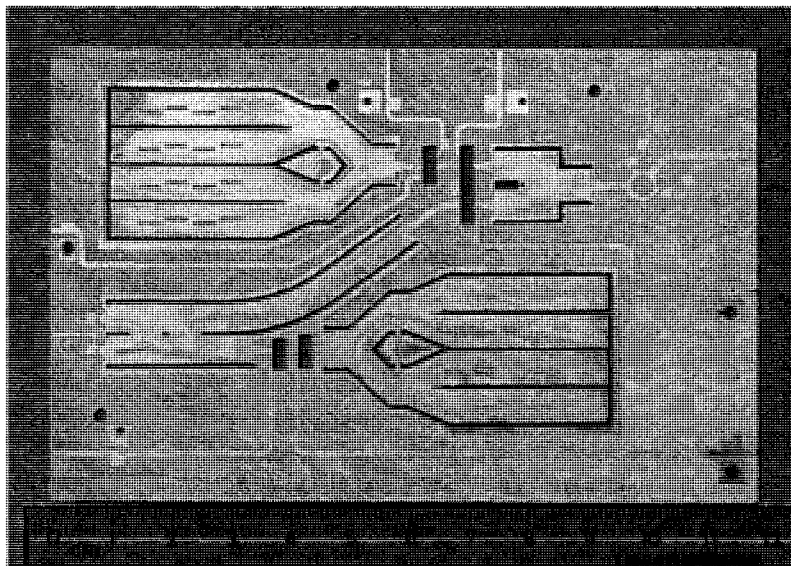

Figure. 8. Circuits imprimés du radar FMCW «front-end» système sur substrat. [72].

Expériences du système radar "front-end"

La fonctionnalité du système front-end seul est vérifiée avant d'être utilisé pour

effectuer des mesures de portée. Parce que l'émetteur et le récepteur du système front-

end sont tous intégrés ensemble, un test individuel n'est pas possible. Toutefois, avec un

signal externe illuminant le système front-end intégré, un signal démodulé de sortie du

récepteur peut être mesuré. La fréquence du signal externe doit être une fonction linéaire

de la sortie démodulée du récepteur IF front-end. C'est pourquoi le signal IF à une

tonalité est appliqué à l'émetteur front-end, le système front-end lui-même est

essentiellement une mesure de la différence de la fréquence entre l'émetteur du signal de

référence et la fréquence du signal externe. Une source externe à balayage de fréquences

est mathématiquement équivalente à changer la distance séparant la cible du front-end. Le résultat des mesures, illustrées à la figure 9, confirme que le système front-end seul fonctionne bien.
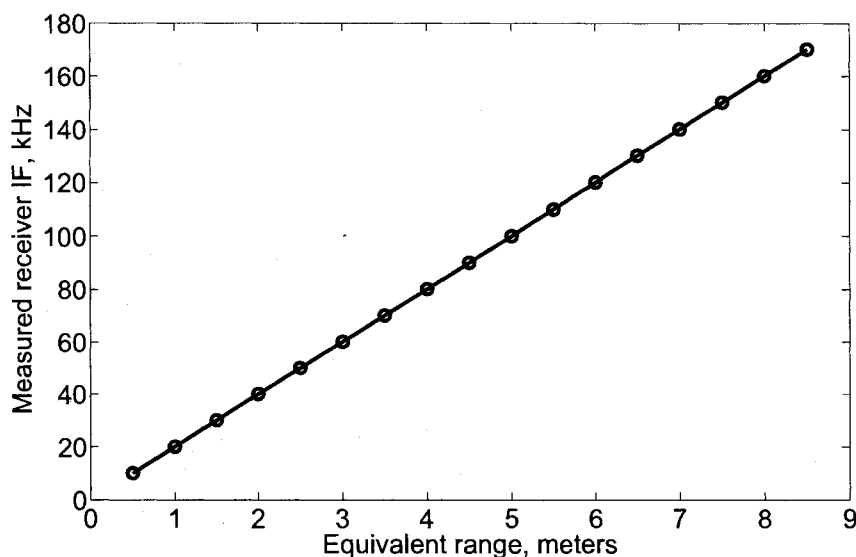

Figure. 9. Mesures des fréquences IF du receveur «front-end» versus la portée de la cible

Pour effectuer les mesures de portée, un signal modulé en fréquence est appliqué à l'entrée du port IF de l'émetteur. Du théorème de Wiener-Khinchine, le signal de l'onde radar retournée est l'inverse de la transformée de Fourier du signal transmis. Par conséquent, pour un signal modulé linéairement en fréquence, le spectre de puissance rectangulaire produira un signal démodulé ayant une distribution d'enveloppe suivant la fonction sinc. Comme la portée de la cible varie, la fenêtre de distance répondra à différentes fréquences conséquemment. Afin de grouper le plus du signal démodulé dans une fenêtre de distance de spectre, les techniques à modulation de fréquences (linear-

frequency-modulation, LFM), y compris des ondes de formes symétriques et asymétriques en dents de scie (triangulaire), montrées à la figure 10, sont utilisées dans ce travail. Ceci est une caractéristique unique des techniques LFM. Un oscillateur VCO externe avec un générateur de fonction est utilisé pour générer le signal FM de base requis. Un réflecteur à angle est utilisé comme station cible placée hors de l'écran radar. La sortie du récepteur SI est filtré avec un filtre passe-bas avant d'être mesuré à l'aide d'un analyseur de spectre. La fréquence du signal à son amplitude maximale est enregistrée, ce qui est relié de façon linéaire à la portée de la cible. La fréquence mesurée du récepteur SI en fonction de la portée de la cible démontre la linéarité du système, ce qui confirme la fonctionnalité du front-end pour un système radar FMCW utilisant des ondes de forme LFM.
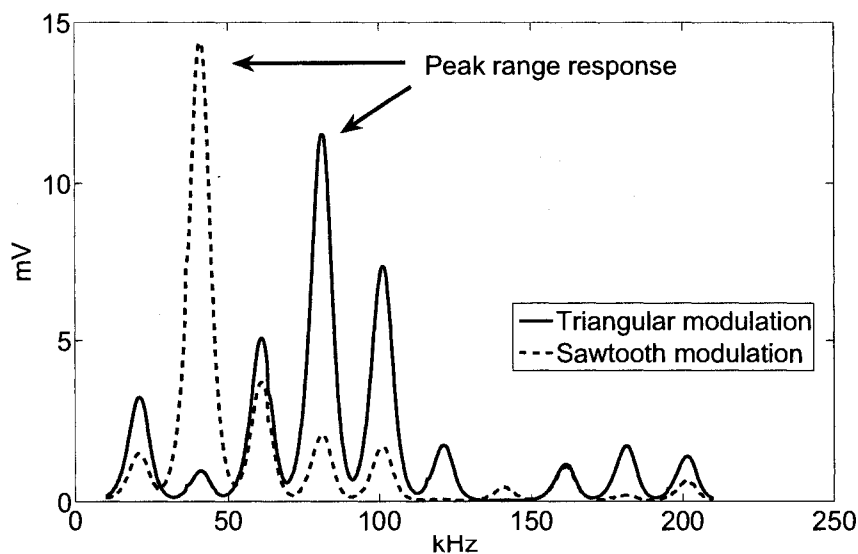

Figure.10. Spectre mesuré de la sortie convertie IF du récepteur pour une cible placée à un 1m avec une fréquence de modulation de 20 kHz.

Enfin, parce que le radar FMCW et le radar à étalement de spectre emploient des techniques de traitement d'auto-corrélation du signal, il est possible de concevoir un système front-end approprié pour les deux radars. En modifiant le signal de base par l'intermédiaire d'un synthétiseur numérique direct, les différentes parties du radar peuvent être réalisées grâce à des logiciels de contrôle. En ce sens, il est possible de dénommer ce type de radar comme défini par logiciel.

Conclusion et travaux futurs

Le concept d'un système sur substrat (*system on substrate*, SoS) radar FMCW intégré front-end a été présenté avec un prototype expérimental. L'application des CIS dans le design des MICs permet une intégration complète au niveau du système. Le SoS intégré est essentiellement un circuit micro-ondes tridimensionnel fait par le biais du processus de fabrication PCB planaire bidimensionnel. Comparée à la technologie monolithique, la stratégie d'intégration hybride proposée offre une possibilité unique d'exploiter les avantages complémentaires de chaque élément tout en éliminant (en partie au moins, si ce n'est complètement) les inconvénients inhérents. Par conséquent, un système complet avec les différentes structures guide d'ondes peut être construit en même temps sur un seul substrat de manière cohérente. En fait, une conception du système CIS n'est pas (et ne devrait pas être) limitée à une seule structure guide d'ondes. Un SoS complexe et polyvalent pourrait également inclure différentes structures guide d'ondes intégrées au substrat, telles que le guide d'ondes diélectrique intégré au substrat non rayonnant, le guide d'ondes intégré substrat, le guide d'ondes image intégré au substrat pour en

nommer quelques-uns, et les structures guidées planaires classiques comme la ligne microruban et le guide d'ondes coplanaire.

LIST OF TABLES

LIST OF FIGURES

LIST OF ABBREVIATIONS

ADC	Analogue-digital converter
ADS	Advanced design system
CW	Continuous Wave
DC	Direct Component
DDS	Direct Digital Synthesizer
FM	Frequency Modulation
HFSS	High Frequency Structural Simulator
HPBW	Half Power Beam Width
IC	Integrated Circuits
IF	Intermediate Frequency
IIP3	Input Intercept Point, 3rd order
IMD	Inter-modulation Distortion
IP3	Intercept Point, 3rd order
LFM	Linear Frequency Modulation
LNA	Low Noise Amplifier
LO	Local Oscillator
P1dB	1-dB Power (compression)
MDS	Minimum Detectable Signal

MDSL	Minimum Detectable Signal Level
MIC	Microwave Integrated Circuits
MMIC	Monolithic Microwave Integrated Circuits
OIP3	Output Intercept Point, 3rd order
PA	Power Amplifier
RF	Radio Frequency
SIC	Substrate Integrated Circuits
SIIG	Substrate Integrated Image Guides
SINRD	Substrate Integrated Nonradiative Dielectric Waveguide
SIW	Substrate Integrated Waveguide
SNR	Signal-to-Noise Ratio
SS	Spread-Spectrum
TOI	Third-Order Interception

TABLE OF CONTENTS

CHAPTER 1 INTRODUCTION

Microwave and millimetre-wave technologies are critical for future wireless systems and electromagnetic applications such as high-speed personal-area networks and radar sensors [1-5]. Conventional metallic waveguide technology is well matured and widely accepted by the industry. Good component performances are offered through this technology, especially for some high quality-factor applications such as antennas, cavities, diplexers and so on. Nevertheless, waveguide components normally are bulky and generally require precision metallic machining, which makes many microwave systems very expensive and mostly limit their usages in military applications such as radars, or very specific commercial applications such as satellites. As time goes on, the continuous demands of the industry for higher performances, more compact size, lower fabrication cost, as well as the rapid development of civil market such as the need for high-speed wireless data connection, significantly stimulate the research on monolithic microwave integrated circuits (MMICs) [6]. Based on planar microwave transmission lines, this technology is well suited for active components such as mixers and amplifiers, where diodes and transistors such as FETs can be integrated conveniently on semiconductor materials. Up to date, some integrated transceiver MMICs, either for sensor applications or for telecommunication applications, have successfully been demonstrated. However, the deployment of a low-cost, mass-producible and high-performance integrated system remains a challenging issue. This is because many high quality (Q) factor components are difficult to get integrated into an MMIC, especially

antennas and filters. Quite often, this class of components are seen as individual building blocks within a microwave system [7, 8]. There has always been a need for an integration approach which can combine the advantage of high-Q owned by non-planar metallic waveguide technology, and the advantage of suitability for mass-production of planar MICs technology.

As an answer to such a specific challenge, the substrate-integrated-circuits (SICs) is widely considered as a potential candidate for the next generation microwave /millimetre-wave integrated circuits integration approach both within research societies as well as industrial communities. Being a new hybrid integration methodology, SICs [9] offers a unique opportunity to integrate geometrical dissimilar waveguiding structures in a uniform manner on a piece of substrate. The basic principle of the SICs is to design or synthesize the conventional non-planar structures in the form of "planar circuits", so that the planar and non-planar structures can be made onto a single substrate with existing manufacturing techniques [10-12]. To do so, substrate synthesis techniques are used, which confine waves guided along substrate with metallised cut-through channels (or vias) on the substrate, or make use of air-filled holes to create an artificial dielectric guiding channel with the contrast of equivalent dielectric constant [12]. The significance of this integration approach is that conventional challenges encountered in planar integration industry can be overcome in an unconventional way by a conventional fabrication process. For example, the classic waveguide cavity structures can be fabricated in a planar profile with more compact profile [13, 14].

A class of substrate integrated waveguiding platforms was developed based on this synthesized integration approach. Some typical examples are the substrate integrated non-radiating dielectric guide (SINRD) [15, 16], the substrate integrated waveguide (SIW) [17, 18], the substrate integrated image guide (SIIG) [19] and so on. Among them, the SIW is the most extensively studied geometry. This could be because the electric field profile of the SIW is most similar to microstrip, a widely adopted planar MICs technology currently. The field transition between these two structures is smooth and low loss over a wide bandwidth. Therefore, it is very convenient to use the SIW in conjunction with other existing planar structures.

As far as the electromagnetic wave propagation mechanisms are concerned, the SIWs are quite similar to classic metallic waveguides. However, there are some different features inherent to the integrated SIW structures. For example, the resonant characteristics of a standing wave fed SIW slot array antenna is different from that of a metallic waveguide structure, where waveguides are all air-filled instead of dielectric-filled. The result is that the equivalent admittance of the slot cut on the SIW is more depend on its offset from the center because of the dielectric filling and waveguide height reduction.

Meanwhile, some classic post-fabrication tuning work for waveguide components can be relieved to a great extent by deploying the planar fabrication process. For example, the port match tuning based on an inductive metal post at the input port for a classic waveguide power divider can be realized easily by embedding a metallized via hole on the substrate.

It is worth mentioning that the research concerning SIWs has progressed much beyond its original concept as a laminated waveguide for applications such as antenna feeding structures[20]. Many new devices featuring excellent performances while exhibiting a compact profile were reported in a review article [12]. A typical example of this statement is a planar cavity oscillator, which is usually realized using a metallic cavity or a low-Q microstrip resonator [13]. In fact, as a member of the entire SICs family, the development of SIWs has well established its own set of design methods, rules and postulates and evolves into a systematic self-encapsulated integration discipline [18]. The concept of the SICs applies more to a fundamental methodology issue than simply an integration approach.

The design philosophy of SICs is not to fabricate every microwave integrated circuits using a monotonous integration strategy. Instead, SICs offers an integration technology which can exploit and combine the technical merits of different integration approaches. Meanwhile, this SIC methodology may eliminate the technical disadvantages of different integration approaches, partly at least if not completely, which is illustrated by a SIC mixer using a *surface-volume* hybrid integration approach in this work. An analogy can be made is that the SICs is not intended to be a key which is able to open every door. Instead, it is a balanced integration technology between different available technologies such as exchanging substrate size with quality-factor (e.g. microstrip, small size, lower-Q factor vs. SIW, larger size, higher-Q factor). It is also a bridge among different waveguiding structure geometries, which has already been proven by many developed transitions between planar structures and non-planar

structures [17]. It is an art where the designer's understanding of waveguiding mechanisms is crucial to make a proper decision on the selection of versatile integration technology.

Up to date, many interesting SICs components with very compact profile have been reported. However, so far, most of the research results in this area are still limited to fundamental demonstrations of single passive or active SICs components. Many of the advantages of general SICs are still not fully explored. Among them, one most interesting aspect in the SICs design is the potential ability to integrate a complete system on a single piece of substrate including a radiating element -- antenna, which can be designed most suitably with a non-planar structure. System level integration of this concept remains a question mark. The entire SICs building misses an important brick, i.e. a system-on-substrate integration demonstration [21]. The aim to answer this question constitutes the first fundamental motivation of this research.

Examining from the application side of microwave industry, one important commercial application is the short range frequency-modulation continuous-wave (FMCW) radar sensor, with typical functions such as level measuring and automotive cruise control [22]. The initial driving forces behind these research activities were mostly military applications [23, 24]. A large amount of efforts were put on the automotive application since the 1990's [4, 22, 25-27], when the matured GaAs monolithic integration technology opened the door for low-cost mass-production-based commercial applications. Many of these systems are constructed with an integrated transceiver chip and separate 3-D antennas, such as horn, lens or dish [7, 8]. The

fundamental limitation on system level integration is that a high directive, high-efficient and high-gain antenna system is simply not available based on a resistive semi-conductive material. Therefore, a more realistic approach is to fabricate a high performance antenna separately, and then interconnect the antenna to a monolithic transceiver through a planar-to-nonplanar transition structure. However, the required transitions between planar MMIC chips and non-planar antennas usually complicate the design and installation of the whole system and also increase the system cost, which may overshadow the advantages of employing the integrated MMICs.

This challenge, however, can be resolved relatively simple by using SICs integration technology, based on the fact that high performance waveguide type antennas could be designed through this technology. The objective to combine the superior integration ability of SICs and the application of a short range radar system becomes the second motivation of this research work. The output of this initiative constitutes the first contribution of this work.

The thesis is organized into five chapters, as outlined below.

Following this introduction, chapter 2 gives the design of the front-end system from the perspective of a set of performances specified functional blocks. The desired system performance is created by the interaction of these building blocks based on specified/synthesized block performances. As a matter of fact, the system design is a bilateral analysis-synthesis process throughout this work, in order to obtain achievable individual building block specifications with an acceptable design cost. The system design methodology includes system topology selection (homodyne/super-heterodyne)

7

and IF selection in terms of mixer spurious response (spurs) analysis/synthesis, linear gain/return loss analysis/synthesis and non-linear products/intermodulation levels analysis/synthesis. Based upon the system design method mentioned above, a test-bed using commercially available components was designed and tested. This part of the work was published in [28].

Chapter 3 presents different proposed antenna solutions for the radar system. Based on the chronological sequence of the development of this project, the design of a quasi-integrated H-plane sector horn [29], a nonplanar surface mountable horn [30] and an integrated SIW slot array [31] are investigated. Their pros and cons in the application of radar are discussed upon the measured antenna parameters.

Chapter 4 is devoted to the design of two different SIW and SICs mixers. An SIC mixer is proposed, which attempts to combine the advantages of different waveguiding structures as well as remove the limitations of each, based upon a proposed "surface-volume" [11] integration technique. The proposed SIC mixer performances are carefully compared with a mixer designed using conventional microstrip technology. Conclusion is made that the "surface-volume" integration approach indeed demonstrates a superior applicability compared with a monotonous integration approach. This is the second contribution of this work.

Integration issues unique to an FMCW radar front-end system-on-substrate are studied in chapter 5, such as the proper selection of different mixers, the leakage between two sets of antennas and its effect on the overall radar performances [32] and so on. The functionality of the front-end alone and the functionality of the front-end as in

FMCW radar are verified separately through different experiments. The measured data are carefully discussed as well. A conclusion and directions for future research work in this area are given in the end of the thesis.

CHAPTER 2 FRONT-END SYSTEM DESIGN

2.1 System Topology and Intermediate Frequency Selection

Two distinctively different FMCW radar systems are shown in figures below. The major difference lies on the selection of receiver intermediate frequency (IF) which leads to two different systems, namely, a heterodyne system and a homodyne system, also known as a high-IF system and a zero-IF system [4, 5, 33].

As shown in Figure 2-1, there is a central frequency shift Δf in the direct signal path between the FM generator and the receiver mixer. The amount of frequency offset is determined by transmitted spectrum width, filter design parameters in selecting the sideband, and the requirements for suppression of other parts of the signal spectrum. The basic purpose of the central frequency shift is the realization of a classical heterodyne reception. As the central frequencies of direct and reflected signals are separated by Δf, the converted signal spectrum will be grouped around that frequency. This permits the amplification of a received signal by an IF band-pass amplifier, as in the case of a typical heterodyne receiver with high receiver sensitivity. One major issue in heterodyne receivers is the suppression of unwanted image signals using filters with high quality factor, which requires careful filter design to reject unwanted sideband. Consequently, these multiple stages of down-conversion and amplification significantly increase the difficulty of system level integration and add to the complexity and cost of the system.
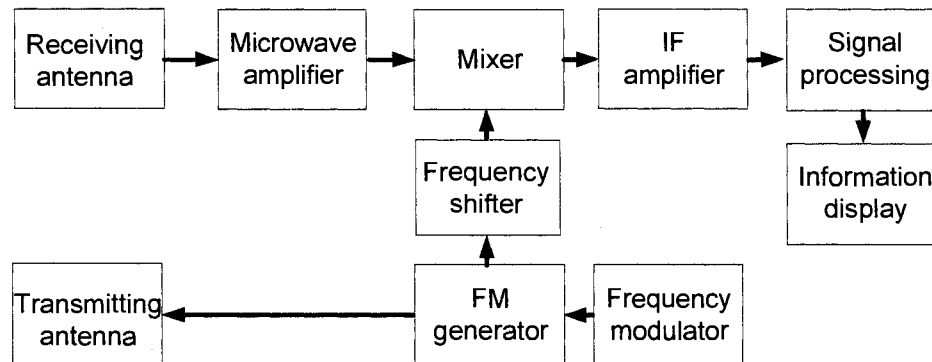
Figure 2- 1. FMCW radar with shifted intermediate frequency (from [24]).
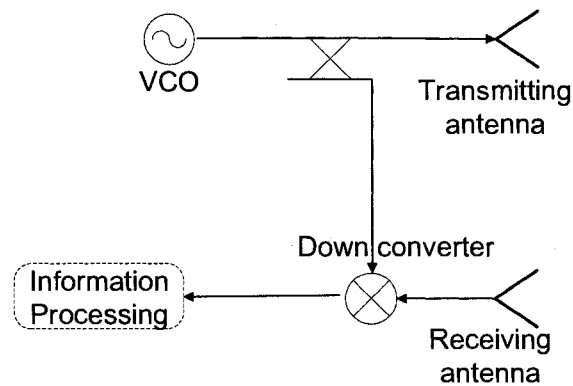
Figure 2- 2. Homodyne FMCW radar with zero intermediate frequency.

Shown in Figure 2-2 is a zero-IF system, also known as a homodyne system. In the case of homodyne FMCW radar, the reflected signal is directly down-converted to base-band by mixing with the reference signal. The mixer output is immediately followed by low pass filters and a chain of high-gain direct-coupled amplifiers that can amplify the demodulated base-band signals. The homodyne systems are quite attractive and widely adopted mainly due to the simplicity of its direct conversion receiver architecture, which is essential for ultra-compact, low-power and low-cost applications [25]. If implemented

successfully, homodyne FMCW radar systems are the most compact realizations one can achieve [8, 24].

Both of the two system architectures have their unique advantages and disadvantages in terms of system integration, topology complexity and signal distortion. For example, in the case of a homodyne system, because of the presence of a strong in-band LO signal, the generation of DC offset is unavoidable due to LO self-mixing. The extraneous DC voltage in the demodulated spectrum of a homodyne FMCW radar receiver will be amplified immediately by the following baseband amplifier stages. Therefore those unwanted DC offsets could not only corrupt the output, but also propagate through the baseband circuitry and saturate the subsequent stages. The separation of the down-converted output from the extraneous DC offset becomes troublesome. In the other hand, the heterodyne approach can eliminate the DC offsets very easily through capacitive coupling, but suffers the image interference unless multiple conversion stages and band pass filters are deployed in the system.

To accommodate these advantages and limitations, some modifications have to be made in the integrated system. In this work, the integrated radar receiver is implemented on the basis of a homodyne architecture for the purpose of simplicity. However, to reduce the free space leakage problem associated single antenna homodyne system, two integrated SIW antennas are used for transmitter and receiver respectively. This is a significant advantage associated with the SIW technology in a system design, which enables a high density integration scheme including dual antennas on the same substrate.

The measured free space leakage between both antennas is over 40 dB, which presents a significant improvement compared to the design using one antenna plus a circulator.

In the radar transmitter, care must be taken to select an appropriate IF to facilitate the filtering after up-converting. As a general case, the output spectra of a mixer are defined by the order of RF harmonics and LO harmonics with $f_{IF} = mf_{LO} + nf_{RF}$ where m and n are integers.

Considering a system with an LO of 24.05 GHz and IF bandwidth of 30 MHz ~ 105 MHz generated from a sweeping VCO , the transmitter up-converter output spur chart is plotted in Figure 2-3. The mixer output spurious response (spur) including the upper-side-band component (USB) and the lower-side-band (LSB) component are defined by $f_{RF} = f_{LO} + f_{IF}$ and $f_{RF}' = f_{LO} - f_{IF}$ respectively, which correspond to $f_{IF} = -f_{LO} + f_{RF}$ (m,n)=(-1,1) as the red line shown in the spur chart and $f_{IF}' = f_{LO} - f_{RF}$ (m,n)=(1,-1) as the black line shown in the spur chart. The LSB and USB bandwidth are 23.945 GHz~24.02 GHz and 24.08 GHz~24.155 GHz respectively. To separate the two bands apart, a filter with a transit band of 0.06 GHz over 24 GHz would be required, which means a 0.249% relative bandwidth. This filtering task becomes almost impossible because of the low IF selection. On the other hand, if a higher IF is selected so that the LSB, LO and USB bands can be widely separated, then the filtering circuitry requirements will be greatly relieved. In this work, a 2.4-GHz IF is selected as the front-end transmitter IF. The related mixer output spur chart [34] is plotted in Figure 2-4 as shown below.
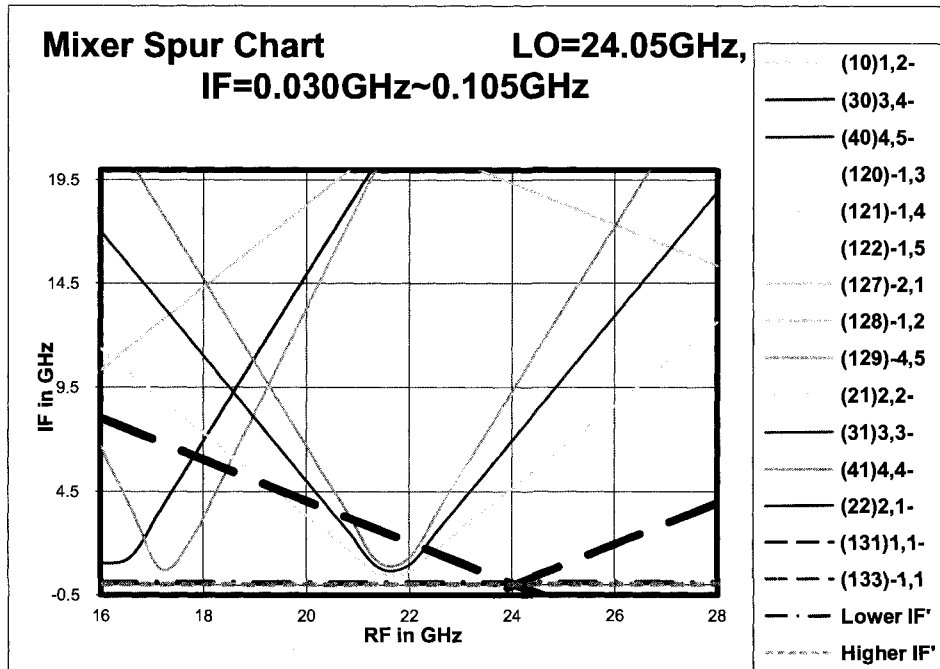
Figure 2- 3. Transmitter mixer spurious response chart (IF=67 MHz).
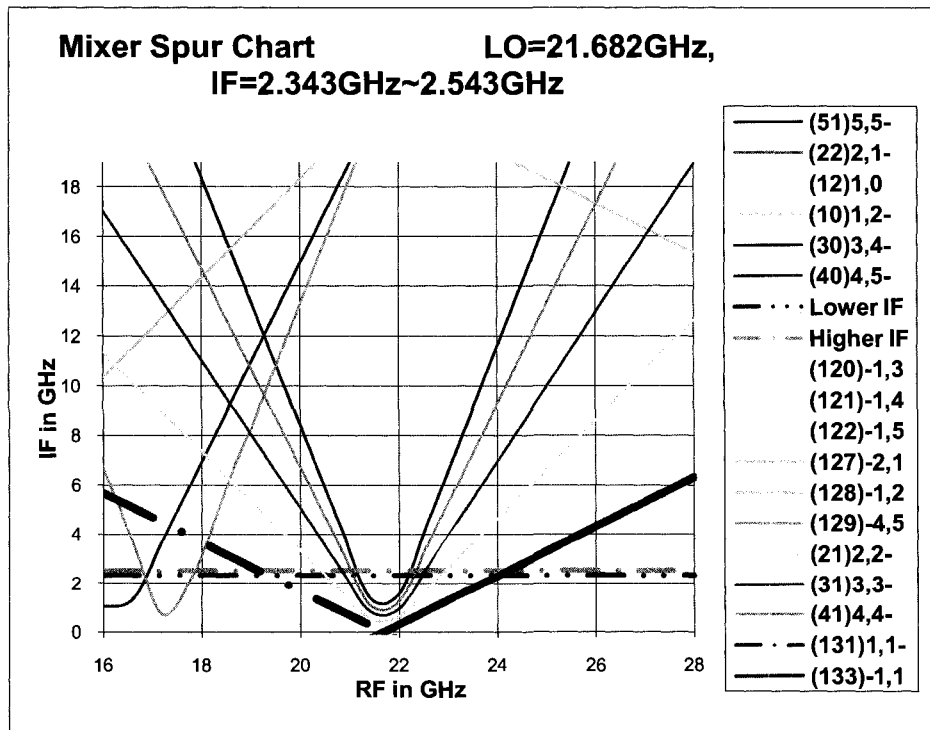
Figure 2- 4. Transmitter mixer spurious response chart (IF=2.4 GHz).

With an IF bandwidth from 2.343 GHz~2.543 GHz and LO 21.682 GHz, the LSB

band and USB band are 19.139 GHz~19.339 GHz and 24.025 GHz~24.225 GHz

respectively. For this selected IF, the relative filter transit band is increased to 19.4%.

Under this circumstance, a high pass filter in the form of a section of SIW or a narrow

band antenna can be integrated within the substrate to attenuate the undesired signal. A

proposed front-end system block diagram is shown in Figure 2-5.
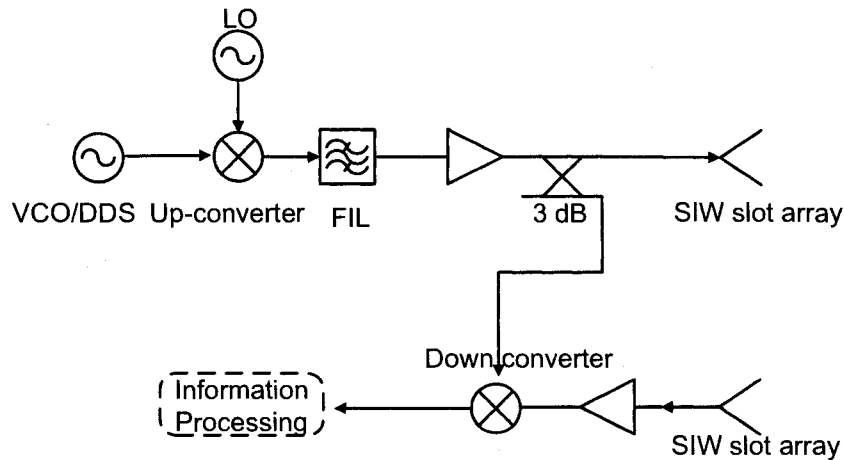
Figure 2- 5. An FMCW radar with a zero-IF receiver, a high-IF transmitter.

2.2 Cascade System Linear Gain Analysis

The system gain is contributed by the gain or loss of each individual building block

and the interconnecting transitions and adapters. For an ideal system where all the

building blocks have the same nominal port impedance, say 50Ω, the system gain will

simply be the sum of the individuals. However, the mismatch between different building

blocks or transitions between different waveguiding structures such as microstrip-to-

SIW transition will complicate the system gain calculation, because they may create

reflections or multiple-reflections due to their bilateral characteristics. In order to accurately estimate the cascade gain, the mismatches between different cascaded modules must be modeled and accounted for [35]. An approach treating the multiple reflections effects as a feed-back network is adopted in this work [36]. Consider a bilateral interconnection module j between two modules j-1 and j+1, with a voltage transfer ratio represented by τ_j, the voltage at the output of this cascade is $v_{o,j+1}$, the voltage at the input is $v_{o,jT}$. The net forward signal gain estimation should include the multiple reflections created among these modules. Therefore, the contribution to the cascade gain variance caused by individual mismatches can be modeled by the following network as in Figure 2-6 [36, 37].
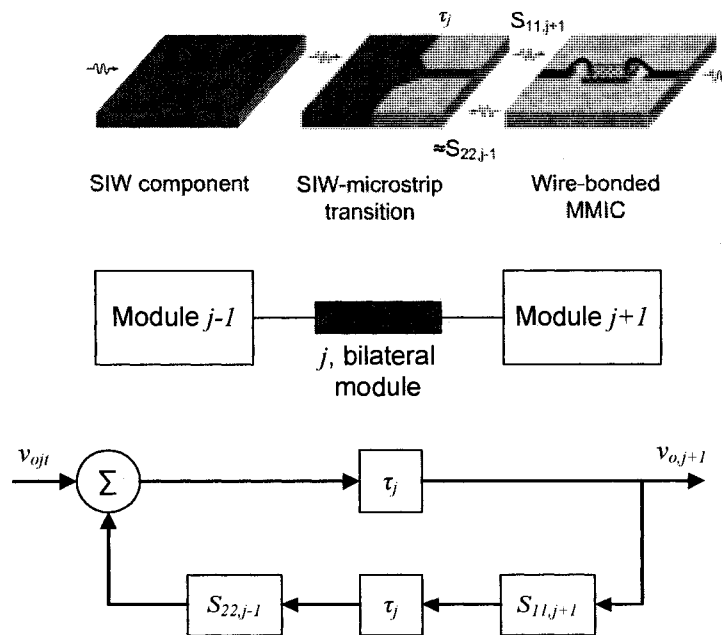
Figure 2- 6. Modeling a three-module cascade with imperfect port matching.

The closed-loop equation is given by

$$[v_{ojT} + (S_{22,j-1} \cdot \tau_j \cdot S_{11,j+1}) \cdot v_{o,j+1}] \cdot \tau_j = v_{o,j+1}$$

$$v_{ojT} \cdot \tau_j + S_{22,j-1} \cdot \tau_j^{\,2} \cdot S_{11,j+1} \cdot v_{o,j+1} = v_{o,j+1} \qquad (2.1)$$

$$\frac{v_{o,j+1}}{v_{ojT}} = \frac{\tau_j}{1 - S_{22,j-1} \cdot \tau_j^{\,2} \cdot S_{11,j+1}}$$

where τ_j can be modeled as $\tau_j = e^{-\alpha d} \cdot e^{-j\beta d}$.

The closed loop voltage transfer function is given by

$$\alpha_j = \frac{v_{o,j+1}}{v_{ojT}} = \frac{\tau_j}{1 - S_{22,j-1} \cdot \tau_j^{\,2} \cdot S_{11,j+1}} \qquad (2.2)$$

The open-loop (round-trip, shorted as RT in subscript) voltage transfer function can be

obtained by

$$| \alpha_{RTj} | = | \tau_j |^2 | S_{22,j-1} | \cdot | S_{11,j+1} |$$

$$= | \tau_j |^2 \cdot \frac{VSWR_j - 1}{VSWR_j + 1} \cdot \frac{VSWR_{j+1} - 1}{VSWR_{j+1} + 1} \qquad (2.3)$$

The corresponding forward power gain is given by

$$g_j = | \alpha_j |^2$$

$$= \frac{| \tau_j |^2}{(1 - S_{22,j-1} \cdot \tau_j^{\,2} \cdot S_{11,j+1})[1 - S_{22,j-1}^{*} \cdot (\tau_j^{\,2})^{*} \cdot S_{11,j+1}^{*}]}$$

$$= \frac{| \tau_j |^2}{1 - S_{22,j-1} \cdot \tau_j^{\,2} \cdot S_{11,j+1} - S_{22,j-1}^{*} \cdot (\tau_j^{\,2})^{*} \cdot S_{11,j+1}^{*} + | S_{22,j-1} \cdot \tau_j^{\,2} \cdot S_{11,j+1} |^2} \qquad (2.4)$$

$$= \frac{| \tau_j |^2}{1 - 2 | S_{22,j-1} \cdot \tau_j^{\,2} \cdot S_{11,j+1} | \cdot \cos(\angle S_{11,j+1} + \angle S_{22,j-1} - 2\beta d) + | S_{22,j-1} \cdot \tau_j^{\,2} \cdot S_{11,j+1} |^2}$$

$$= \frac{| \tau_j |^2}{1 - 2 | S_{22,j-1} \cdot \tau_j^{\,2} \cdot S_{11,j+1} | \cdot \cos\theta + | S_{22,j-1} \cdot \tau_j^{\,2} \cdot S_{11,j+1} |^2}$$

where $\theta = \angle S_{11,j+1} + \angle S_{22,j-1} - 2\beta d$

Using (2.3) and we have

$$g_j = \frac{|\tau_j|^2}{1 - 2|\alpha_{RTj}|\cos\theta + |\alpha_{RTj}|^2} \qquad (2.5)$$

Therefore, the minimum and maximum forward voltage gain can be given by

$$|\alpha_j|_{max} = \frac{|\tau_j|}{\sqrt{1 - 2|\alpha_{RTj}| + |\alpha_{RTj}|^2}} = \frac{|\tau_j|}{1 - |\alpha_{RTj}|} \qquad (2.6)$$

$$\text{and } |\alpha_j|_{min} = \frac{|\tau_j|}{\sqrt{1 + 2|\alpha_{RTj}| + |\alpha_{RTj}|^2}} = \frac{|\tau_j|}{1 + |\alpha_{RTj}|} \qquad (2.7)$$

when $\cos\theta$ varies from 1 to -1 representing the sum up effect of multiple reflections is in phase or off-phase. The average gain of interconnection module j is obtained by

$$\begin{aligned}
\bar{g}_j &= \frac{|\tau_j|^2}{2\pi} \int_0^{2\pi} \frac{d\theta}{1 - 2|\alpha_{RTj}|\cos\theta + |\alpha_{RTj}|^2} \\
&= \frac{|\tau_j|^2}{1 - |\alpha_{RTj}|^2} = |\alpha_j|_{max} \cdot |\alpha_j|_{min}
\end{aligned} \qquad (2.8)$$

To write in dB form we have

$$\begin{aligned}
\bar{G}_j &= 10\log\bar{g}_j = 10\log\frac{|\tau|}{1 - |\alpha_{RT}|} + 10\log\frac{|\tau|}{1 + |\alpha_{RT}|} \\
&= \frac{20\log\frac{|\tau|}{1 - |\alpha_{RT}|} + 20\log\frac{|\tau|}{1 + |\alpha_{RT}|}}{2} = \frac{G_{j,max} + G_{j,min}}{2}
\end{aligned} \qquad (2.9)$$

The maximum gain deviation of the interconnection caused by multiple reflections can be expressed (in dB) as

$$\Delta_{max} = G_{j,max} - \overline{G}_j = G_{j,max} - \frac{G_{j,max} + G_{j,min}}{2}$$

$$= \frac{G_{j,max}}{2} - \frac{G_{j,min}}{2} = 10\log\frac{|\tau|}{1-|\alpha_{RT}|} - 10\log\frac{|\tau|}{1+|\alpha_{RT}|} \qquad (2.10)$$

$$= 10\log\frac{1+|\alpha_{RT}|}{1-|\alpha_{RT}|}$$

The overall cascade system gain variance can then be determined upon the cumulative of the gain variance of each individual module. The worst case and best case cascade gain can be estimated based on the calculated overall gain variance. Using a spreadsheet, the system gain behaviour can be estimated based on this method.

The above mentioned cascade gain estimation approach is not limited to integrated system design. Systems using multiple-chip-modules interconnected by adapters or cables can also be estimated by this method. In this work, a radar front-end prototype using commercially available components was designed using the above mentioned approach to estimate the cascaded gain. A design example is shown in the Table 2-1. A description of the procedure to calculate the cascade gain is given as follows. The first part of the table describes the behaviour of each individual building block including the gain and port matching conditions. Active modules such as amplifiers and mixers are assumed to be unilateral. Their gain variances come from measurement results within the operating frequency bandwidth. Passive modules such as transitions or adapters are bilateral and they are the cause of multiple reflections. A baseband VCO is measured with 0 dBm output power and a +/- 1.0 dBm variance, i.e. -1.0 dBm to 1.0 dBm. The output return loss of this VCO is 9 dB, from which the output VSWR of 2.09 can be calculated. This VCO module is connected to an up-converter through an

interconnection (adapter), which has a 1.5 dB insertion loss and a measured port VSWR of 1.2. Based on Eq. 2.3, the open-loop gain of this interconnection including multiple reflection effect between the VCO output and up-converter input port can be calculated as 0.022. A gain variance of 0.2 dB will be caused by this value, from Eq. 2.10. The gain (power level) variance is calculated in the second part of the work sheet, where gain variance caused by the mismatching at each individual module port is computed. It is reflected in the second part that the gain of the adapter will be varied between -1.5 (dB)-0.2 (dB)= -1.7 (dB) to -1.5 (dB)+0.2 (dB)= -1.3 (dB). These numbers are accumulated consecutively at the third part of the work sheet, where the gain variance and gain of the cascaded modules are summed up. Therefore, at the output of the adapter in the cascaded, when multiple-reflection effect is taken into account, the power level is estimated to be varied between -1.0 (dBm)+(-1.7 (dB))= -2.7 (dBm) and 1.0 (dBm)+ (-1.3 (dB))= -0.3 (dBm), as shown in the third part of the table. The net gain variance at the adapter output port is the summed up of the variance of the VCO module and the interconnection module, i.e. 1.0 (dB)+0.2 (dB)=1.2 (dB). Consecutively, the output power level at each stage in the cascaded system can be calculated and the entire cascade gain performances can be estimated this way.

Table 2- 1. System linear gain analysis/synthesis.

	Gain	Gain	SWR				
	nom	+/-	at out		$|a_{RT}|$	Port S_{11}	RL
VCO	0.0 dB	1.0 dB	2.09987834				9 dB
adapter	-1.5 dB		1.2		0.02283		
Mixer	-8.0 dB	2.0 dB	1.3289767			-17 dB	17 dB
filter_high_pass	-1.5 dB		2		0.03333		
Driver Amp.	16.0 dB	2.0 dB	1.92495059			-10 dB	10.0 dB
3dB power Div	-4.0 dB		1.1		0.00599		
Power Amp.	13.0 dB	2.0 dB	1.67089966			-12.0 dB	12.0 dB
Derived							
	Gain	Gain	Gain	Gain			
	mean	max	min	±			
VCO	0.00 dB	1.00 dB	-1.00 dB	1.00 dB			
adapter	-1.50 dB	-1.30 dB	-1.70 dB	0.20 dB			
Mixer	-8.00 dB	-6.00 dB	-10.00 dB	2.00 dB			
filter_high_pass	-1.50 dB	-1.21 dB	-1.78 dB	0.29 dB			
Driver Amp.	16.00 dB	18.00 dB	14.00 dB	2.00 dB			
3dB power Div	-4.00 dB	-3.95 dB	-4.05 dB	0.05 dB			
Power Amp.	13.00 dB	15.00 dB	11.00 dB	2.00 dB			
Cumulative							
At the output of	Pwr	max Pwr	min Pwr	Var			
VCO 1	0.00 dBm	1.00 dBm	-1.00 dBm	1.00 dB			
adapter	-1.50 dBm	-0.30 dBm	-2.70 dBm	1.20 dB			
Mixer	-9.50 dBm	-6.30 dBm	-12.70 dBm	3.20 dB			
filter_high_pass	-10.99 dBm	-7.50 dBm	-14.48 dBm	3.49 dB			
Driver Amp.	5.01 dBm	10.50 dBm	-0.48 dBm	5.49 dB			
3dB power Div	1.01 dBm	6.55 dBm	-4.53 dBm	5.54 dB			
Power Amp.	14.01 dBm	21.55 dBm	6.47 dBm	7.54 dB			

2.3 Cascade System Nonlinear Intermodulation Products and Intercept Points Analysis

Apart from the linear gain analysis of a cascaded system, the nonlinear analysis of a system is also an important part in the design process. Assuming that none of the modules of the cascaded system are input too much power or are saturated, i.e. the input power level for different modules are well below the 1-dB saturation point (P1dB point) for active circuits, the most problematic nonlinear issue concerning a system is the generated intermodulation distortion (IMD) products in the cascaded stages. When the nonlinearity of active devices is modeled as a three-term power series, a convenient way to express this characteristic is to use intercept points, which is the quantitative description of its intermodulation products (intermods) levels. Because its frequency is by nature adjacent to in-band signal, third order intermodulation distortion products analysis is absolutely necessary for microwave system design. As the active devices will saturate long before 3rd-order IMD product intercepts the fundamental output power, the measurement of IP3 is usually carried out when the devices are operated well within the small signal region and the IP3 is usually approximated from the interception between the extrapolation of the third order IMD and the fundamental output power. A common estimation for this signal level is 10 dB lower than P1dB gain compression point. For a two port active device such as an amplifier, the *output* 3rd intercept point (OIP3) is given by

$$OIP_3 = P_{out,F} + \frac{\Delta}{2},$$

(2.11)

where $P_{out,F}$ is the output power level in dB, Δ is the level (in dBc) of the IMD relative to the fundamental. For a three port active device such as a mixer, *input* 3rd intercept point is usually measured by

$$IIP_3 = A + \frac{\Delta}{2}$$

(2.12)

as demonstrated in the graph.
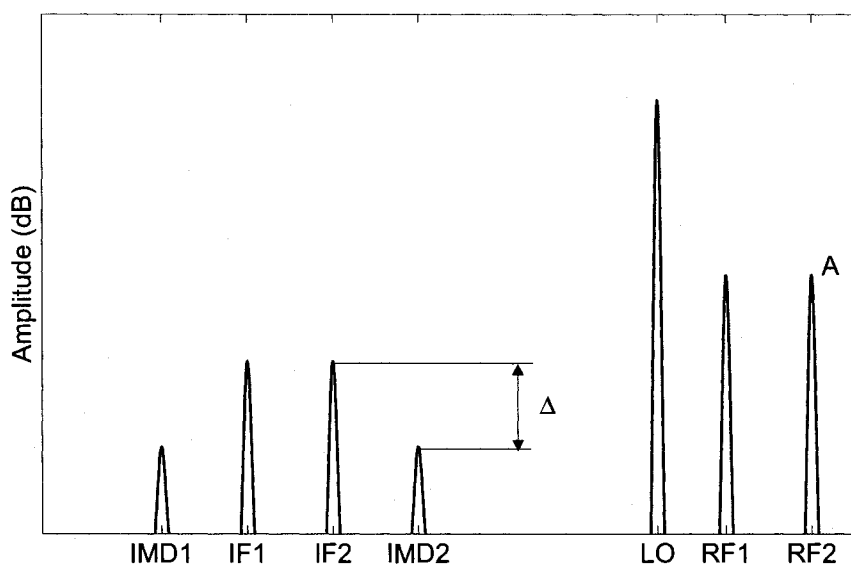
Figure 2- 7. Spectrum components of a mixer with two-tones input.

The calculation of IP3s of a cascaded system is well documented in many resources such as [38]. In order to facilitate the calculation of nonlinear products in a cascaded system, we assume that the gain of each individual block is the same for all of the signals of interest, including the fundamental signals and their intermods. The general cascaded intermods calculation can actually be simplified based on a two-modules-cascade model, with one module representing the second module and the other representing the cascade of all preceding modules.

The intermod power of the first module at its output port can be written as [36]

$$p_{out,IM3}(\pm 2f_1 \pm f_2) = \frac{p_{out,F1}^2 p_{out,F2}}{p_{OIP3,IM}^2}$$

(2.13)

where *F1* and *F2* refer to tone 1 and tone 2 respectively.

Since we have assumed the same frequency response for IMDs too, after the second module, the total IMDs at the cascade output is the sum of the IMDs from the first module times the gain of the second module, plus the newly generated IMDs at the second module. As it is pointed in [39], IMDs which are close to each other (in frequency) tend to be in phase, which means that IMDs created at different modules should be combined voltage-wisely, i.e. IMDs voltage amplitude summation is a more accurate estimation of the worst case IMD estimation of a cascade system. Because of this, the total IMDs at the output of the cascade can be expressed as [36]

$$p^{1/2}_{out,IM3,casc}(\pm 2f_1 \pm f_2) = g_2^{1/2} \cdot \frac{p_{out,F1,1}p_{out,F2,1}^{1/2}}{p_{OIP3,IM,1}} + \frac{p_{out,F1,2}p_{out,F2,2}^{1/2}}{p_{OIP3,IM,2}}$$

(2.14)

$$= \frac{(g_2 \cdot p_{out,F1,1})(g_2 \cdot p_{out,F2,1})^{1/2}}{g_2 \cdot p_{OIP3,IM,1}} + \frac{p_{out,F1,2}p_{out,F2,2}^{1/2}}{p_{OIP3,IM,2}}$$

(2.15)

Note that

$$p_{out,F1,2} = p_{out,F1,casc}$$

(2.16)

$$p_{out,F2,2} = p_{out,F2,casc}$$

(2.17)

$$g_2 \cdot p_{out,F1,1} = p_{out,F1,casc}$$

(2.18)

$$g_2 \cdot p_{out,F2,1} = p_{out,F2,casc}$$

(2.19)

Then (2.15) is rewritten as

$$p^{1/2}_{out,IM3,casc}(\pm 2f_1 \pm f_2) = \frac{p_{out,F1,cas}\, p^{1/2}_{out,F2,cas}}{g_2 \cdot p_{OIP3,IM,1}} + \frac{p_{out,F1,cas}\, p^{1/2}_{out,F2,cas}}{p_{OIP3,IM,2}}$$ (2.20)

$$p^{1/2}_{out,IM3,casc}(\pm 2f_1 \pm f_2) = p_{out,F1,casc} \cdot p^{1/2}_{out,F2,casc}\left(\frac{1}{g_2 \cdot p_{OIP3,IM,1}} + \frac{1}{p_{OIP3,IM,2}}\right)$$ (2.21)

$$p_{out,IM3,casc}(\pm 2f_1 \pm f_2) = p^2_{out,F1,casc} \cdot p_{out,F2,casc}\left(\frac{1}{g_2 \cdot p_{OIP3,IM,1}} + \frac{1}{p_{OIP3,IM,2}}\right)^2$$ (2.22)

The OIP3 of the two-modules cascade system can be found as in [40]

$$\frac{1}{p_{OIP3,casc}} = \frac{1}{g_2 p_{OIP3,1}} + \frac{1}{p_{OIP3,2}}$$ (2.23)

To translate the IP3 points from output port to input port, times the gain of the two modules $g_1 g_2$ at both sides of the equation above and we have

$$\frac{1}{p_{OIP3,cas}/g_1 g_2} = \frac{g_1}{p_{OIP3,1}} + \frac{g_1 g_2}{p_{OIP3,2}}$$ (2.24)

$$= \frac{1}{p_{OIP3,1}/g_1} + \frac{1}{p_{OIP3,2}/g_1 g_2} = \frac{1}{p_{IIP3,cas}}$$ (2.25)

Therefore it is evident for a two module cascade, the worst case IP3 estimation can be made by

$$\frac{1}{p_{IIP3,cas}} = \frac{1}{p_{IIP3,1}} + \frac{g_1}{p_{IIP3,2}}$$ (2.26)

A design of cascaded transmitter is shown in the table below. It should be noticed that very often in practice, output IP3s are cited in case of amplifier, input IP3s are cited in case of mixer.

Table 2- 2. System non-linear products analysis/synthesis.

	Gain nom	Gain +/-	SWR at out	|aRT|	OIP3	IIP3 with	
VCO1	0.0 dB	1.0 dB	2.099878				
adapter	-1.5 dB		1.2	0.0228			
Mixer	-8.0 dB	2.0 dB	1.328		5.1 dBm		
Filter_high	-1.5 dB		2	0.0332			
Driver Amplifier	16.0 dB	2.0 dB	1.924951		39.0 dBm	23.0 dBm	
3dB power divider	-4.0 dB		1.1	0.0060			
Power Amplifier	13.0 dB	2.0 dB	1.6709		26.0 dBm		

Derived

	Gain mean	max	min	±			
VCO1	0.00 dB	1.00 dB	-1.00 dB	1.00			
adapter	-1.50 dB	-1.30 dB	-1.70 dB	0.20			
Mixer	-8.00 dB	-6.00 dB	-10.00 dB	2.00			
Filter_high	-1.50 dB	-1.21 dB	-1.78 dB	0.29			
Driver Amplifier	16.00 dB	18.00 dB	14.00 dB	2.00			
3dB power divider	-4.00 dB	-3.95 dB	-4.05 dB	0.05			
Power Amplifier	13.00 dB	15.00 dB	11.00 dB	2.00			

Cumulative

at output of	mean Pwr	max Pwr	min Pwr	±Gain	IIP3 mean	IIP3 with max gain	IIP3 with min gain
VCO1	0.00 dBm	1.00 dBm	-1.00 dBm	1.00 dB			
adapter	-1.50 dBm	-0.30 dBm	-2.70 dBm	1.20 dB			
Mixer	-9.50 dBm	-6.30 dBm	-12.70 dBm	3.20 dB	14.60	11.40	17.80
Filter_high	-10.99 dBm	-7.51 dBm	-14.48 dBm	3.49 dB	14.60	11.40	17.80
mixer from in	5.01 dBm	10.49 dBm	-0.48 dBm			11.38	17.69
mixer at out	5.01 dBm	10.49 dBm	-0.48 dBm	5.49 dB	14.55	11.38	17.69
3dB power divider	1.01 dBm	6.55 dBm	-4.53 dBm	5.54 dB	14.55	11.19	16.95
Power Amplifier	14.01 dBm	21.55 dBm	6.47 dBm	7.54 dB	10.07	11.19	16.95

2.4 Test-bed Using Multiple Chip Modules

A test-bed using commercially available multiple-chip modules based on the above design methodology was designed and part of the results were published in [28]. A wide tuning bandwidth VCO is used to generate a triangular FM signal. Tuning voltages are carefully selected so that the VCO works in a relatively linear tuning range. A 211 MHz FM signal centered at 2.443 GHz is generated to provide a LFM signal. For a triangular modulation scheme, the demodulated mixer output signal frequency f_R is related to the target range by

$$f_R = \frac{4 \cdot \Delta f \cdot f_m \cdot R}{c}$$

where f_m is the modulation frequency, Δf is the tuning bandwidth, R is the distance between the target and the radar and c is the speed of light. A range measurement with a 0.25 m range step by using a corner reflector as a target is performed. A linear response of the measured output IF frequency as a function of target range is observed, which confirms the functionality of the design methodology.

CHAPTER 3 RADAR ANTENNA DESIGN

Different antenna solutions were studied in this work including an H-plane sector horn antenna, a surface mountable pyramidal horn antenna and an SIW slot array antenna. These different types of antenna have their own advantages and limitations in terms of electrical performances such as radiation pattern, input impedance matching, operating bandwidth and mechanic considerations in connection with the integration with other front-end components, profile size, fabrication difficulties and so on. This chapter discusses the design considerations, integration issues, measurement results and their applications in radar system.

3.1 H-Plane Sector Horn

This antenna was the first antenna prototype considered in this thesis work for the integrated radar system [29]. The origin of this proposal comes from the quasi-waveguide geometrical resemblance between SIW and a full waveguide. This is because a classic metallic waveguide H-plane sector horn is nothing but a waveguide aperture flared into a large opening on the H-plane. However, significant radiation would not happen if the two parallel metallized via holes of SIW are flared open only on one substrate layer. The physical explanation of this is related to the very thin substrate thickness, compared with propagation wavelength, will confine the electromagnetic

waves within the substrate instead of radiating. An electromagnetic explication is that the displacement current will close within the substrate instead of closing at the far field to constitute radiation. To design a radiating structure using this concept, a larger opening in terms of propagation wavelength at the physical aperture of the antenna must be obtained, especially in the E-plane. The original idea has therefore evolved into using two substrate layers to sandwich a low permittivity foam layer in between. As such, an aperture with 0.66λ on the E-plane can be formed and the H-plane has an opening of 7.21λ. A schematic view of the proposed H-plane sector horn is shown in Figure 3-1.

Because the two linear equally spaced metal post arrays act as electric walls, the excited mode inside the input SIW section is quasi-TE10 mode. Therefore, Huygen's equivalent principle can be applied to the aperture across the opening to obtain equivalent current on the aperture. The far-field magnetic vector potential $\bar{A}$ and electric vector potential $\bar{F}$ can be obtained by integrating equivalent electric and magnetic currents over the aperture. Assuming aperture fields are associated with transverse electric fields of the waveguide through a quadratic phase item [41], then the substitution of this relationship into magnetic vector potential and electric vector potential will result in a two-dimensional Fourier transform. Far-field electric fields and magnetic fields can then be obtained from the electric vector potential and magnetic vector potential.
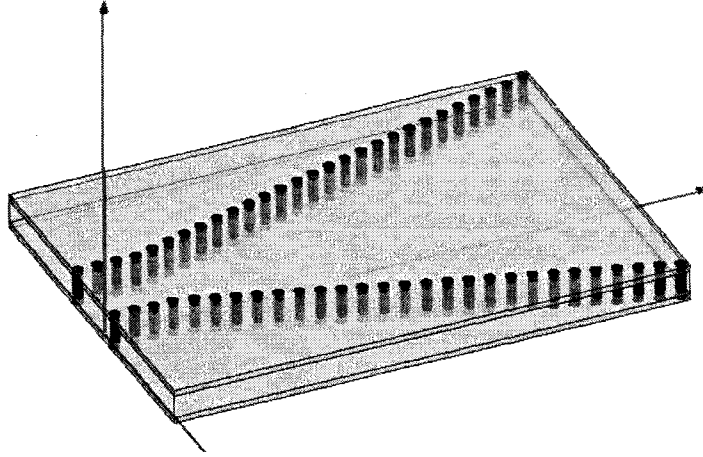
Figure 3- 1. Schematic view of a substrate integrated horn antenna.

Based on the above design principles, the horn antenna pattern can be computed with following formulas [41]. The E-plane pattern (φ=90°) is given by

$$F_E(\theta) = \frac{1+\cos\theta}{2} \frac{\sin[(\beta b/2)\sin\theta\sin\varphi]}{(\beta b/2)\sin\theta\sin\varphi} \tag{3.1}$$

and the H-plane pattern is given by

$$F_H(\theta) = \frac{1+\cos\theta}{2} \frac{I(\theta,\varphi=0^\circ)}{I(\theta=0^\circ,\varphi=0^\circ)} \tag{3.2}$$

where

$$I(\theta,\varphi) = e^{j(R_1/2\beta)(\beta\sin\theta\cos\varphi+\pi/A)^2}[C(s_2') - jS(s_2') - C(s_1') + jS(s_1')] +$$

$$e^{j(R_1/2\beta)(\beta\sin\theta\cos\varphi-\pi/A)^2}[C(t_2') - jS(t_2') - C(t_1') + jS(t_1')] \tag{3.3}$$

$$s_1' = \sqrt{\frac{1}{\pi\beta R_1}}(-\frac{\beta A}{2} - R_1\beta\sin\theta\cos\varphi - \frac{\pi R_1}{A}) \tag{3.4}$$

$$s_2' = \sqrt{\frac{1}{\pi\beta R_1}}(\frac{\beta A}{2} - R_1\beta\sin\theta\cos\varphi - \frac{\pi R_1}{A}) \tag{3.5}$$

$$t_1' = \sqrt{\frac{1}{\pi\beta R_1}}(-\frac{\beta A}{2} - R_1\beta\sin\theta\cos\varphi + \frac{\pi R_1}{A}) \qquad (3.6)$$

$$t_2' = \sqrt{\frac{1}{\pi\beta R_1}}(\frac{\beta A}{2} - R_1\beta\sin\theta\cos\varphi + \frac{\pi R_1}{A}) \qquad (3.7)$$

where $C(x)$ and $S(x)$ are Fresnel integrals defined as

$$C(x) = \int_0^x \cos(\frac{\pi}{2}\tau^2)d\tau$$

and

$$S(x) = \int_0^x \sin(\frac{\pi}{2}\tau^2)d\tau$$

Notice that this design approach implies two assumptions [41]. The first assumption is that the aperture fields exist only over a finite portion (physical aperture) of the antenna where the antenna is mounted on an infinite ground plane. The second is that the aperture is large enough (several wavelengths in both dimensions) so that aperture electric fields and aperture magnetic fields are related by a TEM relationship. A prototype geometry description is given in Figure 3-2. The aperture width A is 53.50 mm; axial length R_H is 77.30 mm; input waveguide broad width a is 7.112 mm; b, which is not shown, is the height of a foam layer with 3.57 mm; flare angle α_H is 16.70°; metal post diameter d is 0.90 mm; the center distance between two metal posts p is 1.80 mm. Top layer and bottom layer substrate both have a thickness of 1.00 mm.
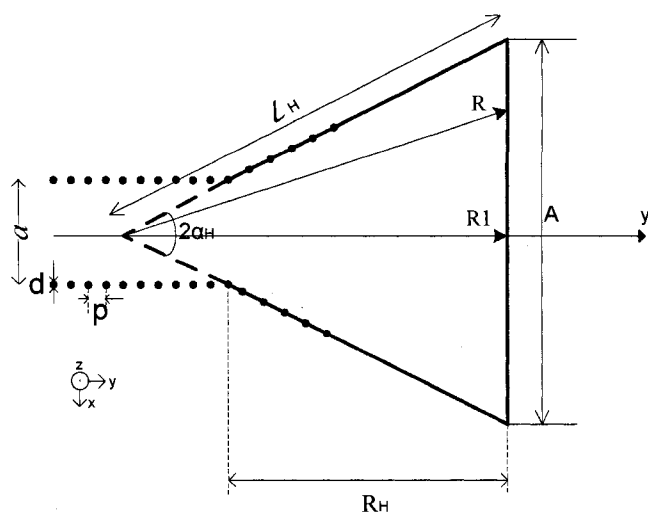
Figure 3- 2. Design parameters of a substrate integrated horn.

The measured antenna input S11 magnitude is shown in Figure 3-3 where the solid line represents measurement results, and dash line represents simulation results obtained from Agilent HFSS. It can be observed that the simulation results generally match the measurement results. A broadband input VSWR with 1.57 or lower is obtained due to the wide-band quasi-waveguide characteristic by applying SIW technology.
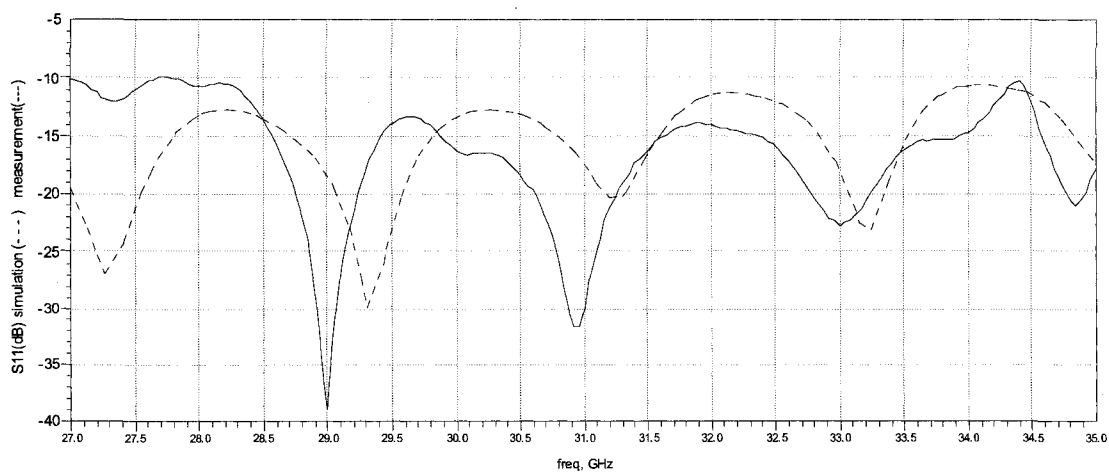
Figure 3- 3. Measured and simulated antenna input S11 magnitude.

The far-field radiation pattern is measured in a compact-range anechoic chamber as shown in Figure 3-4 and Figure 3-5. Both co-polarization component and cross-polarization component of H-plane pattern and E-plane pattern are measured. Around 16° half-power beam width (HPBW) in H-plane and around 47° HPBW in E-plane are obtained. The cross-polarization component level at the main radiation beam is more than 20 dB lower than the co-polarization component. Symmetrical radiation pattern is achieved in the H-plane, while in the E-plane asymmetry appears. This could be caused by the misalignment of the substrate and foam layers during fabrication. It could also be due to the metal base mounted underneath the antenna or the asymmetry of the installation when the antenna is mounted on the rotation table of the measurement system.
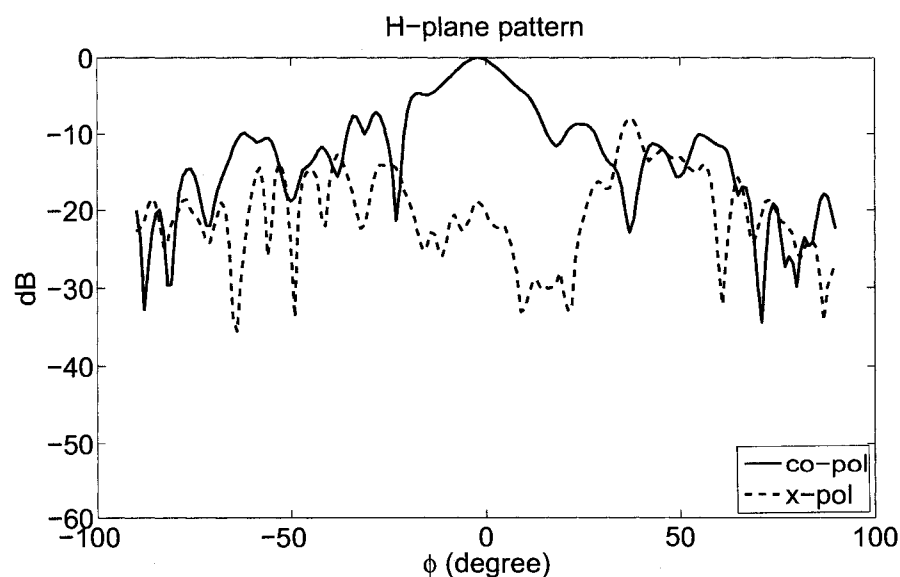
Figure 3- 4.Measured H-plane radiation pattern.
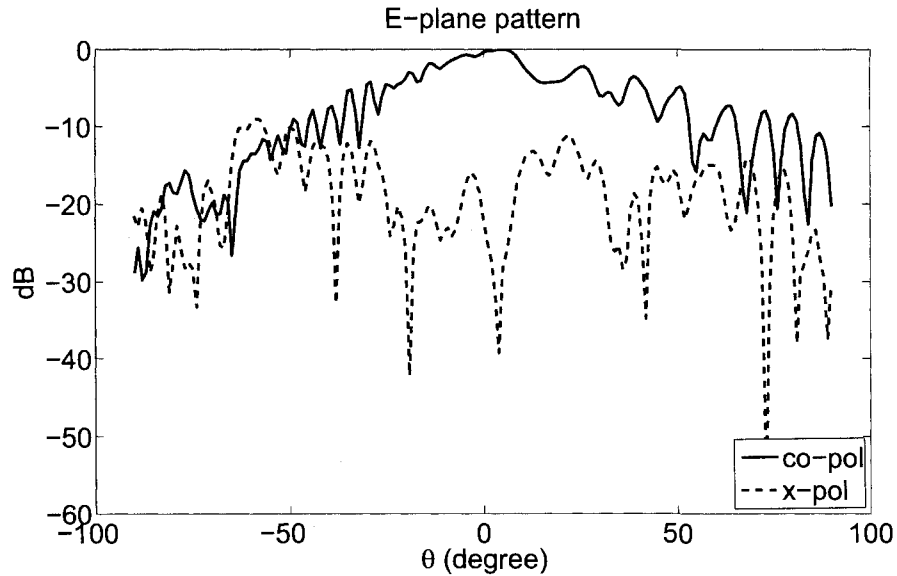
E-plane pattern

Figure 3- 5. Measured E-plane radiation pattern.

Since the two assumptions mentioned above are not well satisfied, theoretical results (not shown) and measurement results start to have more differences when deviating from the antenna main beam, which is because of the edge diffraction effect of the horn. More accurate simulation can be obtained if the fringe current at the edge of waveguide aperture is taken into consideration [42].

There are some advantages of this type of antenna. For example, the antenna provides a wide input matching, which is a direct benefit of using the SIW structures. A narrow H-plane radiation pattern is also obtained as well as a compact profile and a low fabrication cost. However, there are also some inherent drawbacks. Two important ones are a non-planar input feeding port and a wide E-plane HPBW. Because the antenna prototype is connected to a coaxial input through a coaxial-waveguide transition, the real input feeding of the antenna should be considered as a waveguide port, i.e. a non-planar

input feeding. The integration of this antenna with other planar SIW circuitry would require an SIW-waveguide transition. Meanwhile, a wide E-plane radiation pattern due to the narrow E-plane opening could be a disadvantage for radar application, where relatively narrow radiation beam width is generally desired to avoid environment clutters. To overcome these limitations, a surface mountable pyramidal horn antenna is proposed.

3.2 Surface Mountable Pyramidal Horn

As mentioned above, because the H-plane sector horn antenna feeding port should be considered as a non-planar structure, a transition from SIW-waveguide would be required if a horn type antenna were to be used. Meanwhile, the E-plane radiation pattern HPBW should be narrower if possible. Therefore, the structure of a surface mountable pyramidal horn antenna is proposed by flaring the cross-section of the SIW-waveguide transition continuously into a large aperture for radiation [30].

Since most microwave integrated circuit modules require a metal housing regardless of the integration technology, this structure can be constructed and installed as part of the external housing as easily as a surface mounted "cap", as shown in Figure 3-6.

The design of an SIW-waveguide transition is basically related to the design of an appropriate transformer that effectively confines guided-wave fields between different waveguiding structures. Because the fundamental waveguiding mode within the SIW is quasi TE10 mode, the electric fields are mainly confined between the top and bottom metal layers of the dielectric substrate. The transition to a rectangular waveguide

operating with a fundamental TE10 mode would require the design of a stepped

waveguide quarter-wave impedance transformer.
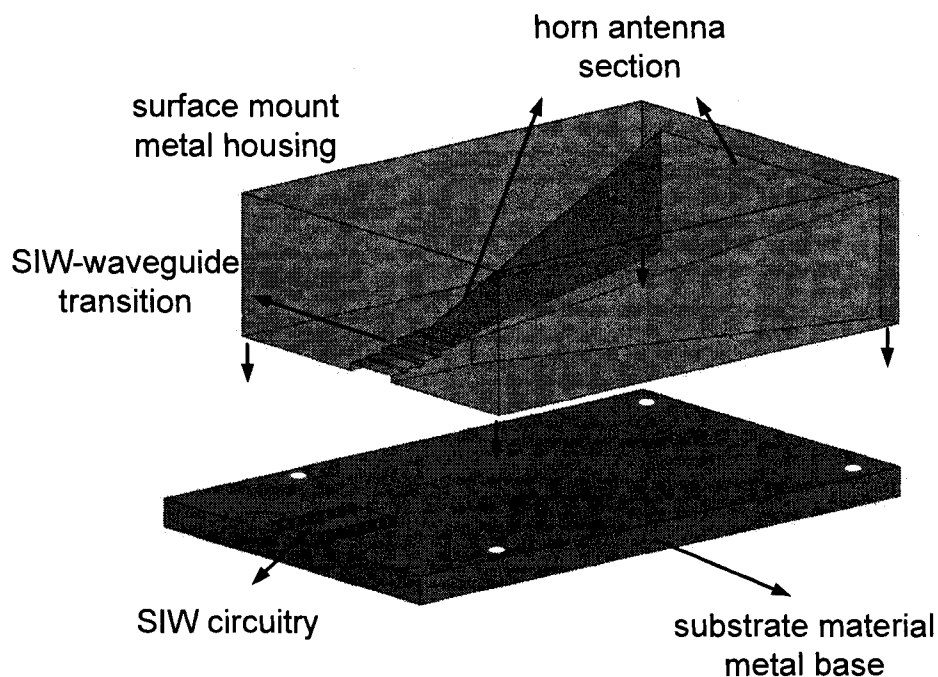
Figure 3- 6. A surface mountable horn antenna and transition to substrate-integrated-waveguide.

The design theory of a stepped waveguide quarter-wave impedance transformer

makes use of a multiple reflection scheme which has been well documented in [43]. The

impedances of each transformer section are first synthesized based on this theory and

then a full wave simulation is deployed for optimization. With respect to the selection of

the waveguide and SIW characteristic impedances, the impedance defined by power and

current, i.e. $Z_{p\text{-}i}$ as formulated by (3.8), is chosen because it is well-defined for a

waveguide port, and the power and current are computed over the area of the port. Also,

the power-current impedance definition is able to meet the design requirements so as to include the effect of narrow wall thickness on the waveguide impedance.

$$Z_{P-i} = \frac{\pi^2}{8} \frac{b}{a} \frac{\sqrt{\frac{\mu}{\varepsilon}}}{\sqrt{1-(\frac{\lambda_0}{2a})^2}} \qquad (3.8)$$

A back-to-back third-order Chebychev prototype is designed as shown in Figure. 3-7. The substrate under study is chosen as duroid/RT5880 with ε_r=2.2 and a thickness of 60 mils. The discontinuity between the interfaces of the SIW section and waveguide section does not pose severe a problem as suggested from the simulation, resulting in a low insertion loss connection as shown in Figure 3-8. This is because the height difference between the two waveguiding structures is so small that neither significant radiation nor reflection can happen at these discontinuities.

Special attention must be paid to the parasitic susceptance, which is caused by the discontinuity between different waveguide steps. The presence of this susceptance will affect both magnitude and phase of individual step reflection coefficient as well as that of transmission coefficient. An extra phase shift is created by those discontinuities in addition to those due to the propagation distance. To improve the performance of the transition, each section can be optimized by shortening their physical length by half the electrical length which corresponds to this extra phase shift [44]. A full wave analysis of the transformer is carried out by using Ansoft HFSS software package to fine tune the length of each section. An average shortening of 6% is applicable in this design. Detailed design parameters are summarized in Table. 3-1. Simulation results of an

optimized back-to-back transition and un-optimized one are shown in Figure. 3-8. It is observed that more than 10 dB improvement is achieved in the design band from 23 GHz to 26 GHz.
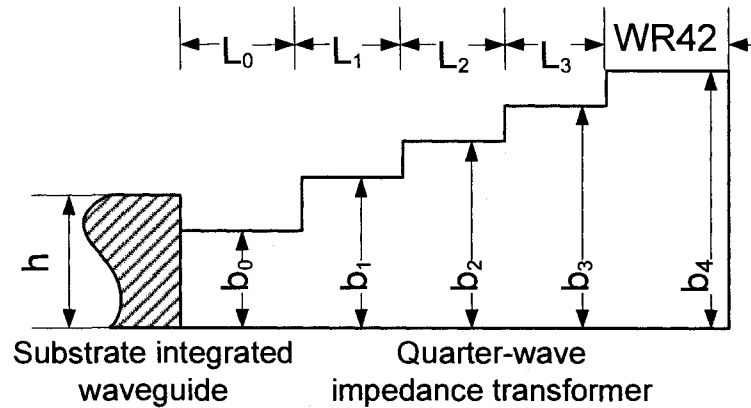
Figure 3- 7. Schematic view of an SIW-waveguide transition design.

Table 3- 1. Design parameters of the SIW-waveguide transition.

Geometry Symbol	Quantity (mm)
L0	3.56
L1	3.56
L2	3.54
L3	3.54
b0	1.10
b1	1.70
b2	2.70
b3	3.90
b4	4.32
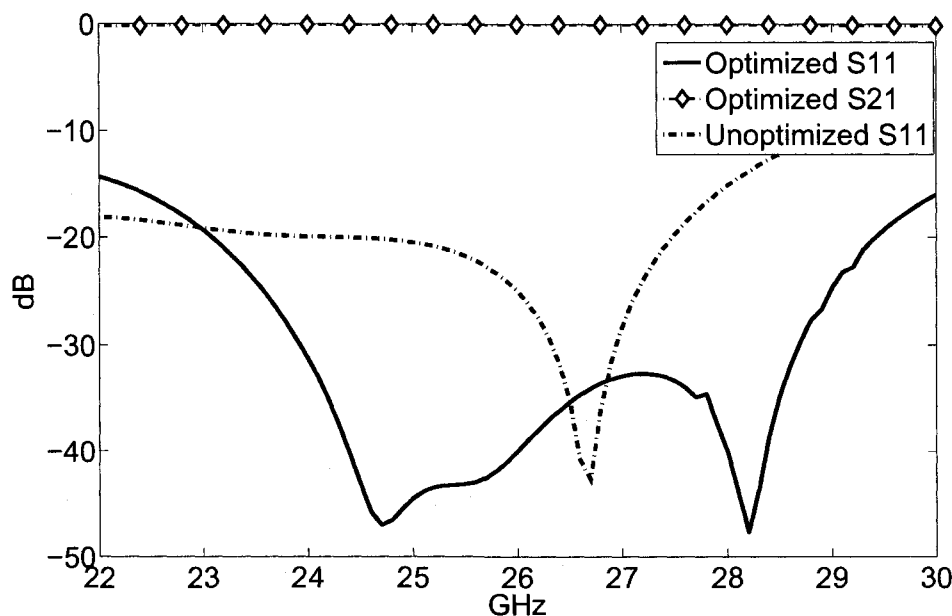
Figure 3- 8. Simulated S parameters of an SIW-waveguide back-to-back transition.

A surface mountable horn antenna itself is designed and fabricated in this work. With the SIW-waveguide transition, the standard waveguide port of the transition is flared into a large opening and forms a horn. Because of the surface mountable profile, the antenna can be fabricated together with the metal housing for the planar microwave integrated circuits and the installation of the horn antenna is as easy as a "cap" on top of the metal base. The radiation pattern design theory is similar to the aperture radiation theory of H-plane sector horn. Detailed design parameters are listed in Figure 3-9 and Table 3-2. A photograph of the fabricated antenna prototype is shown in Figure 3-10. An extra metal layer is added around the aperture of the horn to reduce the back-scattering caused by edge diffraction effect. The antenna radiation patterns are measured in a compact-range anechoic chamber with 1-degree azimuth angle and elevation angle

resolution. Measured results in the two principal planes, i.e. the H-plane and E-plane as well as the input matching of the horn are shown through Figure. 3-11. to Figure. 3-13.
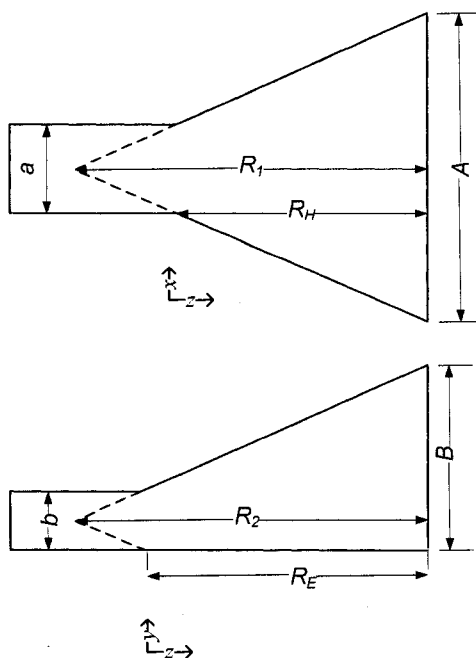
Figure 3- 9. Design parameters of surface mountable horn antenna (not drawn to scale).

Table 3- 2. Design parameters of the surface mount horn.

Geometry Symbol	Quantity (Unit: mm)
a	10.67
b	4.37
A	56.12
B	21.74
R_E	68.02
R_H	68.02
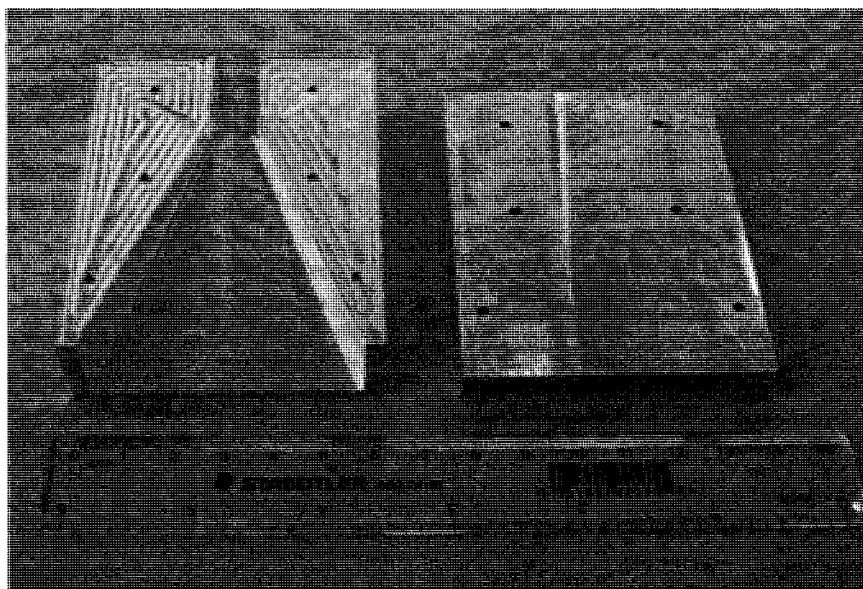
Figure 3- 10. Photograph of a surface mountable horn antenna.
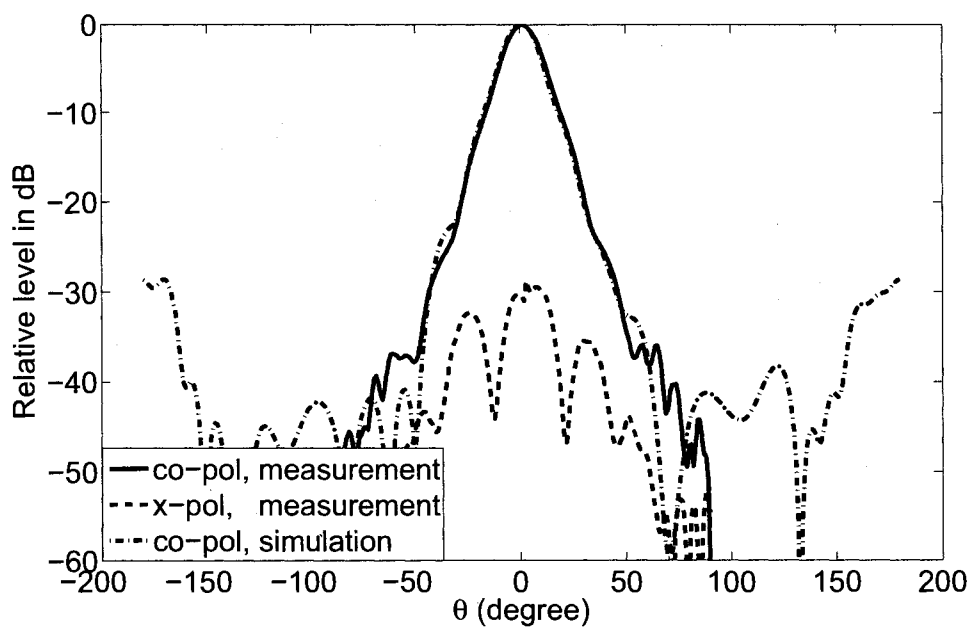
Figure 3- 11. Measured and simulated H-plane radiation pattern.
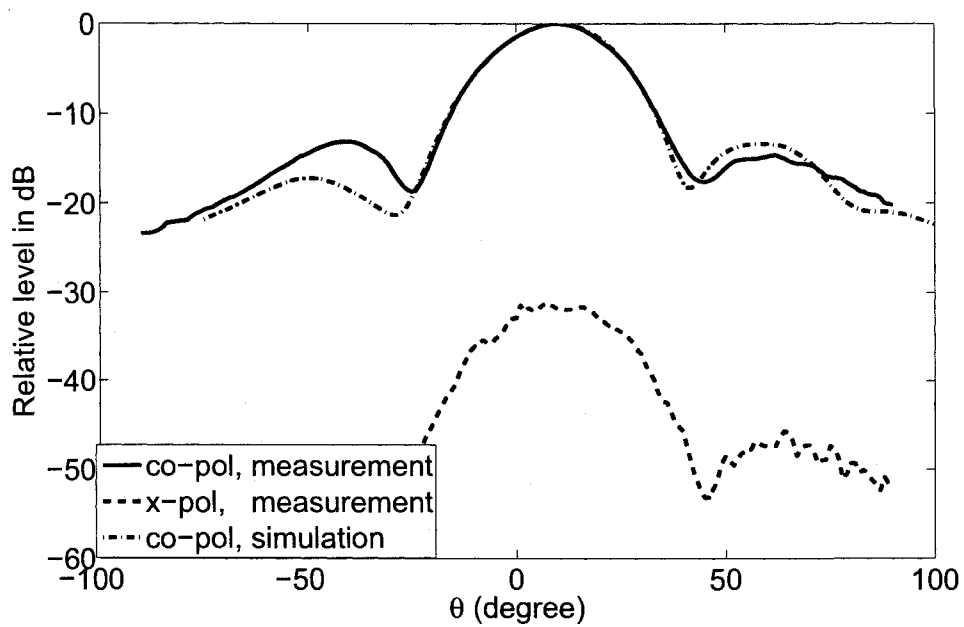
Figure 3- 12. Measured and simulated E-plane radiation pattern.
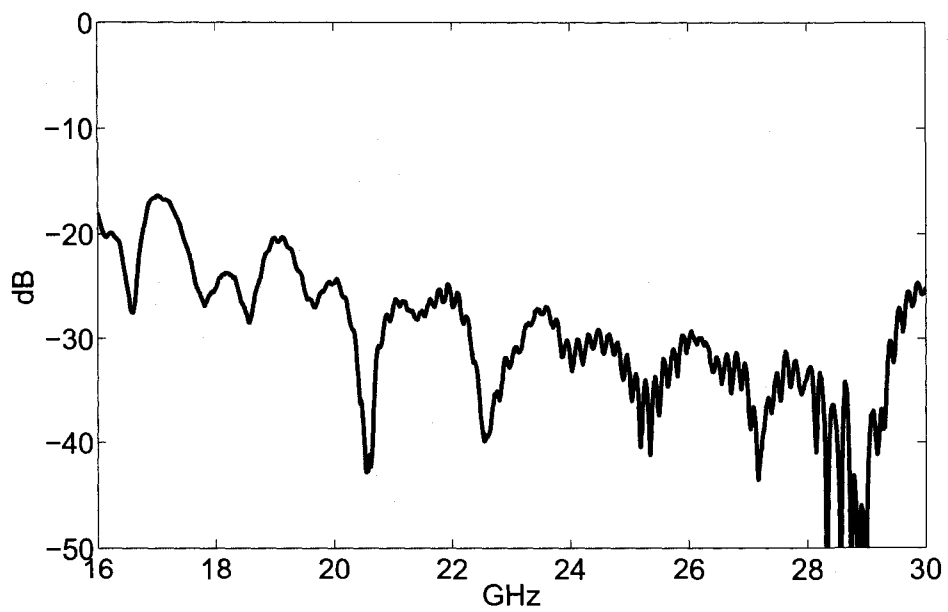
Figure 3- 13. Measured input S11 magnitude of the surface mount horn.

It can be read that the HPBW at H-plane is about 15°. At E-plane the HPBW is about 27°, which are significantly narrower, compared to an H-plane sector horn, because of the larger E-plane aperture opening. The cross-polarization levels in the main beam at both planes are below 30 dB. Meanwhile, the input port matching of the horn also shows a wide bandwidth performance.

3.3 SIW Slot Array

The above-mentioned two types of horn antennas demonstrate interesting characteristics for radar application. However, a limitation exists, i.e. both antennas do not possess a complete planar profile. Both the non-planar surface mountable horn and the quasi-planar H-plane integrated sector horn have to be interconnected with other planar MICs through a transition. This means the fabrication of a complete front-end system cannot be accomplished within one process. Because the objective of system level integration remains the highest priority, some compromises must be made to meet this goal. Generally, two types of planar antennas are potentially available for consideration, i.e. a microstrip patch array and an SIW-fed slot array. Microstrip patch array has the advantage of easy-fabrication (standard photolithographic process) and low cost. However, the maximum gain is limited because of the large transmission losses of microstrip. Therefore, most arrays possess a relatively low radiation gain. On the other hand, SIW-fed slot array essentially is a waveguide slot array antenna integrated on a piece of substrate through SIW technology, which provides a potential for designing a highly directive and high gain antenna. Therefore, the objective of designing an SIW slot

array antenna is proposed. The advantages of using SIW technology on slot array design are obvious. The traditional expensive milling process required for metallic waveguide slot array fabrication can now be exchanged with a conventional photolithography PCB fabrication process. Also, the fabricated SIW slot array has a completely integrated profile, which makes it an attractive option for an integrated system. A schematic view of the proposed SIW slot array is shown in figure below.
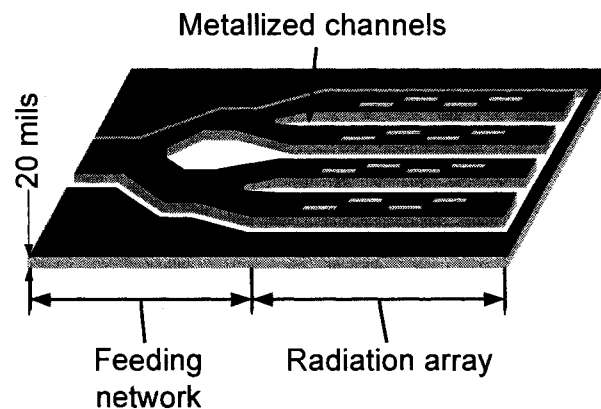
Figure 3- 14. Schematic view of an SIW slot array antenna. (Not drawn to scale).

Although a similar structure was reported in [45], the equivalent circuit of the radiation element was analyzed in detail in [46]. Research on design theory of waveguide feed slot array dated back in 1940s' when it was invented by Watson at McGill University around 1946 and 1947. The detailed design theory was developed later and documented in [47, 48]. A uniformly-excited slot array consists of off-centered longitudinal-cutting slots spaced every half guided wavelength along the longitudinal direction, which disturb transverse surface currents when the TE_{10} mode is excited inside the waveguide. Short-ended slot array is essentially a narrow band antenna because of

the resonance characteristics of the radiation slots. The key design approach is to model the slot cut on the broad wall as a shunt element [49] and the entire array is modeled as a parallel of the shunt element. The radiation pattern can then be calculated based on the slot voltage distribution [50]. If the slots are spaced half a guided wavelength apart each other, the array is said to be standing-wave fed. However, the universal design curves for the full height air-filled waveguide will be quite different for a dielectric material filled SIW [46]. Accurate equivalent circuit parameters extraction is an important step in designing an SIW slot array.

Considering an off-center slot cut on the broad wall of a waveguide, the design geometry parameters are shown in the Figure 3-15. It was shown that the scattering off the slot is symmetrical [51], which implies that the equivalent circuit of the slot can be modeled as a shunt element in a two-wire transmission line system.
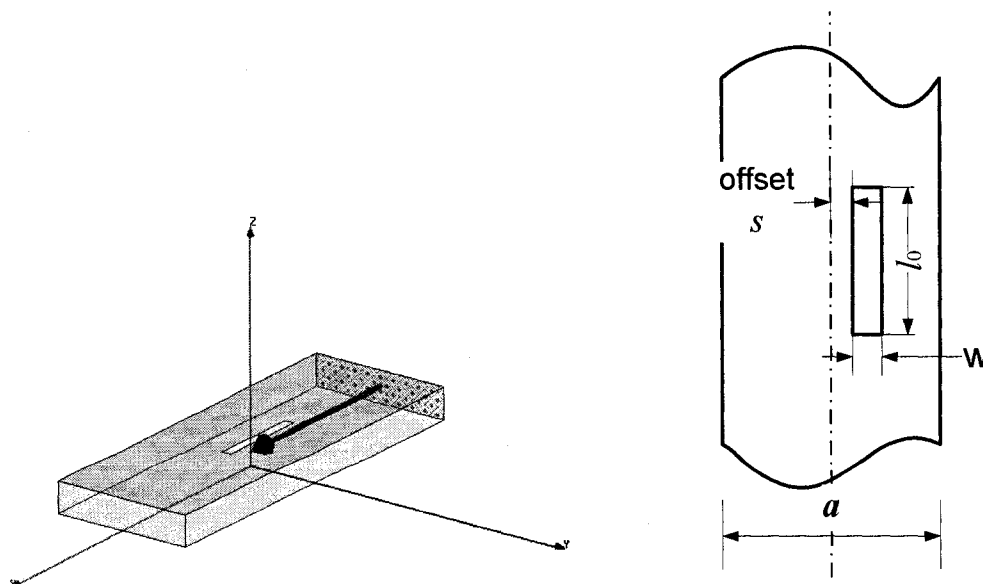
Figure 3- 15. Single slot model. a) A 3-D perspective. b) A top-view perspective. (Not drawn to scale).

$$x=-\lambda_g/4 \qquad x=0 \qquad x=\lambda_g/4$$
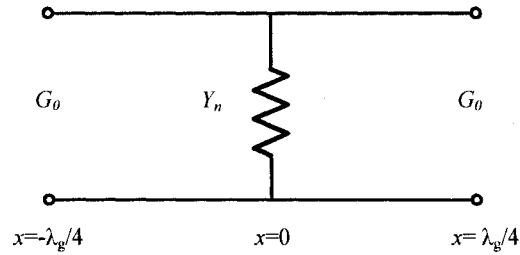
Figure 3- 16. Equivalent circuit of a single slot embedded in SIW.

For the equivalent circuit topology as shown above, there is $S_{11} = S_{22}$ and $S_{12} = S_{21}$. Therefore the parallel admittance is [46]

$$y = \frac{Y_n}{G_0} = G + jB \qquad (3.9)$$

where G_0 is the waveguide port conductance.

Full wave slot model was then constructed to extract the equivalent normalized admittance. A very useful form to express the admittance data of a single slot was suggested in [47], where extracted slot admittance data are assembled with slot offset and length as parameters. Ansoft HFSS software package is used to extract the S parameters. The resonance is confirmed when Y/G_0 is pure real. Under this circumstance, $Y/G_0 = g_r$, $G = G_r$ and the slot length is defined as resonant length l_r.
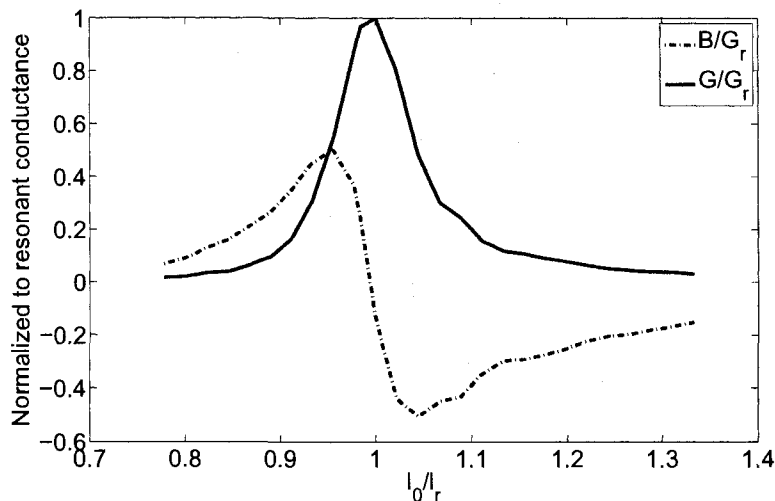
Figure 3- 17. Resonance characteristic of a 0.3 mm offset slot on SIW.

The purpose of this step is to obtain the slot length and offset for a resonant slot, which will be used later as an initial value to achieve a matched array input. The extracted ratio of single slot conductance normalized to SIW port admittance as a function of the slot offset is plotted in Figure 3-18. The physical understanding of the increase of equivalent conductance as a function of increasing slot offset is quite straightforward. As the slot is placed more off-center, the more surface current it disturbs, which makes the slot a stronger radiation element. Because the dissipated power due to radiation can be described as $P_{rad} = V_0^2 \cdot G_r$, where V_0 is waveguide mode voltage being unchanged, therefore it is clear that a stronger radiation relates to a larger resonant conductance G_r.
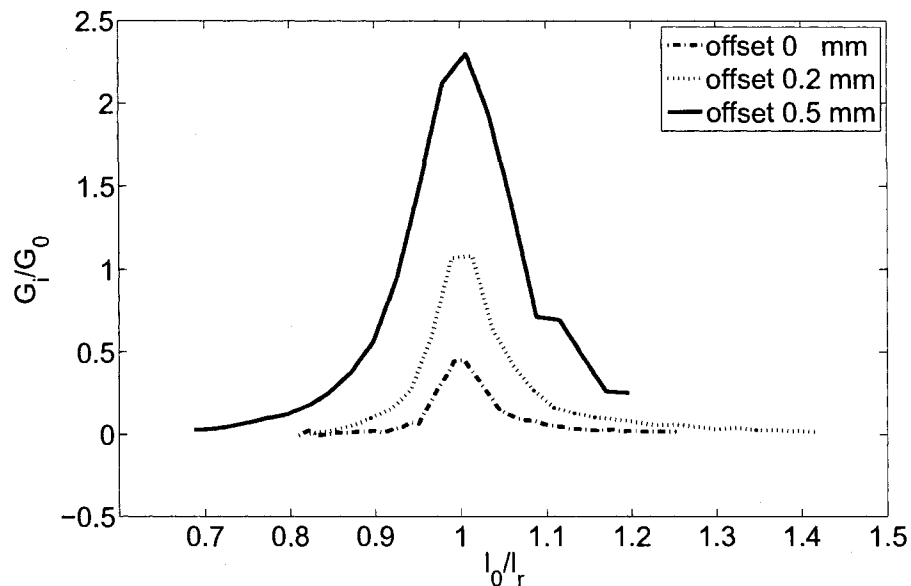
Figure 3- 18. Normalized SIW slot resonant conductance.

The extracted ratio of single slot susceptance normalized to SIW port admittance as a function of the slot offset is shown in Figure 3-19. It is observed that the susceptance of the slot also increases as the slot offset is increased. This is because as the slot is placed farther from the SIW center, the more discontinuity it creates, therefore dissipative higher modes are created which contribute to the larger susceptance part of the shunt element in the equivalent model.
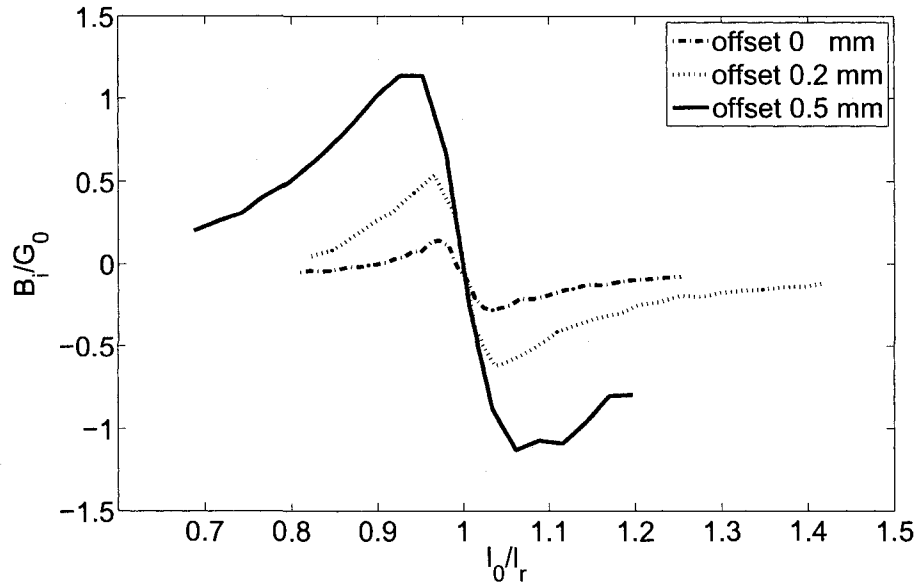
Figure 3- 19. Normalized SIW slot resonant susceptance.

If a specified antenna radiation pattern is desired, each slot length and offset can be

determined based on the slot voltage distribution V_n^s on each slot and the port matching

specification [51]. For a uniformly excited array, when the mutual coupling between

different elements is not considered, each radiation element is to be excited uniformly.

However, in the case of an SIW slot array, where slots are closely spaced to each other,

the mutual coupling effects between each slot should be considered. A careful tuning of

the slot offset and length using HFSS is crucial in the design process. As a matter of fact,

[48] suggested that when mutual coupling effects are considered in the design process,

the final array slots are detuned off-resonance, because mutual coupling creates

susceptance component and this has to be compensated by a reactance component

coming from the off-resonance slot.

An antenna prototype was fabricated on a piece of substrate material. The measured

array input port matching is shown in Figure 3-20.
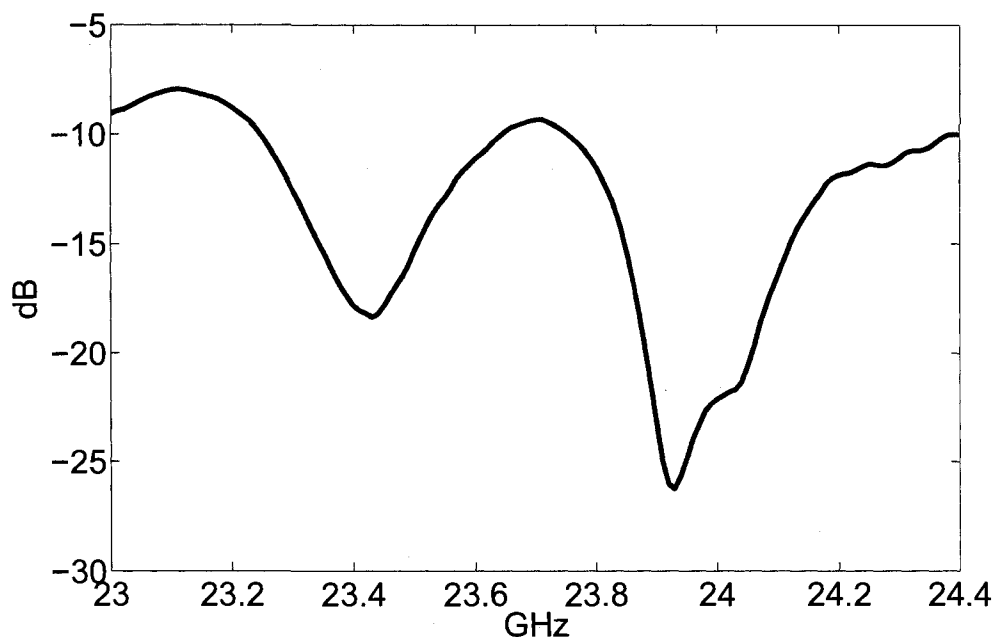
Figure 3- 20. Measured antenna input S_{11} magnitude.

A 10 dB return loss bandwidth ranging from 23.75 GHz to 24.40 GHz (650 MHz) is

achieved. The SIW slot array exhibits a narrow band characteristic with relative

bandwidth around 2.7%. Many reasons contribute to this result. First, the slot itself is a

resonant type radiating element. This is the major reason for the narrow bandwidth. The

bandwidth is further reduced by the mutual coupling between slots. Unless the radiating

slots were to be spaced to form a traveling wave antenna rather than by a half guided

wavelength, the bandwidth of the slot will always remain a narrow band type. The

second major reason of narrow bandwidth is the dielectric filling as well as waveguide

height reducing [48]. To justify this statement, a comparison on the normalized slot resonant conductance is made between a slot etched on an SIW and a slot milled on a classic full-height metallic waveguide, as shown in Figure 3-21. Obviously, the slot on SIW structures possesses a narrower bandwidth compared with the slot on standard metallic waveguides. The practical interpretation of this information is that the fabrication error will have a stronger influence on the slot array matching performance, which explains from another perspective why the SIW slot array exhibits a narrow bandwidth.
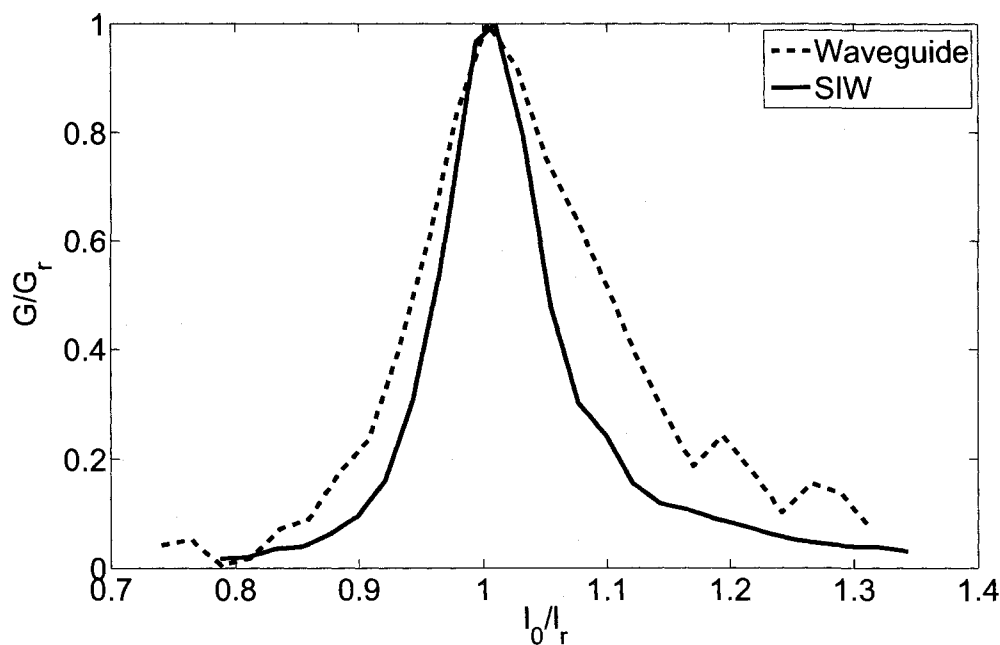
Figure 3-21. Normalized slot conductance on waveguide and SIW.

The measured gain of this antenna is 15.7 dBi at 24.1 GHz. The measured radiation pattern exhibits consistent shape throughout its matching bandwidth. Measured radiation

patterns at 24.1 GHz are plotted below. The measured half-power-beam-width (HPBW) at E-plane is 31° (simulation results indicate 27.02°) and that at H-plane is 37° (simulation results indicate 36.11°). The electric field magnitude across the edge of slot on the E-plane of the fabricated prototype is uniform as expected, which is confirmed by the -13.5 dB first side lobe level. The electric field magnitude across the edge of the slot on the H-plane is a quasi-cosine distribution, as observed from the wider HPBW and the lower first side lobe level.
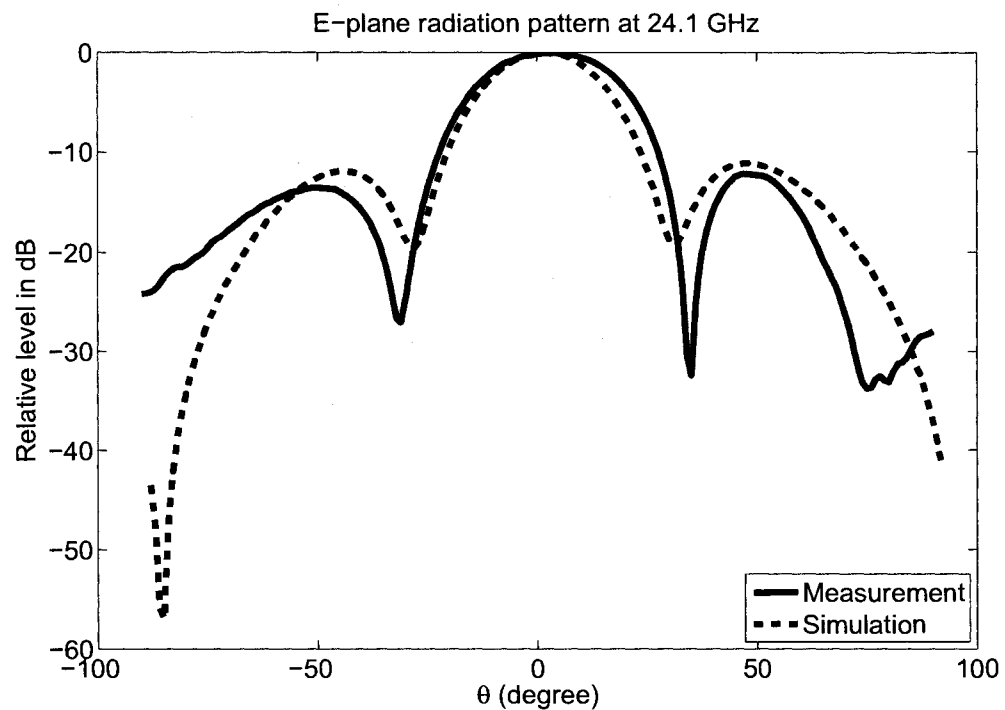
Figure 3- 22. Measured SIW slot array E-plane radiation pattern.
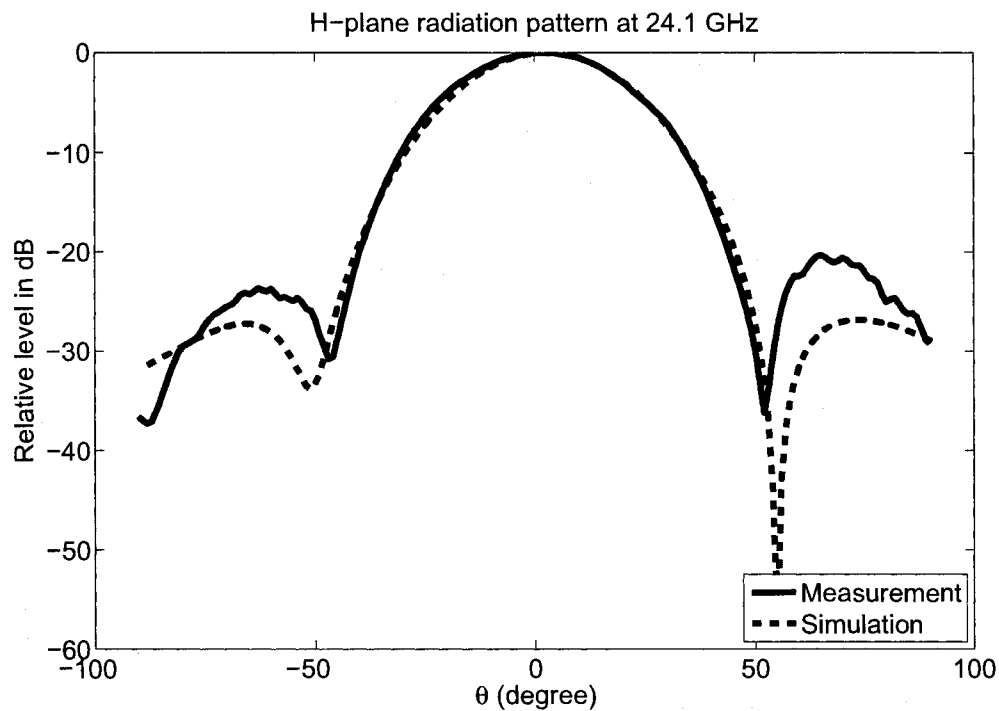
Figure 3- 23. Measured SIW slot array H-plane radiation pattern.

As a final note to this chapter, it is clear there are still many modifications that can be made to improve the performance of this type of antenna. For example, a traveling wave fed slot array would provide wider input matching bandwidth as well as a complete solution of integration. This can be left as a direction for future research on the related areas.

CHAPTER 4 SIW/SIC MIXERS AND SURFACE-VOLUME INTEGRATION

The mixer is one of the most important components in an FMCW radar system. In the radar transmitter, it upconverts base-band signal to RF band. In the radar receiver, the mixer autodynes the reference FM signals from transmitter with the received signals. Because of different functionalities of a mixer in radar system, different performance requirements apply to mixer design. Some common requirements include high frequency conversion gain, high isolation between ports, low port reflection, high linearity, being able to suppress certain orders of harmonics and so on. In an integrated system, there are also integration issues such as a compact profile, facility to integrate with diodes or transistors, possibility to fabricate with a standard photolithograph process, etc. Two different types of mixers are proposed in this work with completely different integration philosophies. One is a 90-deg SIW mixer designed with the major integration approach being SIW. The other mixer is a 180-deg SIC mixer, which is designed with a hybrid integration approach combining microstrip and SIW technologies to achieve an overall optimized performance. A *surface-volume* integration philosophy is implemented in this work. Strict experimental comparison results confirmed that this hybrid integration methodology demonstrates superior characteristics in terms of electrical performances, substrate material usage, and circuitry size and so on compared with a monotonous integration approach. This chapter will discuss the design strategy, integration

philosophy, their advantages and compromises, measurement results and the related analysis of the two mixers.

4.1 SIW Mixer

A 90-deg SIW mixer based on a 90-deg SIW quadrature coupler is designed in this work. Many electrical advantages can be obtained by applying SIW technology. For example, a planar 90-deg quadrature coupler applying microstrip technology normally works at low frequencies only up to 18 GHz or so. This is because of the circuit size limitations at high frequencies, where the line length decreases with increasing frequency, becoming comparable to its width. Therefore, the junction discontinuities become dominant, resulting in a lower performance and rendering the microstrip quadrature coupler almost unemployable at high frequencies. The use of SIW in the making of the hybrid junction easily allows the design of a planar 90-deg quadrature coupler into Ka band. As a good application example of this technology to active devices design, a 90-deg single-balanced mixer based on a SIW coupler is proposed in this work.

The design of an SIW mixer includes the design of an SIW power hybrid junction, i.e. a quadrature coupler, the diodes matching circuits, the transition between SIW hybrid junction and the diodes matching circuits, the transition between the input and output lines and IF output design.

The first decision a mixer designer needs to make is the selection of proper diodes. Although most mixers are less limited by the properties of the diodes than by those of the circuit [52], there are still many considerations of diode selection in terms of performances, ease of integration and cost. A very basic choice is between silicon and GaAs. GaAs diodes have very high cut-off frequency and very good overall performance. However, in the application of design SIW/SIC mixers, where external diodes bias is difficult to apply because the top metal layer of the substrate is also DC grounded due to the conducting SIW side walls, GaAs diodes require more LO power because of their higher barriers. This situation should be avoided because the integrated radar receiver LO comes directly from the integrated transmitter, a scenario where extra amplification is limited and no external power can be requested. Therefore, silicon diodes are considered in this work. Another advantage of choosing silicon diodes are the better LO-port reflection properties because of the lower barriers. Also, by choosing silicon diodes instead of GaAs ones, the mixer will have a lower $1/f$ noise characteristic unique to silicon diodes [52, 53]. For a homodyne FMCW radar receiver, the demodulated signal usually is a low frequency signal in the range of kilohertz, well within the range of $1/f$ noise. Therefore the lower $1/f$ noise the mixer obtains, the more sensitivity the system can achieve.

The second decision which needs to be made related to diodes is the selection of the diodes package form. Bare chips diodes have small series resistance but difficult to integrate within a substrate. Packaged diodes are easy to handle but posses a larger

parasitic inductance. The compromise being made is the beam-lead package form, which yields adequate performances while low in parasitic.

The diodes used in this mixer are silicon beam-lead Schottky diodes. The admittance of the diode can be calculated based on their equivalent circuit. Different LO drive power will excite diodes with different self-bias current leading to different admittance. The equivalent circuit of the diodes with 1 mA self-bias current is shown in the figure below [54].
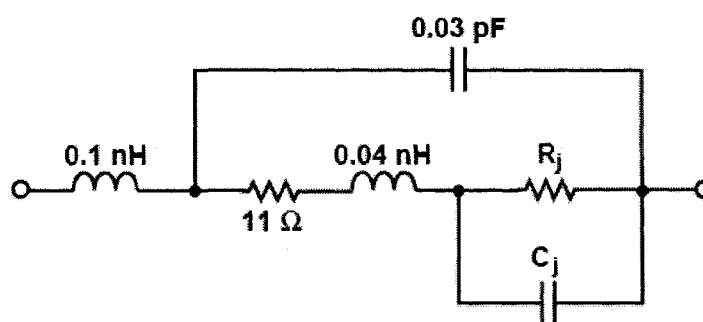
Figure 4- 1. Equivalent circuit of a beam lead Schottky diode.

Diodes junction resistance and capacitance with different self-bias current are shown in the following table.

Table 4- 1. Beam lead Schottky diodes equivalent circuit model parameters [54].

	1mA self bias	1.5mA self bias	3mA self bias
R_j (Ω)	267	232	150
C_j (pF)	0.11	0.11	0.12

Their respective admittance can be calculated as shown in the following Y Smith

chart. Diode matching circuitry can then be designed based on these calculations.

Self bias current=1.0 mA

freq (1.000GHz to 26.00GHz)

| m1 |
| freq=24.00GHz |
| admittance=0.621 / -117.796 |
| impedance = Z0 * (0.313 - j0.559) |

a).

Self bias current=1.5 mA

freq (1.000GHz to 26.00GHz)

| m1 |
| freq=24.00GHz |
| admittance=0.596 / -117.801 |
| impedance = Z0 * (0.337 - j0.552) |

b).

Self bias current=3.0mA

freq (1.000GHz to 26.00GHz)

| m1 |
| freq=24.00GHz |
| admittance=0.503 / -118.557 |
| impedance = Z0 * (0.431 - j0.510) |

c).
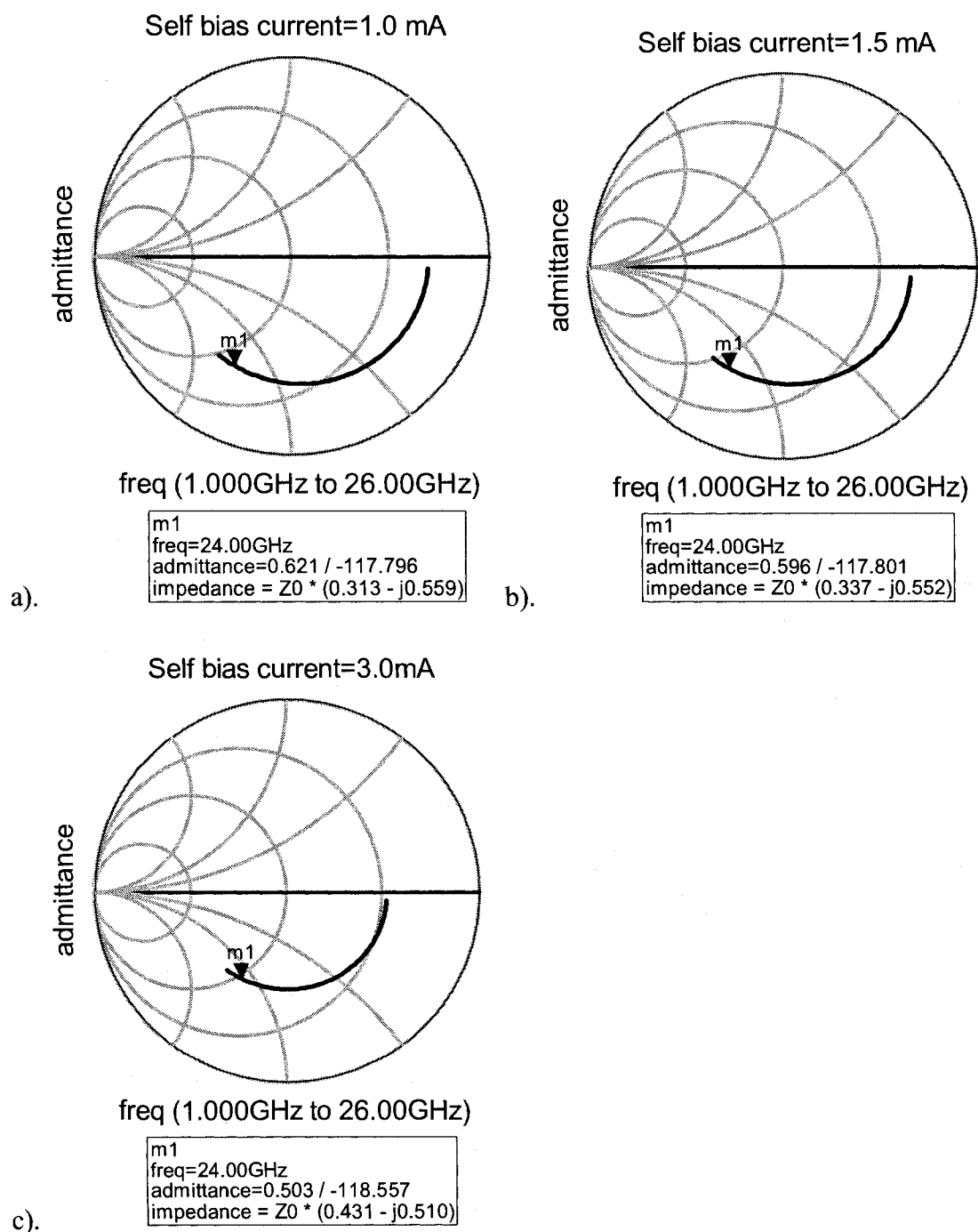
Figure 4- 2. a)-c) Beam lead Schottky diodes admittance as a function of the bias current.

The SIW power hybrid junction is designed using a side wall coupling-based directional coupler. The detailed schematic drawing of the 3-dB SIW 90° power hybrid junction is shown in Figure 4-3 as below.
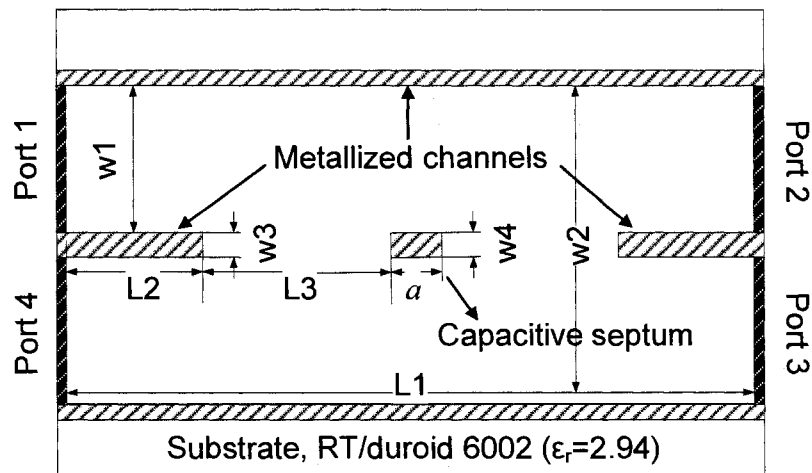
Figure 4- 3. Geometrical top view of 90-deg SIW hybrid junction (not drawn to scale).

A simplified design strategy can be modeled as both TE10 mode and TE20 mode are excited in the broad waveguide section [55]. Because TE10 mode and TE20 mode are experiencing different phase shift, and the output electric field at port 2 and port 3 has 90 degree phase difference, the dimension of the broad waveguide section can be determined by equalizing the power at port 2 and port 3. Suppose the input signal excites two modes equally, then at the input of the coupler, the electric field of TE10 E_1' and the electric field of TE20 E_1'' has the same amplitude and direction; while at the output of the coupler, the electric field of TE10 E_2' and electric field of TE20 E_2'' are related by

$$E_2' = E_1' e^{-j\frac{2\pi}{\lambda_g'}l}$$

$$E_2'' = E_1'' e^{-j\frac{2\pi}{\lambda_g''}l} = E_1' e^{-j\frac{2\pi}{\lambda_g''}l}$$

where λ_g' and λ_g'' are guided wavelength of TE10 and TE20 respectively, E_1' and E_1'' are electric field of TE10 mode and TE20 mode at port 1.

The port 2 output electric field is given by

$$E_2 = E_2' + E_2'' = E_1'(e^{-j\frac{2\pi}{\lambda_g'}l} + e^{-j\frac{2\pi}{\lambda_g''}l})$$

$$= E_1' e^{-j(\frac{2\pi}{\lambda_g'}+\frac{2\pi}{\lambda_g''})\frac{l}{2}}[e^{j(\frac{2\pi}{\lambda_g'}-\frac{2\pi}{\lambda_g''})\frac{l}{2}} + e^{-j(\frac{2\pi}{\lambda_g'}-\frac{2\pi}{\lambda_g''})\frac{l}{2}}] \qquad (4.1)$$

$$= 2E_1' \cdot \cos[(\frac{2\pi}{\lambda_g'}-\frac{2\pi}{\lambda_g''})\frac{l}{2}] \cdot e^{-j(\frac{2\pi}{\lambda_g'}+\frac{2\pi}{\lambda_g''})\frac{l}{2}}$$

The port 3 output electric field is given by the vector summation of E_3' and E_3'' where

$$E_3' = E_2' \text{ and } E_3'' = -E_2''$$

$$E_3 = E_3' + E_3'' = E_2' - E_2'' = E_1'(e^{-j\frac{2\pi}{\lambda_g'}l} - e^{-j\frac{2\pi}{\lambda_g''}l})$$

$$= E_1' e^{-j(\frac{2\pi}{\lambda_g'}+\frac{2\pi}{\lambda_g''})\frac{l}{2}}[e^{j(\frac{2\pi}{\lambda_g'}-\frac{2\pi}{\lambda_g''})\frac{l}{2}} - e^{-j(\frac{2\pi}{\lambda_g'}-\frac{2\pi}{\lambda_g''})\frac{l}{2}}] \qquad (4.2)$$

$$= 2j \cdot E_1' \cdot \sin[(\frac{2\pi}{\lambda_g'}-\frac{2\pi}{\lambda_g''})\frac{l}{2}] \cdot e^{-j(\frac{2\pi}{\lambda_g'}+\frac{2\pi}{\lambda_g''})\frac{l}{2}}$$

To satisfy the equal power coupling requirement, we have $|E_2| = |E_3|$, as expressed by

$$\cos[(\frac{2\pi}{\lambda_g'}-\frac{2\pi}{\lambda_g''})\frac{l}{2}] = \sin[(\frac{2\pi}{\lambda_g'}-\frac{2\pi}{\lambda_g''})\frac{l}{2}] \text{ which leads to}$$

$$l = \frac{1}{4(\frac{1}{\lambda_g{}'} - \frac{1}{\lambda_g{}''})} \tag{4.3}$$

To compensate the reactance introduced by the discontinuities of the aperture, a conductive metal post at the center of the coupler is inserted [56, 57]. The transverse dimension of the metal septum is determined by the minimum achievable fabrication resolution. The longitudinal dimension of the septum a, however, has a strong influence over the input port matching and the two port coupling. A detailed full wave study of the size of the metallised septum is done using Ansoft HFSS. The summarized simulation results on RF/LO port reflection, isolation, coupling and phase shifting are shown in the following figures. It is observed from Figure 4-4 that an input port return loss better than 20 dB over 3 GHz frequency band can easily be achieved.

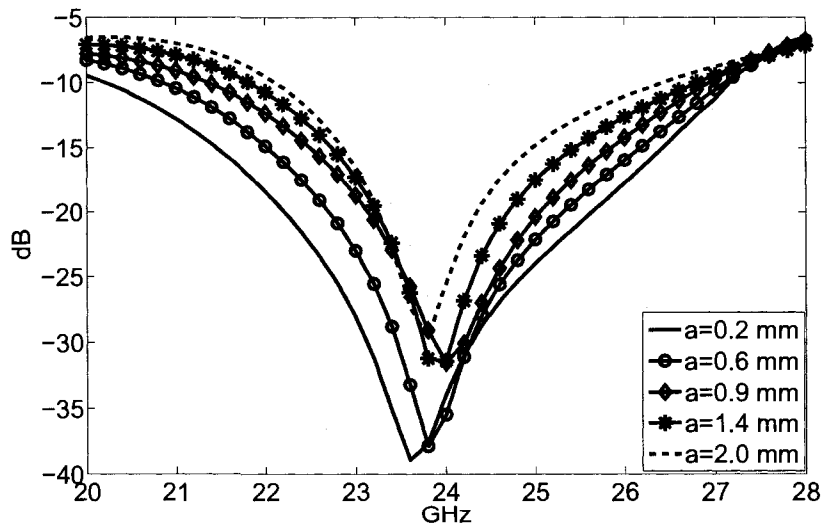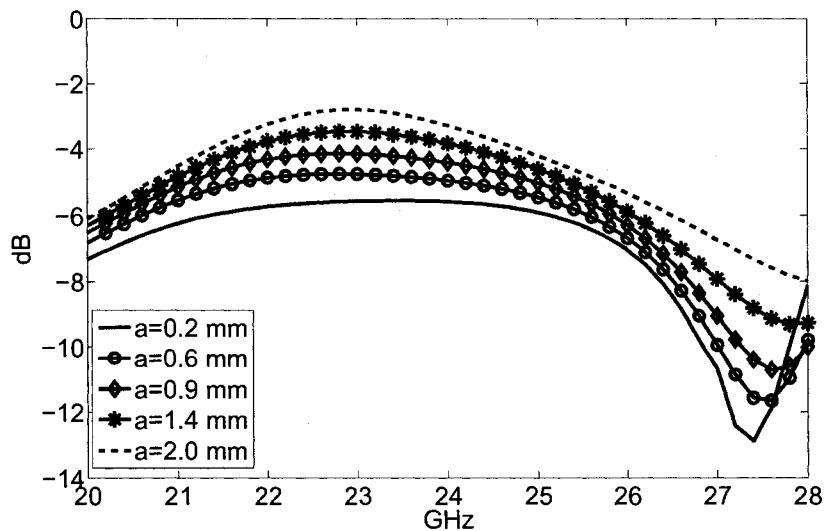Figure 4- 4. 90-degree SIW coupler input port $S11$ magnitude.

Figure 4- 5. 90-degree SIW coupler *S*21 port magnitude.

Port 2 is the through port which is supposed to have a 3 dB coupling coefficient. The

simulated results in Figure 4-5 show that the coupling coefficient varies from -2.40 dB

to -4.67 dB as *a* varies from 0.2 mm to 2.0 mm as observed.
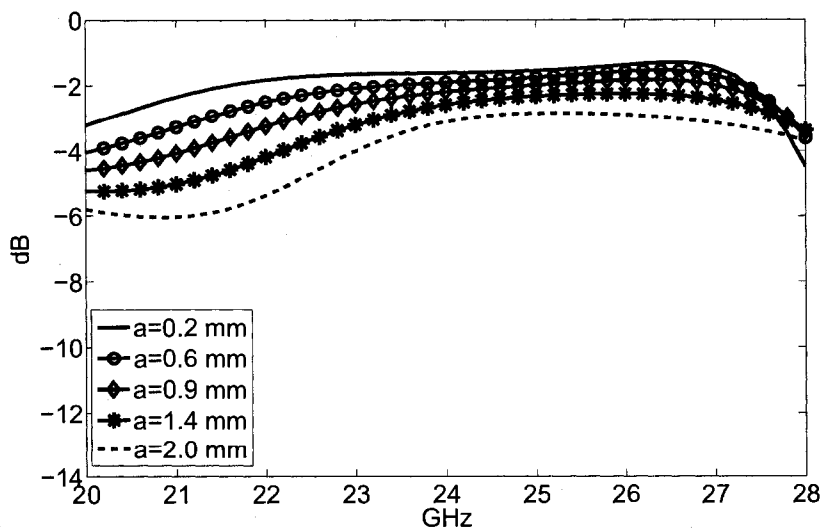
Figure 4- 6. 90-degree SIW coupler coupled port magnitude.

Port 3 is the quadrature coupling port of the coupler. 3-dB power coupled from the input port as well as 90 degree phase difference to port 2 should be obtained. As shown in Figure 4.6, a -2.33 dB to -4.0 dB coupling is achieved when *a* varies from 0.2 mm to 2.0 mm.
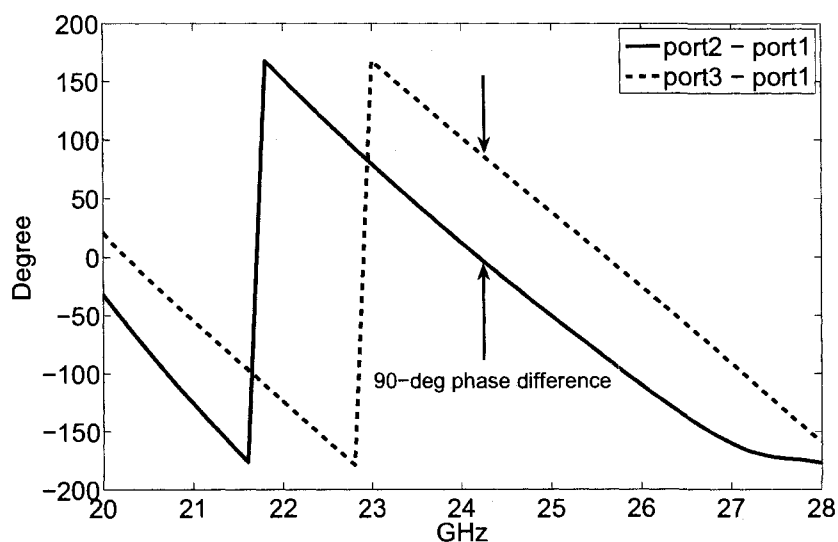
Figure 4- 7. 90-degree SIW coupler S21 and S31 phase.

The phase shift between the input port to either the through port or the coupled port is not important in a balanced mixer design. However, the 90-deg phase difference between the through port and the coupled port, i.e. port 3 and port 2, is critical as it determines the rejection of superior responses. The simulated result in Figure 4-7 shows a clear 90 degree phase difference across the interested band of frequencies.

The 90-deg mixer LO-RF isolation is mainly determined by the isolation of its coupler. The maximum port 4 isolation to port 1, as shown in Figure 4-8, varies from -30 dB to -40 dB as *a* varies from 0.2 mm to 2.0 mm. It is important to note that the maximum isolation is achieved at the center design frequency. Because of this, it makes

the 90-deg mixer mostly applied in a situation where the LO and RF frequencies are close to each other.
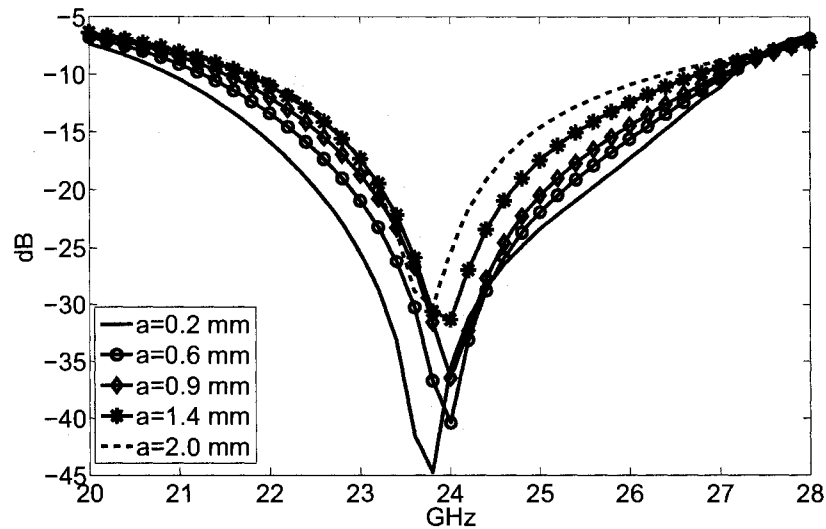
Figure 4- 8. 90-degree SIW coupler isolated port magnitude.

An electric field magnitude spectrum plot is given in Figure 4-9. It is observed that when the port 2 electric field magnitude reaches the maximum, the electric field magnitude at port 3 reaches minimum. A 90 degree electrical length on the propagation direction exists between the maximum and the minimum. The isolated port 4, on the other hand, shows very low level electric field distribution. A summary of fabrication details for a 90-deg coupler prototype is listed in the following table.
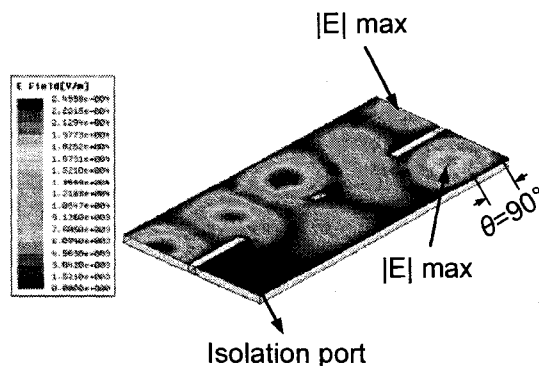
Figure 4- 9. 90-degree SIW coupler E-field magnitude at 24.2 GHz.

Table 4- 2. Design parameters of the 90-degree SIW hybrid junction

GEOMETRY SYMBOL	QUANTITY (MM)
L1	20.00
L2	4.00
L3	5.55
a	0.90
W1	4.75
W2	10.00
W3	0.50
W4	0.50
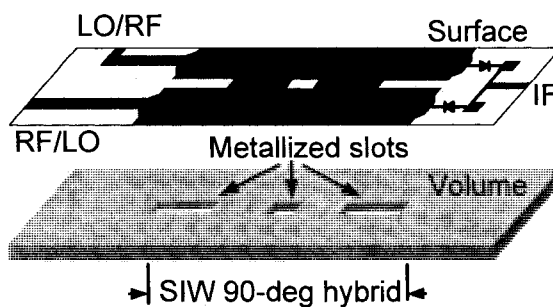
Figure 4- 10. 3-D schematic view of a 90-degree SIW mixer. (Not drawn to scale).

A 3-D descriptive view of the SIW mixer is shown in Figure 4-10. The power hybrid junction of the mixer is an SIW 90-deg directional coupler. At one side of the coupler, the LO port and the RF port of the SIW section are transited into microstrip line through

an impedance matching transformer to facilitate the measurement. At the other side of the coupler, the top metal layer of the SIW section is stretched out to integrate two diodes. The other side of the diodes are integrated with an impedance matching stub. Because the two diodes are orientated in an anti-parallel orientation, the IF signal should be coupled out directly. It is worth noting that a high impedance DC direct coupling technique is used instead of an AC coupling technique. This is because an AC coupling involves a capacitance which blocks the DC components generated by the LO self coupling. However, this capacitance also adversely affects the IF signals with low frequencies. Keep in mind that in a zero-IF FMCW radar system, when the target is close to the radar or the modulation frequency is low, the direct down-converted IF signals are of low frequency. Therefore the filtering effect introduced by the AC coupling could downgrade radar ability to detect very weak returned target signal and is not adopted in this design.

A circuit level co-simulation combining the diodes, the matching stubs, the 3-dB 90-deg SIW coupler, which has been modeled as a SNP junction, is performed using ADS harmonic balance engine. Primitive results on mixer conversion gain, LO driven level, P1dB saturation point can be obtained through this part of the work.

The mixer performance including conversion gain, RF port reflection, LO-RF port isolation, RF-IF port isolation, and input-intercept-point-third-order (IIP3) and the RF port P1dB power saturation point are carefully measured. In the experimentation of mixer frequency and conversion gain, two signal sources plus a spectrum analyzer are used in this work. As a matter of fact, many of the above mentioned mixer

characteristics can be measured using a network analyzer. An additional section on the mixer measurement using network analyzer is given at the end of this chapter.

A photograph of the mixer measurement setup using the spectrum analyzer is shown in Figure 4-11. The mixer is clamped by a universal test fixture with a right angle launcher. The offset ability of the fixture jaws provides freedom to design the mixer RF port and IF port with an offset. The measurement of the mixer conversion gain is performed with a fixed RF frequency at 24.1 GHz and a fixed LO frequency at 22.6 GHz. Because mixer frequency conversion gain is a strong function of the LO driving power level, the frequency conversion gain should be measured with the LO power level as a sweeping parameter. The LO power level is also swept from 0 dBm to 14 dBm. The RF power level is swept from -6 dBm to 8 dBm. Measured conversion gain data set with LO of +7 dBm is plotted as shown in Figure 4-12.
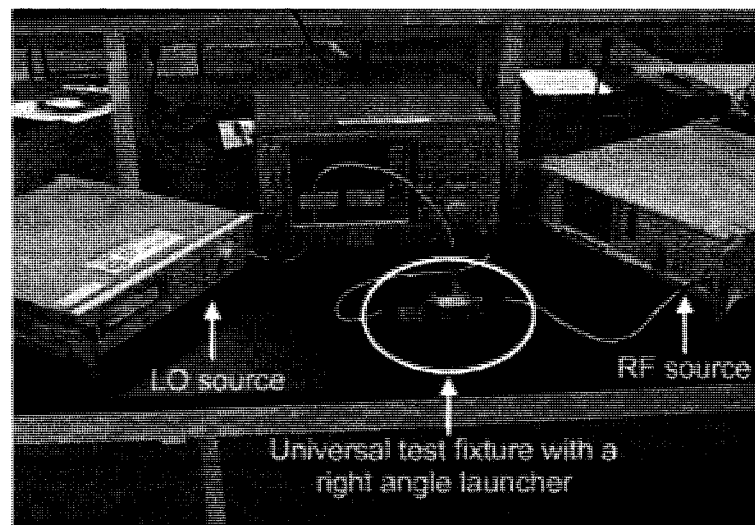
Figure 4- 11. Mixer measurement setup using spectrum analyzer.
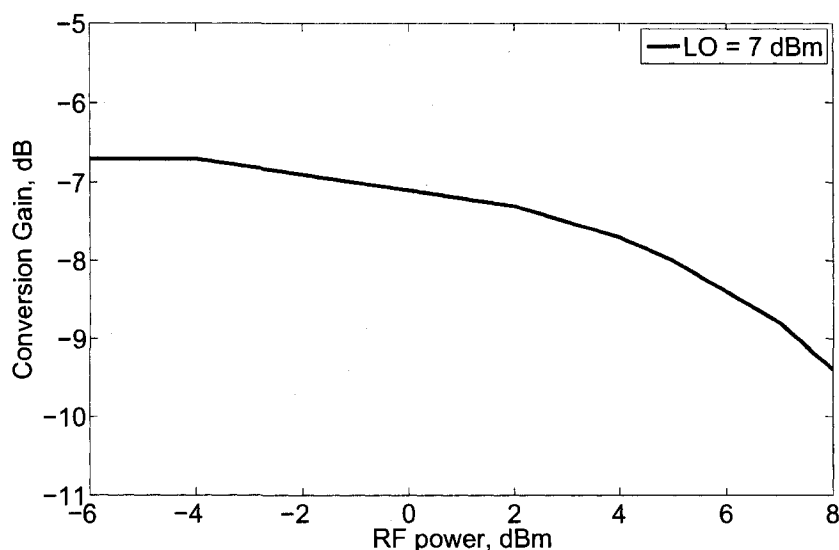
Figure 4- 12. Measured SIW mixer frequency conversion gain with fixed RF frequency and fixed LO frequency.

The mixer operates well with as low as 7 dBm LO driven level. This is because the lower barrier of the silicon diodes requires less LO power as compared to GaAs diodes. It is demonstrated that the mixer exhibits a linear frequency conversion response as RF power increases from -6.0 dBm to -4.0 dBm with the maximum frequency conversion gain of -6.7 dB. This is almost unchanged as the RF power sweeps from -6.0 dBm to 0 dBm. As the RF power level continues to increase, the mixer starts to saturate and the conversion gain starts to decrease. The mixer RF port input $P1$dB with 7 dBm LO input level is expected to be higher than 8 dBm, because the conversion gain drops down only by 0.6 dB when the RF port input level is increased from 7 dBm to 8 dBm.
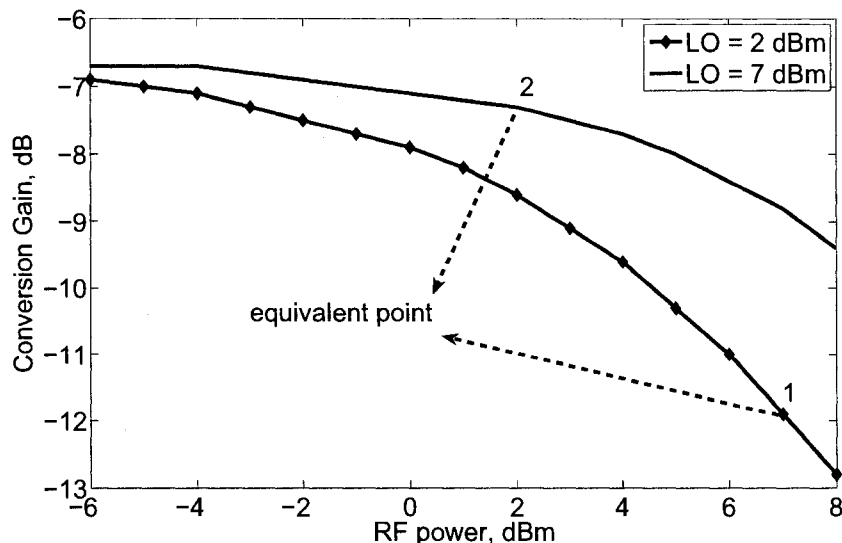
Figure 4- 13. Measured mixer frequency conversion gain data interpretation with 2 dBm LO and 7 dBm LO.

It is interesting to notice that the conversion gain keeps dropping for low LO level driving, even when the RF port level has increased to 7 dBm, as indicated by point 1 shown in Figure 4-13. This seems to violate the physical principle of the 90-deg single balanced mixer, where the RF port and LO port are electrically exchangeable, because the conversion gain is expected to be at the same level when LO is biased with 7 dBm. However, if we take another look at the definition of the frequency conversion gain, which is defined by the power ratio between the power at the IF port and the power at the *RF port*, we shall notice that this definition does not distinguish the *real* RF port and LO port. Actually, the illogical value of point 1 is just because of the good symmetry of this SIW mixer. The physical understanding of the measurement data of point 1 is the mixer is biased from the RF port when RF port level is 7 dBm. The real conversion gain is to be understood as the ratio between IF port power level of -5.7 dBm and the LO port

power level of +2 dBm, i.e. -7.7 dBm, which is almost in the same level as the measured

conversion gain when the mixer is biased from the LO port with +7 dBm as shown of

point 2 in the figure. Only a difference of 0.7 dB is observed, which confirms the good

symmetry between the RF port and LO port of this SIW mixer.

The complete measurement results, with the mixer LO port power level swept from

0 dBm to 14 dBm, with the mixer RF port power level swept from -6 dBm to 8 dBm, are

plotted in Figure 4-14.
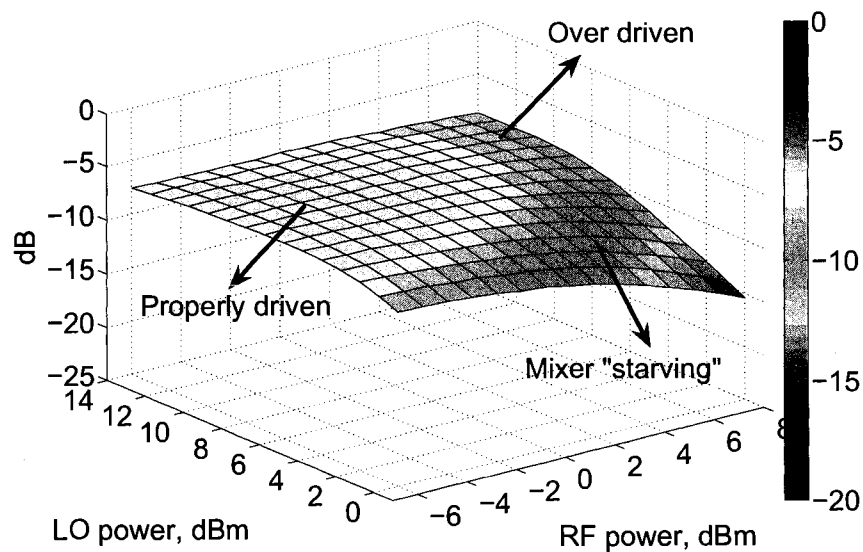
Figure 4- 14. Measured SIW mixer frequency conversion gain.
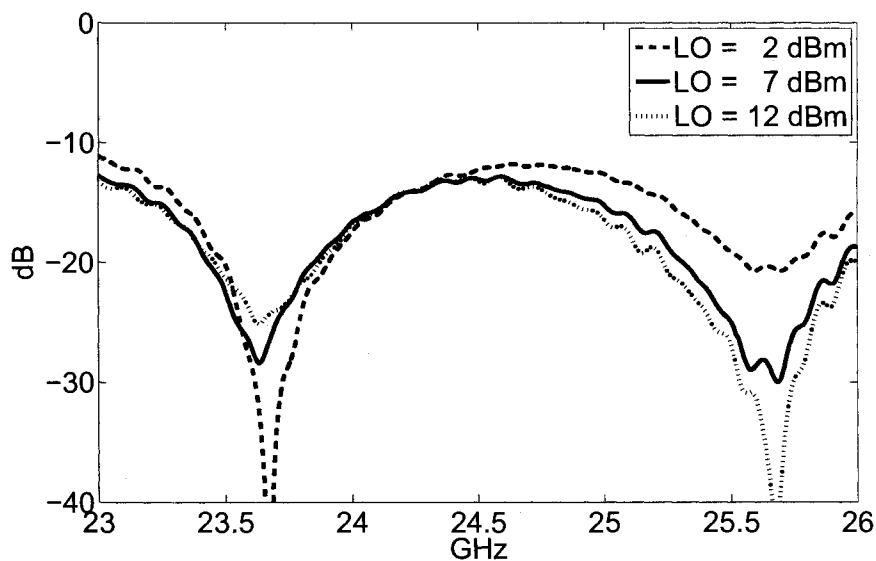
Figure 4- 15. Measured SIW mixer RF port reflection.
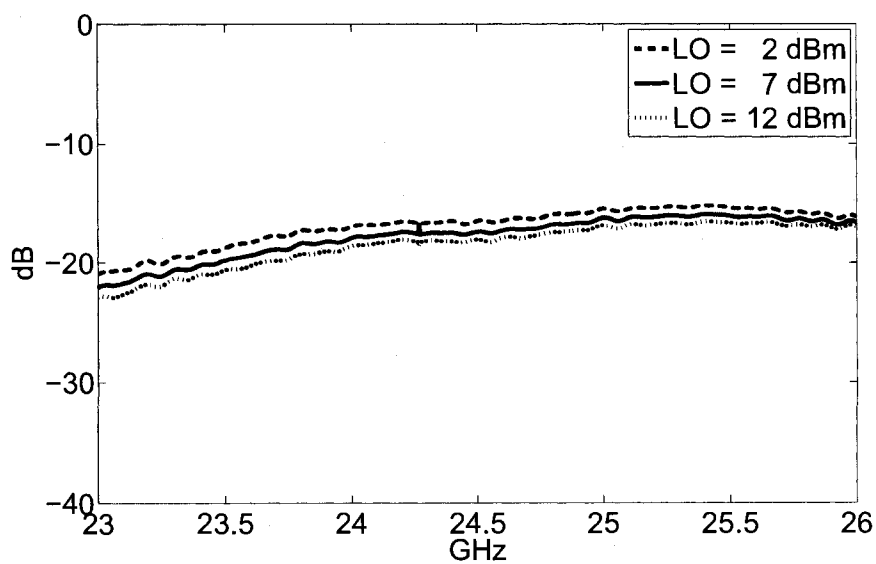
Figure 4- 16. Measured SIW mixer RF-IF port isolation.

The measured SIW mixer RF port reflection and RF-IF port isolation are shown in Figure 4-15 and Figure 4-16. Because all the mixer port impedances are related to the LO power level as a result of differences in diodes impedances, the mixer RF port

reflection as well as the RF-IF port isolation are also observed as a function of different

LO power levels of 2, 7 and 12 dBm, respectively. At ISM band (24.00 GHz to 24.25

GHz), the SIW mixer shows S_{11} below -13.0 dB at the RF port and the RF-IF isolation

of the SIW mixer is better than 17.3 dB over the ISM band of interest.
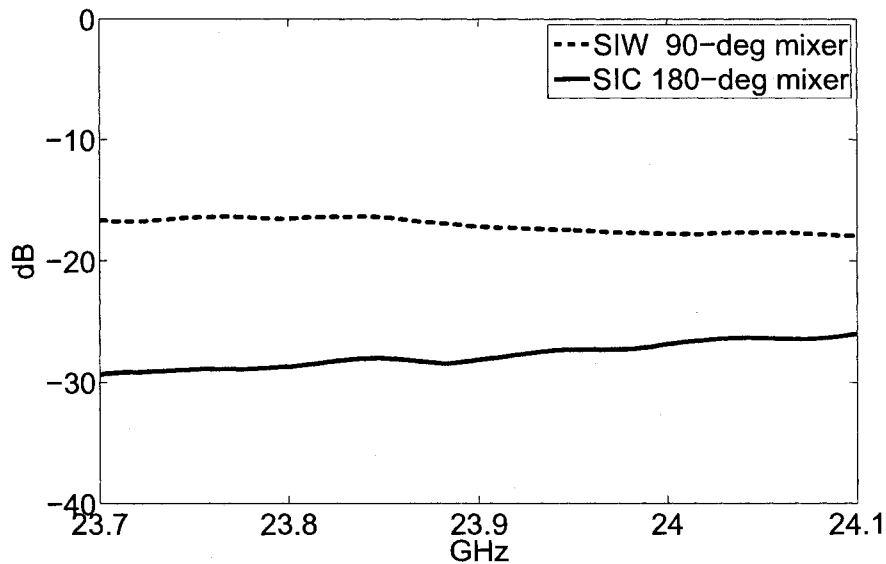
Figure 4- 17. Measured mixer LO-RF port isolation.

The measured LO-RF isolation is shown in Figure 4-17. The LO-RF isolation is

around 18 dB. This is within expected range but not an excellent one. It is the price paid

by choosing a 90-deg mixer in exchange of its convenient circuitry layout, since a 90-

deg mixer normally exhibits a poor LO-RF isolation [52]. The effect of this limited

isolation for the radar system will be discussed later in chapter 5. The conclusion drawn

there is that this leakage does not significantly degrade radar receiver dynamic range.

The mixer 3rd-order input intercept point level is measured with two RF tones spaced 10 MHz apart and 0 dBm power level with LO bias 7.0 dBm. At 24.125 GHz, a 14.6-dBm IIP3 is achieved for the SIW mixer.

4.2 SIC Mixer -A Surface-Volume Integration Approach

The above mentioned 90-deg SIW mixer demonstrates many advantages over conventional microstrip 90-deg branch line mixers [58]. However, as a 90-deg single balanced mixer, there are also some limitations on its application such as limited LO-RF port isolation and limited spurious response rejection and so on. A 180-deg single balanced mixer, on the other hand, is able to remove these limitations [52].

The frequently encountered microstrip hybrid ring seems a possible candidate for this application. However, at 24 GHz, microstrip lines suffer from high transmission losses as well as radiation loss. A complete SIW H-plane ring definitely will reduce the transmission losses as well as enlarge the operating bandwidth. Nevertheless, if an SIW H-plane ring was to be used for power coupling, then the integration with diodes would be awkward because the SIW section needs to be transformed into microstrip again. Also, the SIW technology will occupy a larger substrate area compared with microstrip technology at the same frequency band. Therefore it comes out naturally to combine the integration merits of both microstrip and SIW. An SIC mixer is designed in this work as an up-converter. The innovation in this part of the work is the combination of synthesized SIW and classic microstrip lines. A schematic view of the completed SIC

mixer is shown in Figure 4-18. The design is a hybrid platform of SIW and conventional microstrip technologies. RF port and LO port are designed using SIW technology. A microstrip ring is embedded functioning as a balun to excite LO currents and RF currents on the diodes with/without 180° phase difference. Between the ring and SIW there is a SIW-microstrip transition. The integration with beam-lead diodes is very convenient with the adoption of microstrip ring in the mixer because of their planar profile.
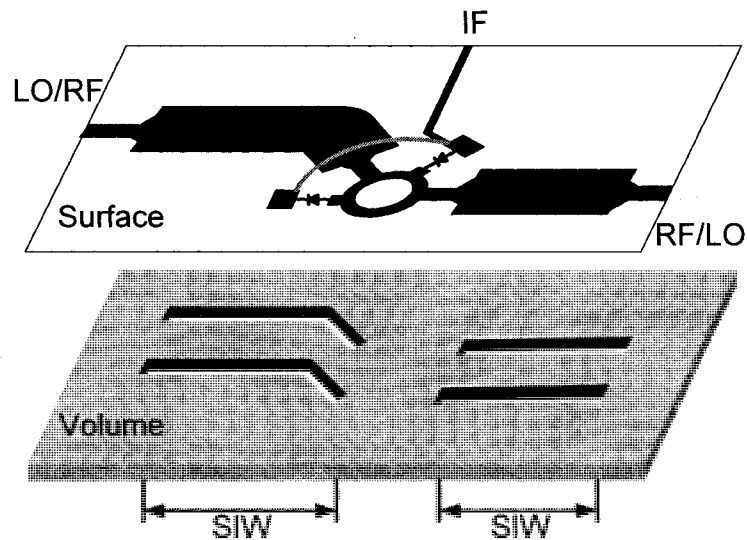
Figure 4- 18. 3-D schematic view of a 180-degree SIC mixer. (Not drawn to scale).

The ring is designed using a commercial 2-D planar method-of-moments based software, i.e. Agilent Momentum. The designed sum port (Σ) and difference port (Δ) S-parameters performances are shown in the figures below.
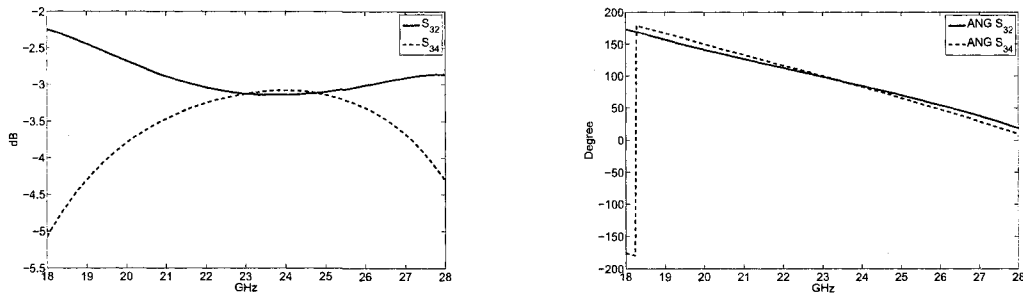
Figure 4- 19. Simulation results of microstrip ring, magnitude and angle, Σ port.
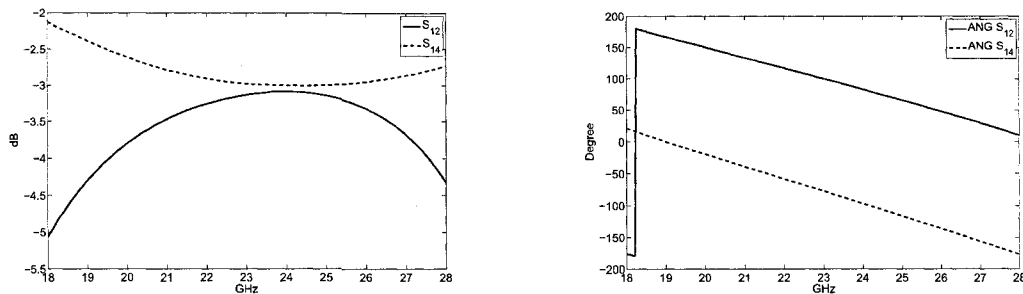
Figure 4- 20. Simulation results of microstrip ring, magnitude and angle, Δ port

The RF and LO SIW feeding section is characterized using a full wave software package, i.e. Ansoft HFSS.

The mixer conversion gain is measured in a similar manner as the SIW mixer. Power level calibration is performed with an accuracy of 0.1 dB. Measured conversion gain results are shown in Figure 4-21. The best conversion gain of -6.9 dB is achieved with a LO driven level of 7.0 dBm. It is clearly demonstrated that the pattern of the conversion gain changes as a function of input power level, which is similar to the SIW mixer. Meanwhile, the mixer balance characteristic is also shown. The smoothness of the measured data is because only power level is involved in the measurement. The frequency conversion gain as a function of the port power level across a wide power

range is measured. The measurement results are plotted in Figure 4-22. Again, gain

variance as a function of the port power level similar to the previously mentioned SIW

mixer is observed. In fact, Figure 4-21 is a cross-cut of Figure 4-22.
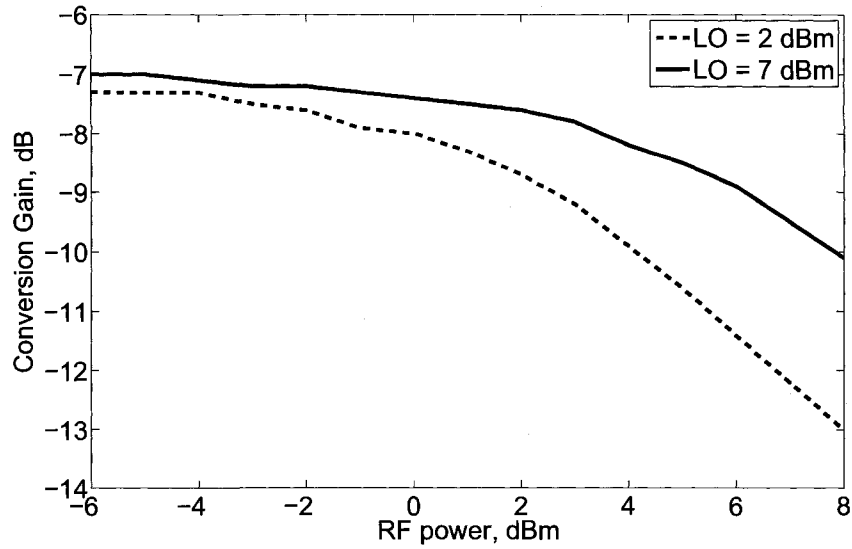
Figure 4- 21. Measured SIC mixer frequency conversion gain.
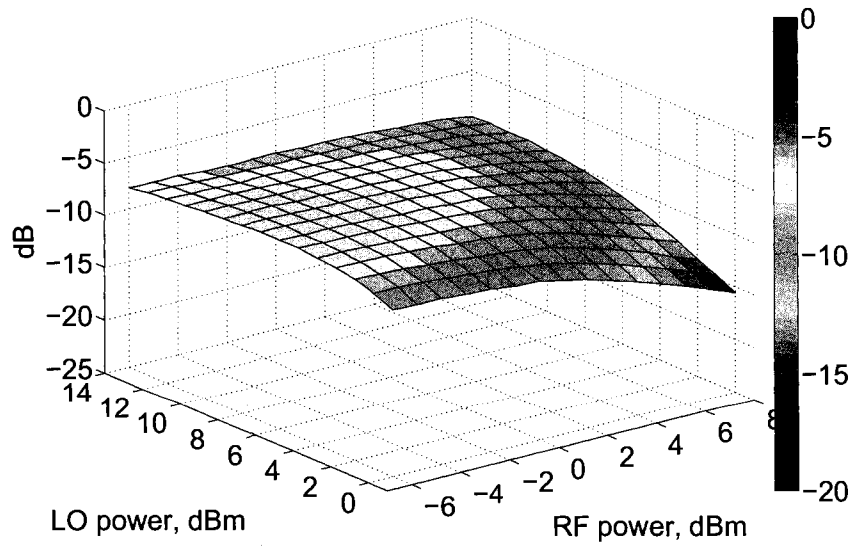
Figure 4- 22. Measured SIC mixer frequency conversion gain.

The measured mixer RF port reflection and RF-IF port isolations are shown in the following figures. The SIC mixer RF port reflection S11 magnitude is shown below -14.5 dB when mixers are driven with the LO level of 7 dBm. RF-IF isolation for the SIC mixer is more than 20.0 dB with 7 dBm LO driven level, as shown in Figure 4-24.
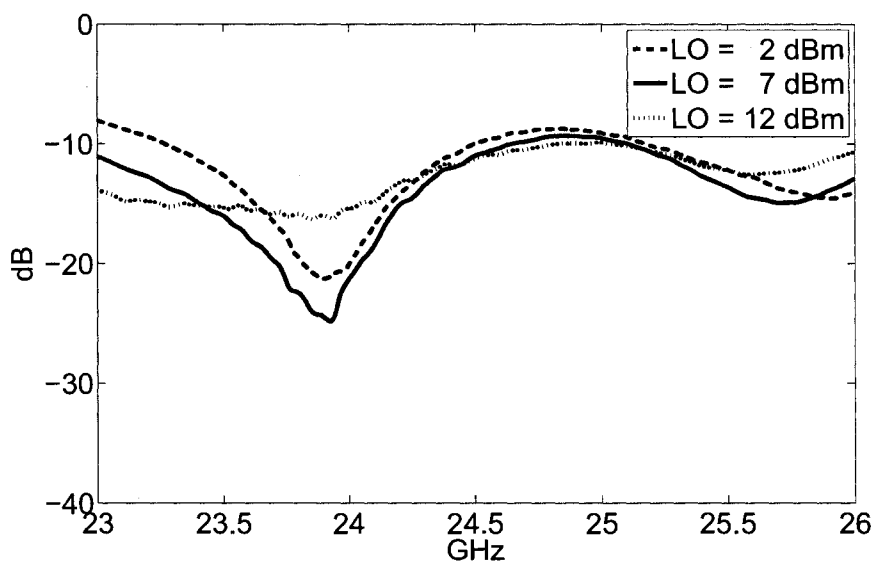
Figure 4- 23. Measured SIC mixer RF port reflection with different LO driven levels.
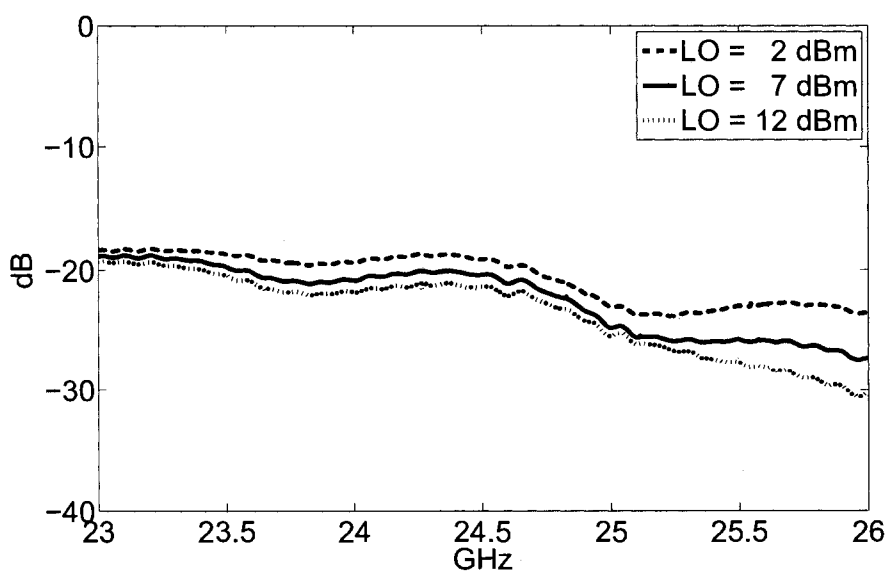
Figure 4- 24. Measured SIC mixer RF-IF port isolation.

The measured LO to RF port isolation as in Figure 4-17 shows a good isolation around 30 dB. This is because of a good symmetry of the mixer circuit topology, which is also confirmed by the symmetrical simulation results in Figure 4-19 and 4-20. The mixer 3rd-order input intercept point level is measured with two RF tones spaced 10 MHz apart with 0 dBm input power level. Mixer is biased with LO=7 dBm. Around 10.5 dBm IIP3 is achieved for this mixer.

4.3 Performances Comparison between Hybrid Integration Approach and Monotonous Approach

The above mentioned SIC mixer integrates two different waveguiding structures on a substrate, i.e. conventional microstrip lines and substrate integrated waveguides. From the fabrication perspective of MICs, the making of conventional planar transmission line, such as microstrip, involves only the surface of a substrate ("simple printing or surface etching techniques"); therefore microstrip circuitry may be viewed as "surface circuits". The fabrication process of synthesized planar waveguides, such as SIW, involves the volume etching or processing of a substrate. Thus, SIW circuitry may be better viewed as "volume circuits" [11]. Encompassing the advantages of simplicity of integration with semiconductor devices such as diodes for conventional planar transmission lines, while exploiting the merits of high-Q, well-confining EM waves for synthesized waveguides, this "surface-volume" integration scenario optimizes and maximizes the usage of the substrate electrically and materially. For example, the "surface-volume" SIC mixer is

expected to have a higher frequency conversion gain compared with geometrically similar microstrip mixer. This is because the complete enclosure of SIW will confine EM waves well within the substrate and therefore reduce the unavoidable radiation and transmission losses typical of microstrip lines at high frequencies. A geometrically resembling microstrip 180-degree ring mixer is fabricated as shown in Figure 4-25 to compare the performances with the SIC mixer.
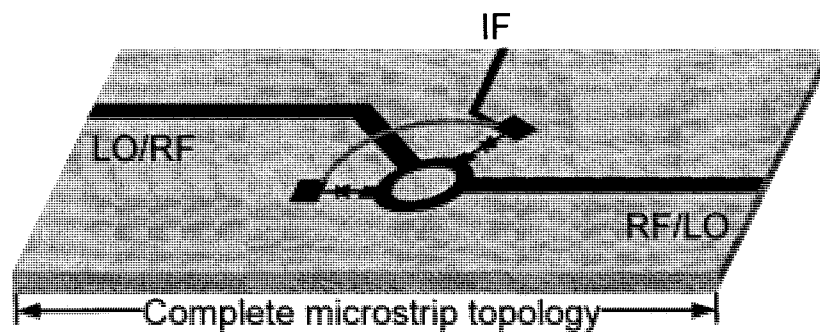
Figure 4- 25. 3-D schematic view of a 180-degree microstrip mixer. (Not drawn to scale).

One of the most important mixer specifications, namely, the frequency conversion gain of the microstrip mixer is carefully measured to make a comparison. Spectrum analyzer is used firstly to measure the frequency conversion gain with fixed RF frequency as well as fixed LO frequency. The measurement results are shown in Figure 4-26. The mixer is measured in a same manner as the SIC mixer. It is apparent that the microstrip mixer exhibits more losses compared with its SIC counterpart. In order to make the comparison more objective, careful measurements were done across 23 GHz to 25 GHz as shown in Figure 4-27. The measured results of the three mixers are compared

together. The conclusion is clear that both the SIW mixer and the SIC mixer demonstrates higher frequency conversion gain compared with the microstrip one. Around 3 dB improvement has been achieved by adopting the integrated waveguide technology. The SIW mixer and the SIC mixer has similar performance until 24.3 GHz. Then the complete SIW mixer possesses a better conversion gain in contrast with the SIC one. This could be the effect of the microstrip ring used in the SIC mixer, which is not as wide band as the SIW quadrature coupler. As frequency increases, the LO power distributes unevenly on the two mixing diodes and lead to lower conversion efficiency. Also, the adoption of microstrip lines at 24 GHz could be another reason for higher losses.
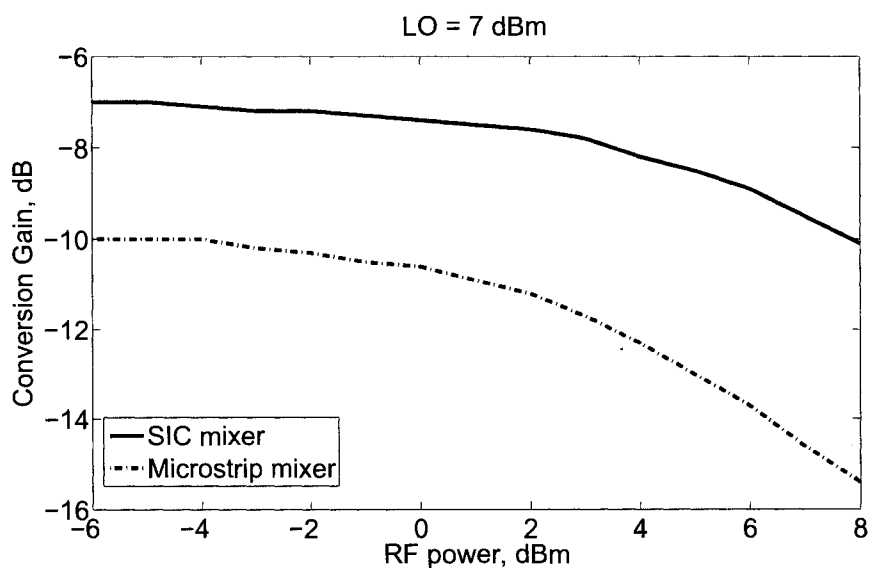
Figure 4- 26. Measured SIC and microstrip mixer frequency conversion gain with fixed RF frequency and fixed LO frequency.
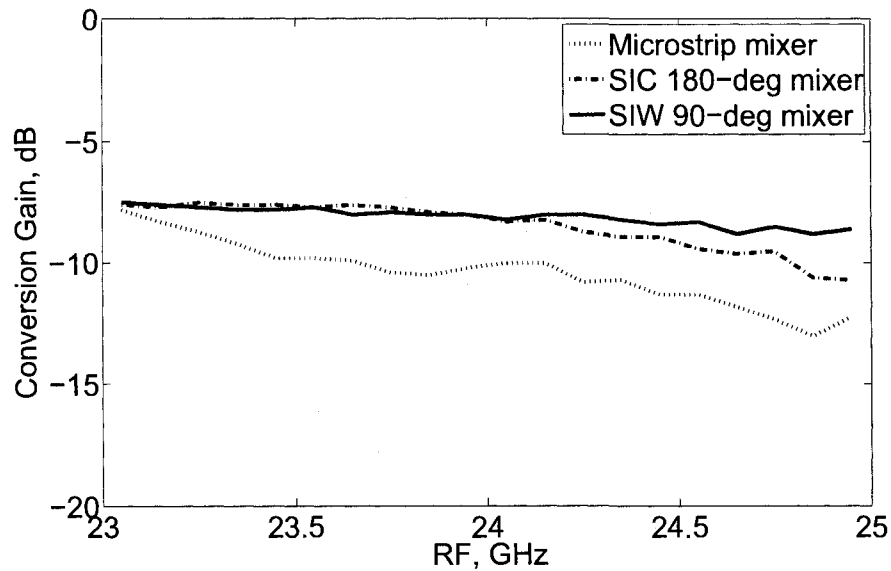
Figure 4- 27. Different mixers frequency conversion gains comparison.

As a final note of this section, all the measurement results point to one fact, this *surface-volume* integration strategy indeed demonstrates better electrical performances than conventional planar strategy under this circumstance. Meanwhile, the microstrip ring used in the SIC mixer has a smaller size (164 mm^2) compared with the designed SIW quadrature coupler (270 mm^2). It is clear that the proposed hybrid approach effectively combines the complementary advantages of each individual building block while eliminating (partly at least if not completely) inherent drawbacks and results in a fully integrated fabrication process and a very compact overall system profile. The microwave integrated circuit design is not (and should not be) limited to a monotonous guiding wave structure. The concept of SIC broadens the versatility of integration and offers a unique bridge between different integration technology to maximize the integration density as well as optimize circuit performance.

4.4 Mixer Measurement Using Network Analyzer

Among many specifications in terms of the performances of a mixer, many quantities can be measured either by a spectrum analyzer or a network analyzer. The spectrum analyzer can provide very high precision measurements up to 0.1 dB and distinct frequency discrepancy. This approach is widely adopted in a spectrum-rich measurement such as the power level related mixer performances including mixer frequency conversion gain, input port power saturation level (P1dB), inter-modulation distortion level and so on. However, this method would be extremely time-consuming when frequency conversion gain values are desired over a band of frequencies, unless extra automation programming is provided. The vector network analyzer method, on the other hand, can provide fast measurements over a band of frequencies, at the expense of more complicated calibration techniques and post data processing. It is suited to quantify frequency related mixer performances including port isolation and reflection. Although a three-port network analyzer would be useful for measuring power level related quantities including mixer frequency conversion gain [59], a two port network analyzer can also be used to measure mixer frequency conversion gain when proper calibration techniques are provided [60, 61].

Power transfer and reflection type quantities without frequency conversion, such as isolation and port reflection, can be measured using a network analyzer. For example, in the case of measurements of RF-IF isolation, it is performed with RF port connected to network analyzer port 1 and IF port connected to network analyzer port 2. The S11 obtained in the measurements is interpreted as RF port reflection. Note that the

definition of isolation is defined as the ratio between power levels of the same signal at another port to the power levels at its originated port. The RF-IF isolation is interpreted as the ratio of RF signal level at the IF port, to the RF signal level at the RF port. Therefore, the measured S21 magnitude after a standard S parameter calibration is interpreted as the isolation quantity. That is why in sections before these two measured quantities appeared in association. It is important to notice that a mixer should exhibit different isolation and reflection quantities as a result of different mixer LO driven level. This is completed by incorporating another external source in the measurement as an LO source.

The measurement of mixer LO-RF isolation is more difficult, because network analyzers generally cannot provide enough high-frequency power output to adequately bias the LO port. The maximum output power level of Anritsu 37××× is around -4.0 dBm. Therefore extra amplification of the network analyzer output power should be provided. To amplify the network analyzer output power level, an extra low noise amplifier is inserted in the network analyzer port 1 branch so that the mixer can be properly driven. The obtained output power level at port 1 is 6.2 dBm (with the default network analyzer output power of -7.0 dBm plus the amplifier gain and the interior port 1 branch insertion losses and exterior cable losses). With this output power level, it is sufficient to drive the mixer under proper working condition.

A network analyzer can also be used to measure mixer frequency conversion gain, when proper configuration is provided. The principle of this measurement is easy to understand, when the mechanism of S parameters measurements is understood. At either

port of the network analyzer, a pair of transmitter and receiver is configured to measure the power ratio of the transmitted signal as well as the reflected signal. The measurement of conversion loss therefore is possible if only absolute power levels are measured instead of power ratios. This is equivalent to say that the network analyzer is the same as a spectrum analyzer when it only measures the received power level. Of course, a proper power level calibration should be performed in order to make power level measurement interpretable.

CHAPTER 5 INTEGRATION OF SYSTEM-ON-SUBSTRATE AND SYSTEM EXPERIMENTS

Before different SIW and SIC components and devices can be integrated together on a substrate, some integration issues unique to an integrated system-on-substrate should be carefully considered, for example, the proper selection of the transmitter up-converter and the receiver down-converter, the leakage effects on the system performance and so on [32, 62-65]. The fabrication process of the prototype is explained in this chapter. Upon the completion of the prototype, the functionality of the front-end is confirmed using a single tone test experiment. Radar range measurement is performed afterwards by using a VCO to generate a linear frequency modulated signal. Detailed discussion on radar range responses and the measured results are given in this chapter. Finally, the possibility of sharing the FMCW radar front-end with spread-spectrum radar is discussed.

5.1 Selection of Mixer

When it comes to justify the selection of different mixer in the transmitter and receiver, the electrical performances as well as the integration issues of the mixers should be balanced [33]. An advantage of a 90-deg mixer is that its LO port and RF port are placed on the same side of the mixer, which is a very gracious point in the design of a compact integrated system due to this layout convenience. As it will be discussed later

in this chapter, this orientation of mixer LO port and RF port also enables the radar antennas to be placed in a way that permits high free space isolation between antennas. Parametric studies on chapter 4 suggest that the isolation of SIW coupler used in this mixer obtains its maximum isolation when the two ports are excited in the same frequency band. Meanwhile, since the homodyne FMCW radar receiver is a zero-IF architecture, the receiver LO signal and the received RF signal are in the same frequency band. Therefore it is concluded that the FMCW radar receiver could be an appropriate application situation for a 90-deg SIW mixer. On the selection of transmitter mixer, a 180-deg mixer can accommodate a much larger frequency difference between the LO signal and RF signal. This enables the separation of the USB signal from LO signal and LSB signal to be performed easily. Meanwhile, a 180-deg mixer generally exhibits better LO-RF isolation performances as observed from the measurement results in chapter 4, which is effective in reducing the transmitter leakage. Another benefit of choosing the SIC mixer is that it occupies a relatively small size in contrast with the SIW mixer in the transmitter, where devices including SIW power divider, transmitter drive amplifier, power amplifier and receiver LO driver are concentrated together. Care must be taken in considering the placement of the 180-deg SIC mixer LO port and RF port, because they are placed on different sides of the IF signal. In this work, because the transmitter LO signal comes from an external source, therefore the 180-deg SIC mixer can be placed conveniently with the RF port interconnected to the SIW power divider, while the LO port and IF port can be oriented normal to each other on both sides of the system.

5.2 Leakage and LO Interference

As a member of CW radar family, FMCW radar also faces the challenge of leakage phenomenon between the transmitter and receiver which is inherent to any CW radar. This leakage could cause severe problems for the FMCW radar receiver by saturating the receiver first-stage low-noise-amplifier or degrading radar performances by reducing the dynamic range, depending on the leakage power level and the leakage place. This is why most FMCW radars are limited to short range applications, where high transmitter power is not required and leakage power level is low [23, 62, 64, 66]. For a radar system with one antenna, the majority of the leakage comes from the insufficient isolation between the circulator ports connecting transmitter and receiver, in which 25-dB isolation is typical. For a radar system with two antennas, the majority of the leakage comes from the free space coupling between the transmitter antenna and the receiver antenna, in which up to 60 dB isolation can be achieved. FMCW radars employing two separate antennas are mostly used to overcome the challenge of designing a high isolation circulator. In the integrated system-on-substrate, because of the size restraint on the front-end, the two SIW slot array antennas are spaced very close, which might result in insufficient free space isolation and degraded receiver performances, as shown in figure below.
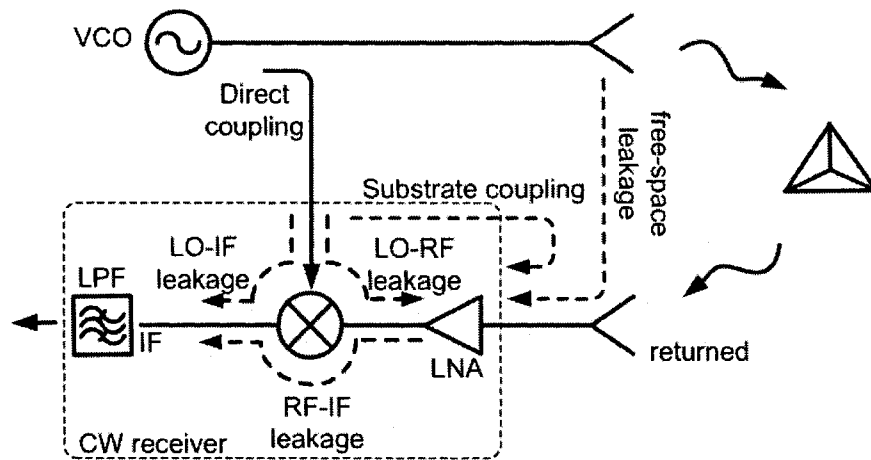
Figure 5-1. A generic FMCW radar model with illustrated leakage paths.

In order to investigate the effect of leakage on the receiver performances, accurate leakage modeling and measurements of its effect on the receiver dynamic range is of great importance. Upon a constructed generic FMCW radar homodyne receiver model employing such an antenna system, the free space leakage and its effect on the FMCW radar receiver performances are investigated in this work.

Considering the generic FMCW radar model as shown in Figure 5-1, the basic ranging principle of FMCW radar is to measure a frequency shift caused by the time delay of a reflected signal, when the transmitted signal is linearly-frequency-modulated by a periodic waveform. Because of its auto-correlation ranging method, FMCW radar receiver requires a reference signal directly coupled from the transmitter mixing with the received signal. Therefore, the FMCW radar homodyne receiver is mathematically equivalent to a frequency difference measuring device for the reference channel and the received signal channel. Successful detection of the target range depends on sufficient detection of this frequency difference signal between the two channels [62].

Upon this, an experiment to measure the effects of leakage on the homodyne receiver

is designed as shown in Figure 5-2.
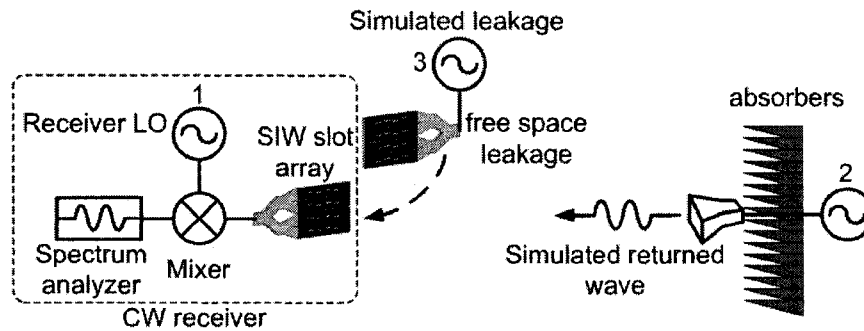
Figure 5-2. Free space antenna leakage measurement setup.

Figure 5-3. Photograph of the measurement setup (the second source which
functions as a simulated target return signal is not shown).

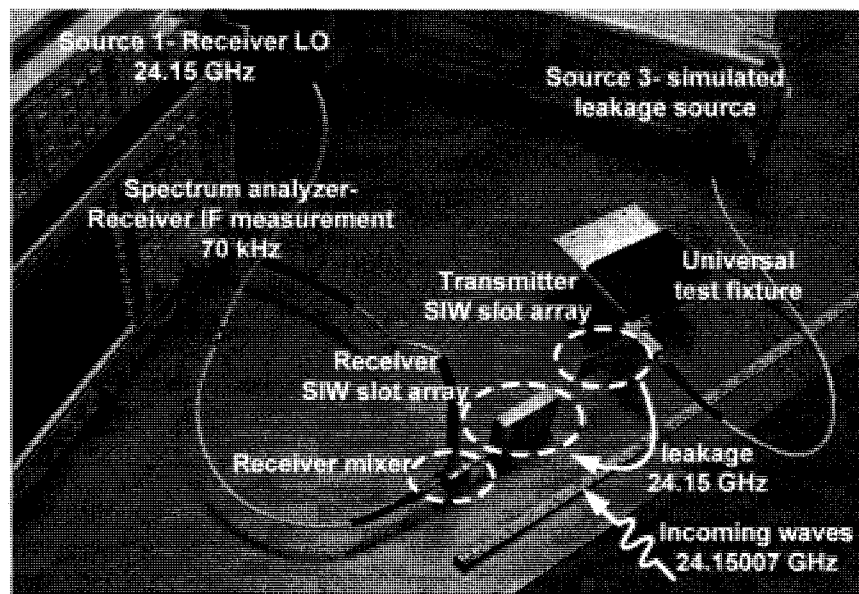The receiver is constructed with an SIW slot array antenna connected to a mixer RF

port. The SIW antenna is mounted on a copper base to facilitate the connection with the

mixer module. The LO of the receiver is provided with an external signal source. The

function of this source is equivalent to the reference signal in the generic model. A second source is placed far away from the receiver, which emits a signal through a horn antenna illuminating the receiver with a frequency different from the receiver LO. Bear in mind that for an FMCW radar with linear-frequency-modulation, the target range is a linear function of the frequency difference between the reference and the reflected signals [67]. Therefore, this source is equivalent to a reflected signal from a target with a frequency shift different from the reference signal. A third source is connected to another SIW slot array, with a frequency identical to the receiver LO. This source is the simulated source of transmitter leakage. The antenna is clamped by a universal test fixture and is placed in a way similar to the placement of the two antennas on the system-on-substrate layout [31]. It is worth mentioning that in order to approach a more realistic system, the leakage signal should be coherent to the reference signal, that is to say that the leakage signal should be applied to the transmitter SIW antenna from the receiver LO either through a power divider, or through a directional coupler. However, this approach will lose the control over the absolute leakage power level on the receiver antenna, limiting the measurement system. Moreover, for an FMCW radar system when only frequency difference information (i.e., target range) is of interest, losing leakage-reference phase coherency will not affect the system ability to measure the frequency difference. Notice here that the definition of leakage refers only to the free space leakage between the two antennas. The feed-through of the direct coupling signal, either caused by the limited receiver mixer LO-RF isolation or the imperfect receiver antenna port matching condition, is not singled out. However, because the variables of this

experiment are the power levels of the simulated leakage source and the simulated returned wave, both are external to the radar receiver, therefore the observed receiver detection ability changing is due to the free-space leakage only.

The radar receiver LO frequency is set at 24.15 GHz. The simulated target return wave source is set with a frequency value of 24.15007 GHz. The power level is set at the radar receiver antenna port where the incoming wave is -84.6 dBm. Based on the radar equation [23], $P_r = P_t \cdot G^2 \cdot \lambda^2 \cdot \sigma /[(4\pi)^3 \cdot R^4]$, for a CW system with a 0-dBm transmitter power level, this is equivalent to a target with 260 m^2 radar-cross-section (RCS) 50 m away.

Because single tone signal is used in the experiment, the minimum detectable signal level (*MDSL*) is an appropriate description of the receiver sensitivity. With the spectrum analyzer (Rohde & Schwarz FSIQ40) measurement bandwidth of 20 kHz, the noise floor is around -110 dBm. Consider a signal-to-noise (SNR) ratio of 15-dB, the MDSL is around -95 dBm. However, with the presence of leakage signal, either the receiver sensitivity or the SNR will be degraded. The leakage signal power level on the receiver antenna is controlled by changing the third source power level. With a measured leakage level of -36.0-dBm, the measured receiver MDS versus a measured receiver MDS without leakage is shown in Figure 5-4.
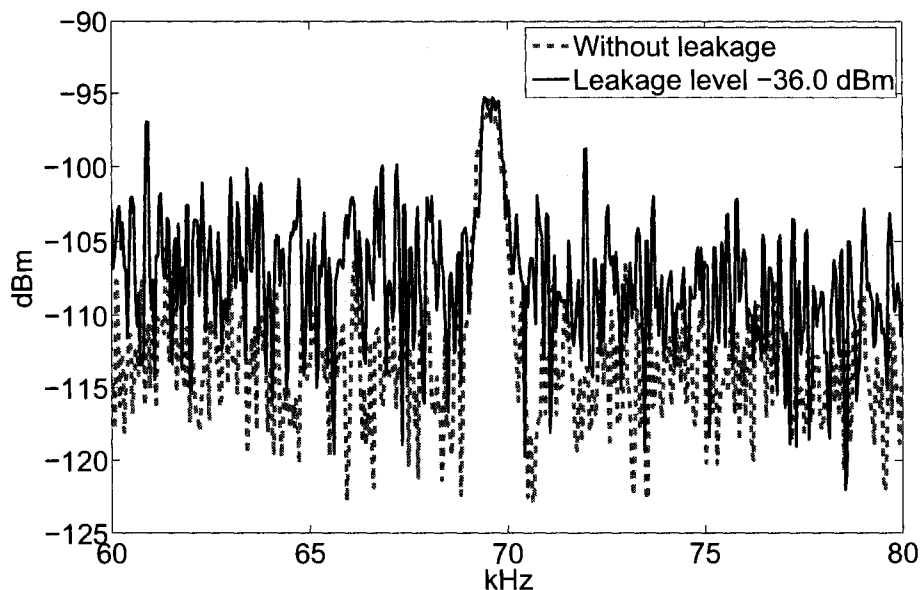
Figure 5-4. The minimum detectable signal level without the presence of leakage and the degraded signal with the presence of leakage.

It is clearly demonstrated that even with a small leakage level, the noise floor of the receiver is still increased to -105 dBm. With the incoming waves unchanged, the receiver SNR is decreased to 10 dB. The physical reason of this is the presence of an unwanted DC component generated because of the mixing of receiver LO and the leakage signals. Once the DC component is generated, it will flow within the nonlinear mixing junction and increase the flicker noise, therefore increasing the overall mixer noise level. It is important to notice that although some techniques exist to cancel this leakage signal [68-70], they are however generally complicated and expensive for low-cost sensor applications.

To recover the IF signal, either the "useful" input RF signal level has to be increased, or the IF signal-to-noise ratio should be sacrificed. This implies that either the radar

cannot "see" as far as in a no leakage situation when a -36.0-dBm leakage is presented, or the radar probability of detection has to be reduced due to the reduced SNR. In most radar applications, the SNR is specified from a given false-alarm probability and normally cannot be compromised, which suggests that the maximum range performances have to be compromised to maintain a given SNR. Experiment results as shown in Figure 5-5 reveal that only when the input RF signal level is increased to a -74.5-dBm would the IF signal be recovered for a 15-dB signal-to-noise ratio. Obviously, the augmentation of input RF signal levels to maintain the signal-to-noise ratio is equivalent to a loss of receiver sensitivity. Based on radar equation, the reduced maximum radar operating range can be estimated.
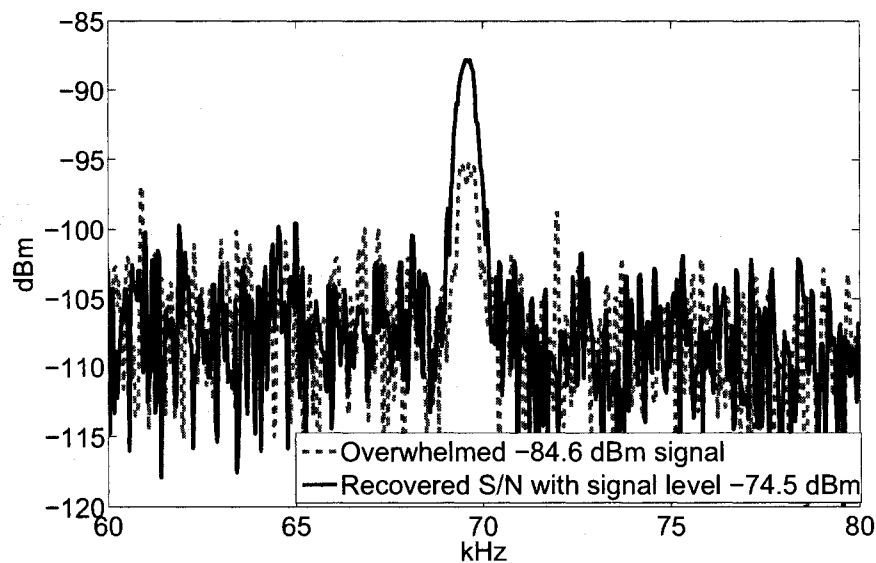
Figure 5-5. The degraded original signal and the recovered signal (with the penalty of 10.1 dB dynamic range sacrifice).

93

Meanwhile, the DC component caused by the leakage will also influence the upper

end of the dynamic range by affecting the compression point, i.e. $P1\mathrm{dB}$ point, as

illustrated in the figure below.
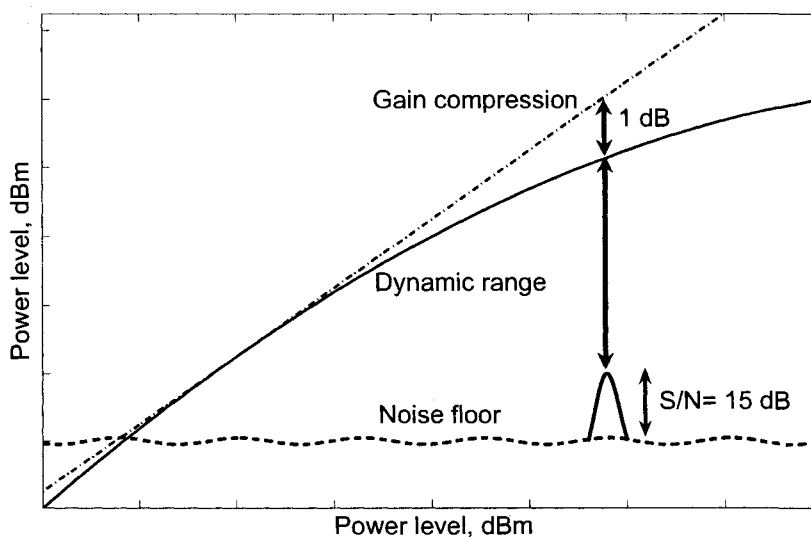
Figure 5-6. 1-dB dynamic range measurement definition (not drawn to scale).

A circuit-level model is constructed using the Advanced Design System (ADS)

simulation package to investigate this effect. The simulated mixer frequency conversion

gain, as a function of different leakage levels is shown in Figure 5-7.
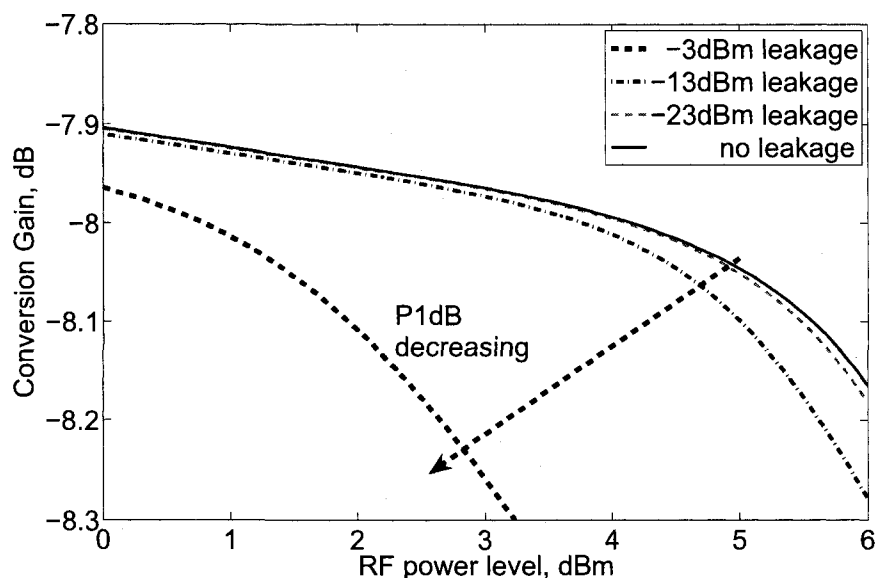
Figure 5-7. Simulated conversion gain compression point decreasing with different leakage levels.

Clearly, the $P1$dB gain compression points demonstrate a trend to decrease as the leakage level increases. This is also because of the unwanted DC component offsets the mixer diodes operation point. Therefore, at the upper end of the receiver dynamic range, the leakage signal will make the receiver more likely to be saturated. However, it is found that the effect of leakage on the gain compression point decreasing is minuscule. Even when the leakage level is increased to -3-dBm, the $P1$dB point shows less than a 0.5-dB decrease. The physical explanation for this is that the diodes biasing point shifting caused by the generated DC component, is a small quantity compared with the diodes biasing currents provided by the LO driven signal.

To experiment this effect, let us consider the "self-mixing" effect caused by mixing a signal possessing the same frequency as the LO, the free-space leakage measurement

experiment can be simplified by using a mixer model with a power-combing network.

The experiment is set up as shown in the following figure.
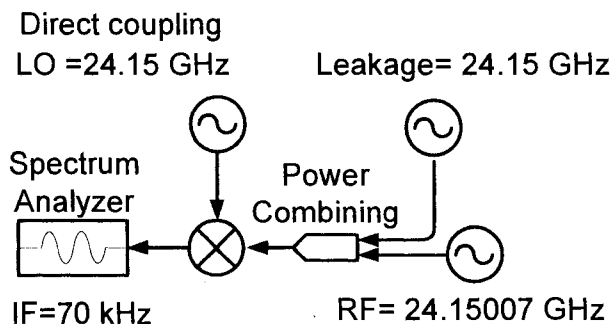
Figure 5-8. Measurement setup for modeling dynamic range with leakage effect
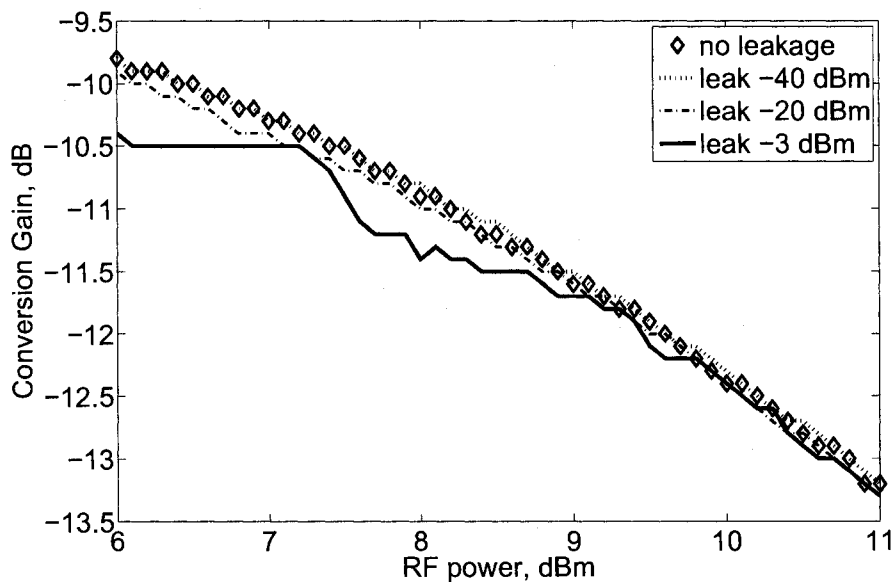
Figure 5-9. Measured conversion gain compression with different leakage levels.

The measurement turns out to be difficult since when the leakage level increases, the

generated DC component also increases. Because the mixer is directly coupled to the

input port of the spectrum analyzer, this DC component overflows the spectrum analyzer

input mixer and introduces fluctuation on the converted IF signal. It is found that the

power saturation performances are indeed influenced much less even if a significant level of leakage occurs. Less than 1 dB $P1dB$ drop down is recorded with the presence of a -3 dBm leakage. Therefore it is safe to conclude that a leakage in the level of -40 dBm will almost have no effects on the upper end of the dynamic range.

Besides the free space leakage introduced from the receiver antenna, there are other sources of leakage affecting the receiver performances. Among these leakages, those that are caused by the receiver LO is of most interest, because the LO signal normally has a high power level within the receiver. One possible leakage is the one from LO to the receiver low-noise-amplifier (LNA) input port, which is caused either through insufficient receiver mixer LO-RF isolation or caused by the substrate coupling. The effect of this leakage is potentially to saturate the LNA due to the high signal power level before the useful signal is amplified. The leakage as a consequence of low LO-RF isolation can be reduced either by improving mixer performances, or by placing an additional isolator between the mixer RF port and the LNA output port. The on-substrate coupling between the receiver LO and the LNA could be suppressed by embedding metalized channels within the substrate to isolate different modules. The quantitative analysis of this leakage however, should be performed based on each specific layout situation from a full-wave analysis point of view [71]. Possible insufficient RF-LO isolation, however, cannot be a severe damage to the overall performance, because the RF signal power level is relatively low. This is the same for the possible insufficient RF-IF isolation.

Another important leakage within the receiver is related to insufficient mixer LO-IF isolation. If the receiver IF processing unit has a high gain chain, the leaked LO could saturate the IF before the useful signal is amplified. Also, for a system with a fixed analog-digital converter (ADC) sampling rate, the excessive LO could easily produce aliasing phenomenon for the signal processing part, making the target beat frequency undetectable. A simulation system based on behavior model is designed to simulate this effect. Considering the receiver has an input signal level of -30 dBm with an 18-dB gain, the simulated demodulated IF beat signal for a 15-dB LO-IF isolation and the same propagation path for a 30-dB mixer LO-IF isolation are shown in Figure 5-10. Clearly, the demodulated IF beat signal for an insufficient LO-IF isolation contains extra high frequency LO component and will cause aliasing of the ADC. The signal amplitude is also significantly increased due to the excessive LO signal, which could exceed the dynamic range of the ADC. To prevent this, the mixer LO-IF isolation should be high enough or a low pass filter should be included between the ADC and receiver mixer output to sufficiently attenuate high frequency LO signals.
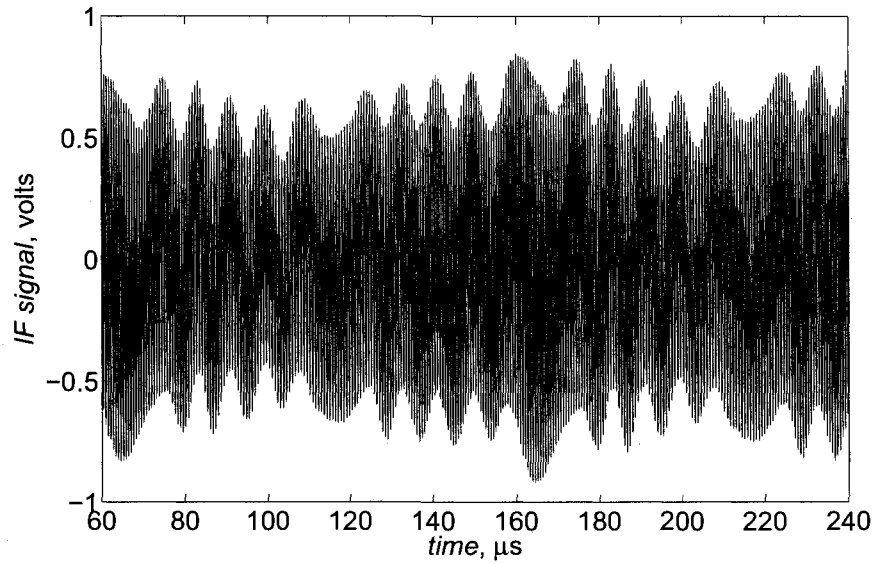
Figure 5-10. a) A simulated demodulated IF signal in a receiver system with received power level is -30 dBm and a mixer LO-IF 15 dB isolation.
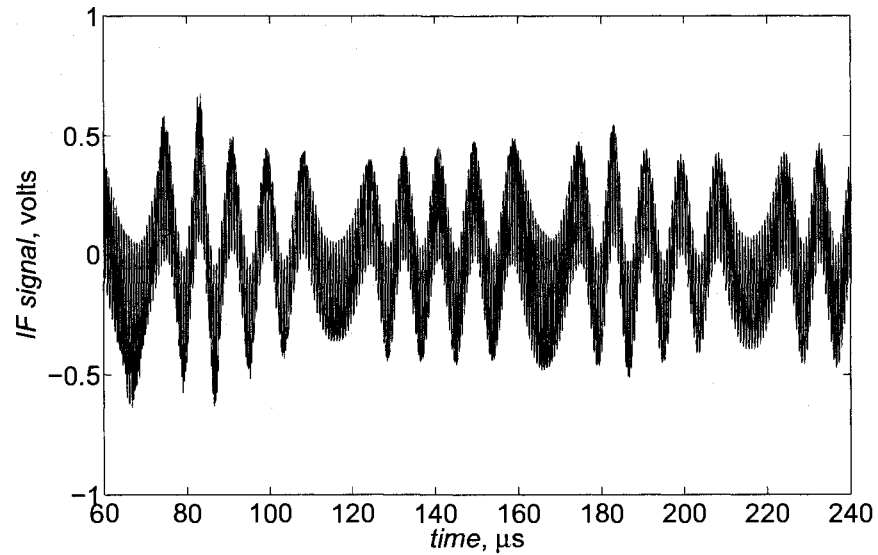

Figure 5-10. b) A simulated demodulated IF signal in a receiver system with received power level is -30 dBm and a mixer LO-IF 30 dB isolation.

5.3 Front-End Fabrication

The complete front-end system on substrate is fabricated on a dielectric material RT6002 with ε_r=2.94, and $\tan\delta$=0.0012 at 10 GHz. A copper cladding thickness of 17 μm is chosen. Although thicker copper cladding will increase the adhesion of the copper to the $(CF_4)_n$ media, it will reduce the maximum achievable photolithography resolution. Thinner copper cladding could maximize the achievable photolithography resolution; however, a very thin copper layer could peel off the dielectric media easily and reduce the entire PCB mechanical robustness. Another reason why this ε_r=2.94 material is chosen instead of a lower dielectric material such as RT 5880 with ε_r=2.22, is that compared with pure PTFE $((CF_4)_n)$ material such as RT5880, RT6002 material is a composite material. This property improves the adhesion of tin to the substrate in a chemical process, which is crucial for SIW sidewall metallization process.

The fabrication of the front-end system is described as follows. The first step requires the complete cutting contour for all the SIW components on the substrate. A Nd-Yag Q-switched laser is used in this process which generates a pulsed laser with 532 nm wavelength. After sputtering a thin metal layer on the channels, the PCB is then immerged into a $CuSO_4$ electroplating solution to metalize the side walls of the channels on the PCB. Those metallised channels are then protected with a $FeCl_3$ erosive-resistant transparent tape before photolithography. After aligning the PCB with its mask, a standard photolithograph process is performed to produce the complete layout of the system. A photograph of a front-end system-on-substrate PCB is shown in Figure 5-11. Finally, active devices are wire-bonded to the traces on the substrate, which is glued on a

metal base using a conductive silver epoxy. It is worth knowing that because the PCB layout is made out of copper, the bonding process becomes extremely difficult since fused gold adhere to copper poorly. The sacrifice paid for this is that wire bonding was used between MMIC and PCB instead of ribbon bonding, which leads to 2~3 dB extra amplifier gain loss at each stage of the system. The future development of SIW radar should avoid this disadvantage by depositing a thin layer of gold on the entire circuit.

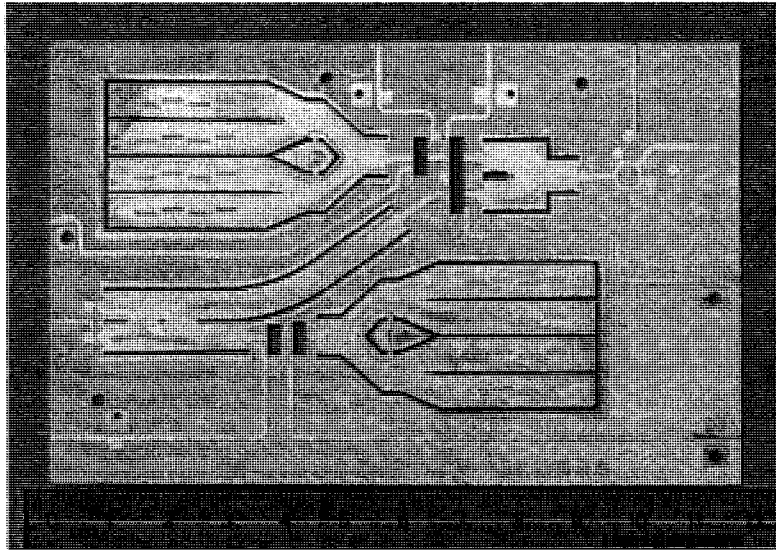Figure 5- 11. Photograph of a front-end system-on-substrate PCB (from [72]).

5.4 Radar Front-End System Experiments

a). Front-end functionality verification.

Before performing the target range measurement experiment, the functionality of the front-end should be verified. It is important to notice that the functionality of the front-end is a different concept with respect to that of radar. The radar functionality is

described by its ability to measure target range. While front-end functionality is mostly related to the frequency response of a FM system. Considering a triangular waveform modulated FMCW radar, the front-end basically functions as a frequency difference measuring device. That is to say, at any instantaneous moment, the front-end measures the frequency difference between the reference signal (the same as the transmitted signal) and the received returned signal (target reflection signal). Therefore, the frequency response of the front-end itself can be verified using a single tone experiment.

The experiment is designed as shown in the figure below. With a single tone transmitter IF signal *Tx_IF*, mixing with a single tone transmitter LO signal *Tx_LO*, a single tone transmitter signal *Tx* is generated. This transmitter signal is coupled to the receiver as a reference signal, bearing the same frequency. Meanwhile, another source transmits a signal *Rx* different to *Tx* in frequency, illuminating the front-end. The receiver is supposed to be able to receive this *Rx* signal and mix it with *Tx*, generating a IF signal *Rx_IF*, which is equivalent to measuring a target. The mathematical relationship between this measured *Rx_IF* signal and the equivalent target range, should be a linear function for a linear modulation scheme.

Figure 5- 13. Measured front-end receiver IF frequencies as a function of equivalent target range.

Tuning the simulated target source with a frequency step is equivalent to moving the target away from the front-end. For a well-designed front-end, the measured real front-end receiver IF output *Rx_IF* should be a linear function of the changed *Rx*. The recorded real receiver IF outputs as a function of the equivalent target range are plotted in the above figure. It is observed that a linear response is obtained with the fabricated front-end prototype, which confirms the functionality of the front-end.
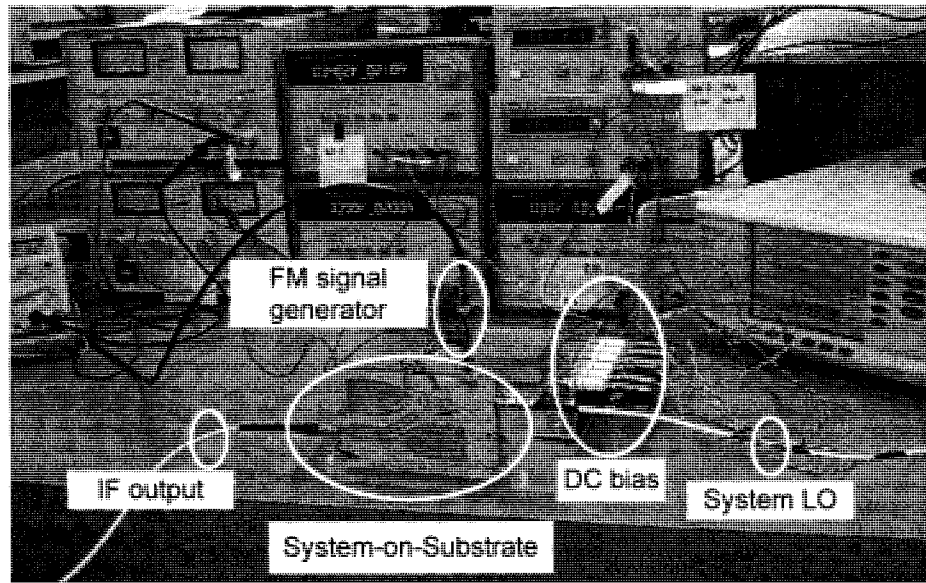
Figure 5- 14. Photograph of the FMCW radar during experiment.

b). Radar functionality verification.

To verify the functionality of the radar, a LFM signal is used as a baseband input. The radar performance with different modulation techniques can be studied with a generic approach [67]. Suppose an FM signal is in the form of

$$f' = f_0 + Mf(t) \tag{5.1}$$

where f_0 is the carrier frequency, f(t) is the modulation signal, M is modulation index. The instantaneous transmit signal phase can be obtained by

$$\varphi = 2\pi \cdot \int_{-\infty}^{t} f'(x)dx = 2\pi f_0 t + 2\pi M \int_{-\infty}^{t} f(x)dx \tag{5.2}$$

Based on the homodyne design of the system, the output of the mixer in receiver is essentially a multiplier; the output will be the vector summation of the reference signal V_0 from the transmitter and the received signal V_s with a time delay τ, i.e.

$$V = \sqrt{V_0^2 + V_s^2 + 2V_0 V_s \cos \Delta\varphi} \tag{5.3}$$

Expanding the above equation in a power series until the second order gives

$$V = V_0 + V_s \cos \Delta\varphi + \frac{1}{2}\frac{V_s^2}{V_0} - \frac{1}{2}\frac{V_s^2}{V_0}\cos^2 \Delta\varphi \tag{5.4}$$

Because the received signal amplitude is much less than the reference signal, i.e. $|V_s| \ll |V_0|$, the second order terms can be omitted and we can get the following

$$v_s \approx V - V_0 = V_s \cos \Delta\varphi \tag{5.5}$$

Note that here v_s is referred to as a time signal.

The instantaneous phase difference between the transmitted signal and the received signal can be given by the integration of frequency over time as

$$\Delta\varphi = \varphi_{reference} - \varphi_{receiving}$$
$$= 2\pi f_0 t + 2\pi M \int_{-\infty}^{t} f(x)dx - 2\pi f_0(t-\tau) - 2\pi M \int_{-\infty}^{t-\tau} f(x)dx \tag{5.6}$$
$$= 2\pi f_0 \tau + 2\pi M \int_{t-\tau}^{t} f(x)dx$$

Therefore, the instantaneous mixer output signal can be given as

$$v_s = V_s \cos[2\pi f_0 \tau + 2\pi M \int_{t-\tau}^{t} f(x)dx] \tag{5.7}$$

Integrating this signal over the modulation period gives

$$v_i = \frac{V_s}{T} \int_{-T/2}^{T/2} \cos[2\pi f_0 \tau + 2\pi M \int_{t-\tau}^{t} f(x)dx]dt \tag{5.8}$$

which is also the auto-correlation of the transmitted signal. From Wiener-Khinchine theorem, which states that the power spectral density of a wide-sense-stationary random process is the Fourier transform of the corresponding autocorrelation function, this received signal is the inverse Fourier transform of the transmitted signal power spectrum. Consequently, for a linear-frequency-modulation signal, the rectangular power spectrum will produce a demodulated signal having a sinc-function envelope distribution. As target range varies, the range gate will give responses at different frequencies accordingly as shown in Figure 5-15 below.
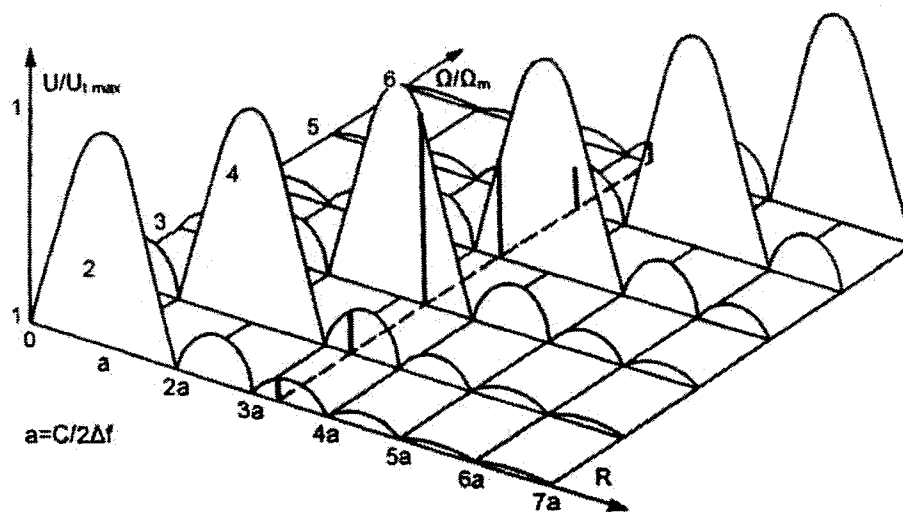
Figure 5- 15. Spectral component amplitude dependence on target range (from [24]).

To group most of the demodulated signal into a major spectrum range gate, linear-frequency-modulation (LFM) techniques including symmetrical sawtooth (triangular) waveform and asymmetrical sawtooth waveform are used in the experiment. This is the unique characteristics for LFM techniques. An external VCO with around 0 dBm output

power is used to generate the required baseband FM signal. A corner reflector with a RCS of approximately 260 m^2 is used as a station target placed away from the radar. The output radar transmitted signal is measured around 0 dBm from 23.87 GHz to 24.13 GHz as shown in Figure 5-16.
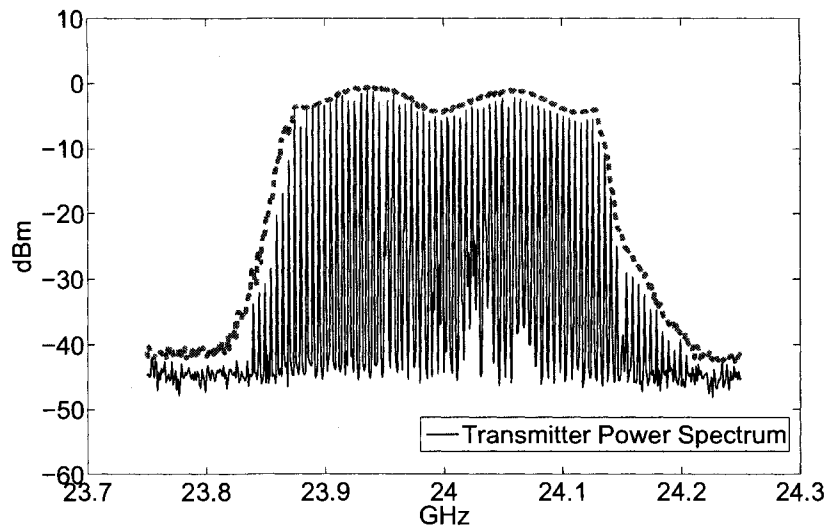
Figure 5- 16. Measured transmitted signal spectrum.
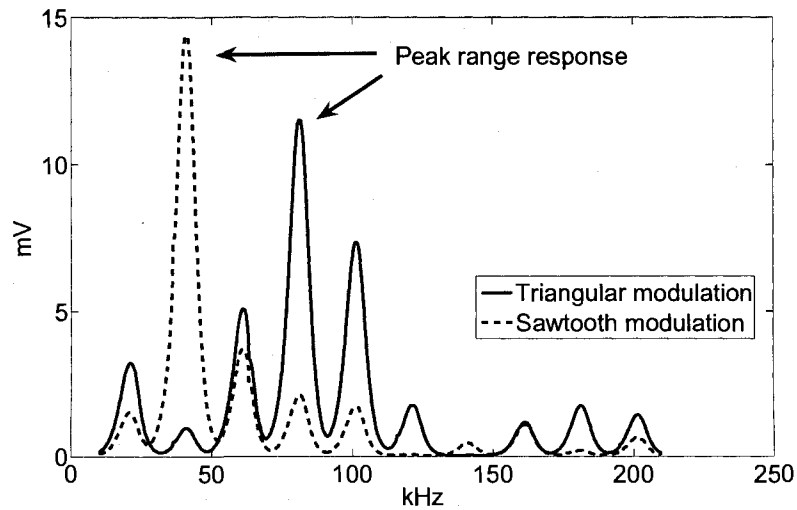
Figure 5- 17. Measured spectrum of a converted receiver IF output for a 1.00 m target with a modulation frequency of 20 kHz.

The receiver IF output is low-pass filtered before being measured using a spectrum analyzer. As an example of typical measured range responses, one converted receiver IF signal spectrum is shown in Figure 5-17. The baseband VCO is swept at a rate of 20 kHz over 7.0 V, resulting in a frequency-modulation bandwidth (for 0-dBm power level) of approximately 260 MHz and an IF frequency around 70-kHz/m distance between the antenna and the target for a triangular modulation. The measured range response includes a spectral peak around 80 kHz for the case of a triangular modulation, indicating the measured target range. For the case of a sawtooth modulation, because the tuning bandwidth is not changed while the modulation period is actually doubled, the demodulated IF output is approximately a half of the triangular modulation case. Aside the major peak component, several range side lobes are clearly visible. It is interesting to point out that there are basically two major factors contributing to this phenomenon. Firstly, it is in the nature of the FM system employing a rectangular spectrum [67] to produce such range side lobes. Because, as mentioned earlier, the range response of such an FMCW radar is the inverse Fourier transform of the transmitted power spectrum, i.e. a group of harmonics with the envelope of a sinc function.

Secondly, the spreading of the range response could also be due to the limited FM linearity. In this case, it is because of the limited VCO frequency tuning linearity. Some research works [73, 74] on increasing the FM ramp linearity clearly demonstrate the improvement on range measurement accuracy. It is concluded from [73, 74] as shown in the figure below, that reducing spread of range side lobes and achieving a high range peak will be obtained when the linearity of the FM is significantly improved.
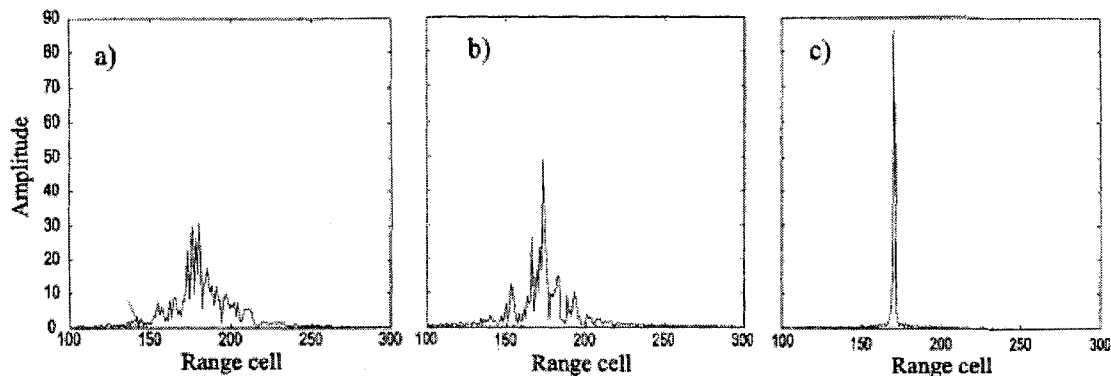
Figure 5- 18. Range profile of a delay line. a). without linearization, b).with hardware linearization, c). with hardware and software linearization. (From [73]).

The frequency value of the maximum range response is recorded to calculate the measured range. A series of range measurements can be made by moving the target with a distance step. Two types of modulation schemes are used in this work and the detailed range measurement results are plotted in the figure below. Obviously, it is observed that the measured spectral peak is linear to the target range, which confirms the functionality of the front-end for radar application. The radar range resolution, which is defined as the minimum distance between two targets that radar can discern, could be measured with a radar signal processing unit.
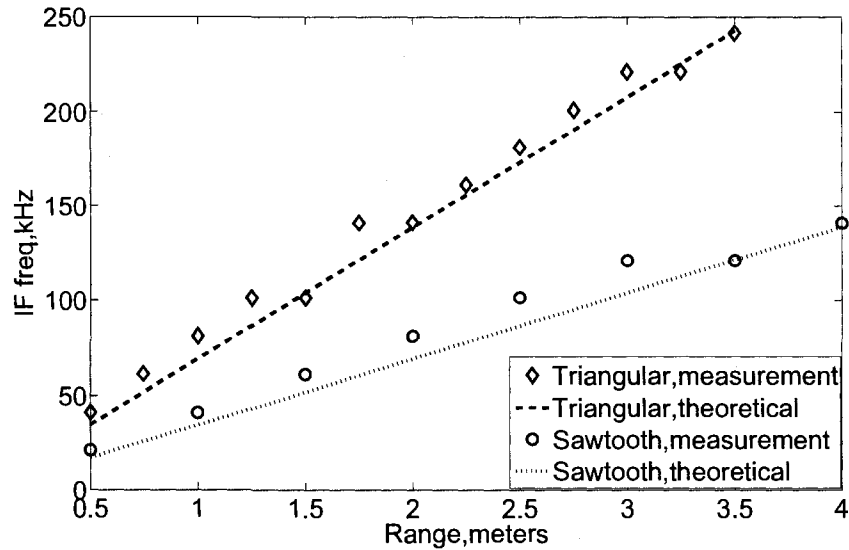
Figure 5-19. Measured IF frequency as a function of range using different modulation techniques.

During the range measurement experiments, it is found that the spectra of the range response are sensitive to the movement of the target, i.e. limited changes on the movement of the target can have an impact on the shape of the range response. This can be explained by considering the range response in time domain [67] which is written as

$$
\begin{aligned}
v = \frac{a_0}{2}\cos 2\pi f_0 \tau + \cos 2\pi f_0 \tau \cdot \sum_{k=1}^{\infty} a_{2k} \cos[2\pi(2k)f_m t - \pi(2k)f_m \tau] \\
+ \sin 2\pi f_0 \tau \cdot \sum_{k=1}^{\infty} a_{2k-1} \cos[2\pi(2k-1)f_m t - \pi(2k-1)f_m \tau]
\end{aligned}
$$

(5.9)

It is important to pay attention to the side lobes amplitude modulation terms $\cos 2\pi f_0 \tau$ and $\sin 2\pi f_0 \tau$, because the two terms can have different effects on the side lobe levels which will have a direct impact on the range response spectrum shape [67]. For example, for a range gate 8, the spectrum lines are distributed in several adjacent lines as shown below when $\cos 2\pi f_0 \tau = 0$ and $\sin 2\pi f_0 \tau = 1$.
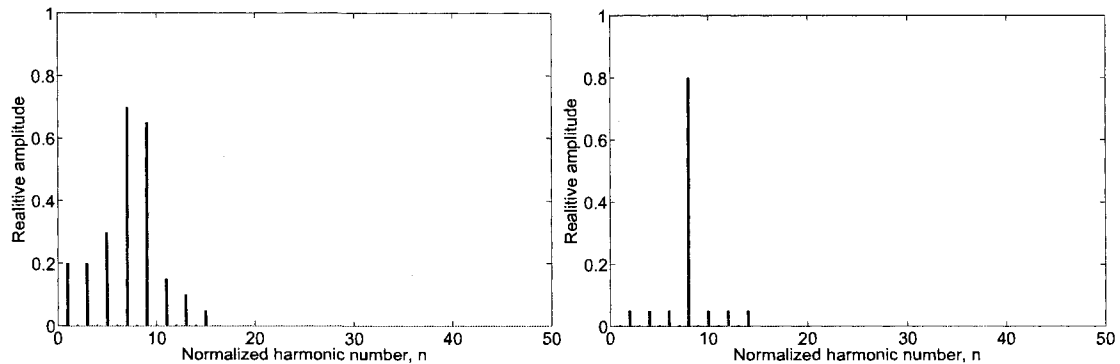
a). $\cos 2\pi f_0 \tau = 0, \sin 2\pi f_0 \tau = 1$ b). $\cos 2\pi f_0 \tau = 1, \sin 2\pi f_0 \tau = 0$

Figure 5-20. Effect of RF phase on typical post mixing spectra (from [67]).

If the two amplitude modulation terms are changed into $\cos 2\pi f_0 \tau = 1$ and $\sin 2\pi f_0 \tau = 0$, i.e. $\Delta\varphi = \pi/2$ then the demodulated signal spectrum can be concentrated into only one or at most a few spectrum lines. That is to say, if there was a target range perturbation, which causes the $2\pi f_0 \cdot \Delta\tau$ item a $\pi/2 + n\pi$ phase change, significant change of the look of the range response would happen. The minimum range perturbation then can be concluded as

$$2\pi f_0 \cdot \Delta\tau = \frac{\pi}{2} \Rightarrow \Delta\tau = \frac{\lambda_0}{8} \cdot \frac{2}{c} = \frac{2 \cdot \Delta R}{c} \tag{5.10}$$

where $\Delta R = \lambda_0/8$.

At 24 GHz, the quantity $\lambda_0/8$ is approximately 1.6 mm. In other words, range perturbations in the order of millimeters can have an impact on the looking of the observed demodulated signal spectrum.

5.5 Integration FMCW Radar with Spread-Spectrum Radar

Research activities on the use of different radar waveforms in a radar system in order to achieve different range resolutions in different applications are carried for a long time [26, 75-78]. FMCW waveform including linear frequency modulation, sine-wave modulation, dual modulation and FSK waveform can share a same front-end system as in [79]. Recently, many efforts are put in the development of spread-spectrum radar trying to achieve better range resolution [80].

If one takes a look at (5.2), the instantaneous transmitted signal is written as

$$v(t) = \cos[2\pi f_0 t + 2\pi M \int_{-\infty}^{t} f(x)dx] \tag{5.11}$$

The auto-correlation function of the transmitted signal is [67]

$$\psi(\tau) = \lim_{T \to \infty} \frac{1}{T} \int_{-T/2}^{T/2} \cos[2\pi f_0 t + 2\pi M \int_{-\infty}^{t} f(x)dx] \cdot$$

$$\cos[2\pi f_0(t+\tau) + 2\pi M \int_{-\infty}^{t+\tau} f(x)dx]dt$$

$$= \lim_{T \to \infty} \frac{1}{2T} \int_{-T/2}^{T/2} \cos[2\pi f_0 \tau + 2\pi M \int_{t-\tau}^{t} f(x)dx]dt \tag{5.12}$$

The similarity of equations (5.8) and (5.12) reveals the autocorrelation essence of FMCW radar. Therefore, integrating the front-end of spread spectrum radar and FMCW radar together is straightforward. A schematic block diagram is given in Figure 5-21 for a descriptive explanation. The radar signal processing mode changes could be made with the replacement of a spread-spectrum signal generator by a frequency modulation (FM) signal generator, which can be achieved using a currently widely available multifunction direct digital synthesizer. In this sense, radar systems with different signal processing

method can be realized with the same front-end platform by choosing different configurations of the digital synthesizer and we may call this radar "software defined" [28].
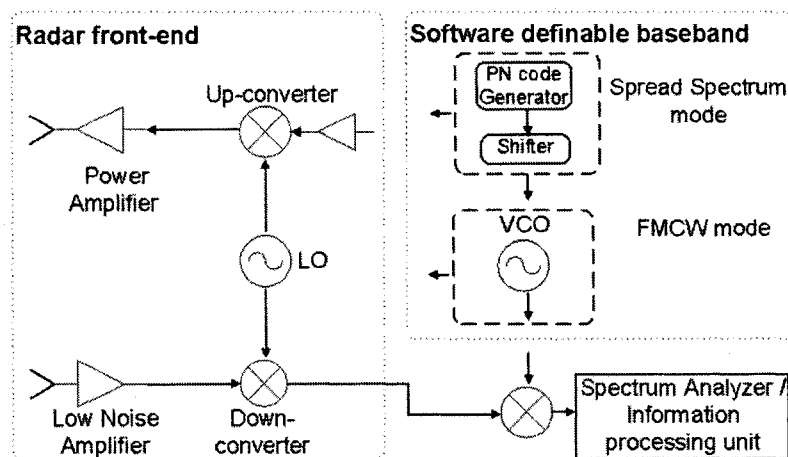
Figure 5- 21. A block diagram for a FMCW/Spread-spectrum radar.

CONCLUSION AND FUTURE WORK

A complete FMCW radar front-end system-on-substrate (SoS) has been designed, fabricated and characterized. This is the first integrated system prototype based on the substrate-integrated-circuit (SIC) concept. It is the first original contribution of this work. The direct technical merit of this contribution is that it has demonstrated that a complete front-end system-on-substrate can be fabricated in one process which is compatible with a conventional PCB fabrication process. By doing so, the microwave system front-end part can achieve a very compact profile as well as a much lower fabrication cost.

The adopted hybrid integration approach, the so-called substrate-integrated-circuits, has proven its usefulness in the design of high performances MICs, as demonstrated by the designed antennas, power dividers, and mixers in this work. One member of the SIC family, i.e. substrate integrated waveguide (SIW) has been widely used for prototypes. Although a geometrical similar structure, as called post-wall or laminated waveguide, was reported earlier, the development of SIW integration technology has progressed beyond its original scope. As a matter of fact, substrate-integrated-circuits design is an advanced organic design philosophy which has self-evolved much further than a mere design concept.

It is concluded that superior MICs performances can be achieved by hybrid integration of different geometries and structures, such as non-planar classic metallic waveguide, and planar microstrip lines through a coherent fabrication manner. A

proposed 180-degree SICs mixer demonstrates that overall performances of such a hybrid MIC are optimized compared with MICs designed with a single waveguiding structure. The easiness of integration with diodes and small size associated with microstrip lines, were integrated together with the lower transmission losses of the SIW, especially at high frequency bands. That is the second original contribution of this work.

Also, as a by-product of this work, the third original contribution is a measurement technique, by which nonlinear characteristic of frequency conversion devices can be measured using a network analyzer.

Although a complete integrated FMCW radar front-end was implemented in this work, there are still many improvements that can be made. For example, a detailed noise analysis, especially the transfer of phase noise from transmitter to the receiver, is desired but not studied because of the limited time frame. This is of course left as a future work in this area.

There are also other directions on the implementation of integrated system on substrate. Although only SIW has been extensively used in this work, the possibilities of integrating other guiding wave structures on the same substrate are enormous. In fact, a good SIC system design is not (and should not) limited to a single guiding wave structures. Areas of future SIC related research areas including:

· Development of semiconductor substrate based high performance SIC components and devices, with the ultimate objective of synthesizing SIC components on a silicon or GaAs substrate. This will enable the large scale manufacturing of high-quality passive

and active microwave integrated circuits and calls for the maturation of monolithic semiconductor processing techniques.

· A complex versatile SoS combining different SIC family members including substrate integrated non-radiating dielectric guide, substrate integrated waveguide, substrate integrated image dielectric guide, to name a few, and classic planar structures such as microstrip lines, coplanar waveguide and so on, with different building blocks exemplified by their unique capabilities, shall be pursued to demonstrate the usefulness of this integration methodology.

REFERENCES

[1]   P. Staecker, "Microwave industry outlook - overview," *IEEE Transactions on Microwave Theory and Techniques,* vol. 50, no. 3, pp. 1034-1036, Mar. 2002.

[2]   H. Sobol, "Microwave industry outlook - microwaves for telecommunication systems," *IEEE Transactions on Microwave Theory and Techniques,* vol. 50, no. 3, pp. 1037-1038, Mar. 2002.

[3]   D. Parker, "Microwave industry outlook - defense applications," *IEEE Transactions on Microwave Theory and Techniques,* vol. 50, no. 3, pp. 1039-1041, Mar. 2002.

[4]   H. H. Meinel, "Commercial applications of millimeterwaves history, present status, and future trends," *IEEE Transactions on Microwave Theory and Techniques,* vol. 43, pp. 1639-1653, 1995.

[5]   H. H. Meinel, "Millimeter-wave technology advances since 1985 and future trends," *IEEE Transactions on Microwave Theory and Techniques,* vol. 39, no. 5, pp. 759-767, May. 1991.

[6]   E. C. Niehenke, R. A. Pucel, and I. J. Bahl, "Microwave and millimeter-wave integrated circuits," *IEEE Transactions on Microwave Theory and Techniques,* vol. 50, no. 3, pp. 846-857, Mar. 2002.

[7]   K. W. Chang, H. Wang, G. Shreve, J. G. Harrison, M. Core, A. Paxton, M. Yu, C. H. Chen, and G. S. Dow, "Forward-looking automotive radar using a W-band single-chip transceiver," *IEEE Transactions on Microwave Theory and Techniques,* vol. 43, no. 7, pp. 1659-1668, July. 1995.

[8]   A. Tessmann, S. Kudszus, T. Feltgen, M. Riessle, C. Sklarczyk, and W. H. Haydl, "Compact single-chip W-band FMCW radar modules for commercial high-resolution sensor applications," *IEEE Transactions on Microwave Theory and Techniques,* vol. 50, no. 12, pp. 2995-3001, Dec. 2002.

[9]   K. Wu, "Integration and interconnect techniques of planar and non-planar structures for microwave and millimeter-wave circuits - Current status and future trend," in *Asia-Pacific Microwave Conference Proceedings, APMC,* Taipei, 2001, pp. 411-416.

[10]   K. Wu and F. Boone, "Guided-wave properties of synthesized non-radiative dielectric waveguide for Substrate Integrated Circuits (SICS)," in *IEEE MTT-S International Microwave Symposium Digest,* Phoenix, AZ, 2001, pp. 723-726.

[11]   K. Wu, D. Deslandes, and Y. Cassivi, "The substrate integrated circuits-a new concept for high-frequency electronics and optoelectronics," in *Proc. 6th Int. Telecommunications in Modern Satellite, Cable and Broadcasting Service,* 2003, pp. P-III-P-X.

[12]   K. Wu, "The substrate integrated circuits (SICs) – a new generation of RF and millimeter-wave integrated circuits," in *Asia-Pacific Microwave Conference Proceedings, APMC,* New Delhi, 2004.

[13]   Y. Cassivi and K. Wu, "Low cost microwave oscillator using substrate integrated waveguide cavity," *IEEE Microwave and Wireless Components Letters,* vol. 13, no. 2, pp. 48-50, Feb. 2003.

[14] D. Deslandes and K. Wu, "Single-substrate integration technique of planar circuits and waveguide filters," *IEEE Transactions on Microwave Theory and Techniques,* vol. 51, no. 2, pp. 593-596, Feb. 2003.

[15] Y. Cassivi and K. Wu, "Substrate integrated NRD (SINRD) guide on high dielectric constant substrate for millimeter wave circuits and systems," in *IEEE MTT-S International Microwave Symposium Digest,* Fort Worth, TX, United States, 2004, pp. 1639-1642.

[16] Y. Cassivi and K. Wu, "Substrate Integrated Nonradiative Dielectric Waveguide," *IEEE Microwave and Wireless Components Letters,* vol. 14, no. 3, pp. 89-91, Mar. 2004.

[17] D. Deslandes and K. Wu, "Integrated microstrip and rectangular waveguide in planar form," *IEEE Microwave and Wireless Components Letters,* vol. 11, no. 2, pp. 68-70, Feb. 2001.

[18] D. Deslandes and K. Wu, "Accurate modeling, wave mechanisms, and design considerations of a substrate integrated waveguide," *IEEE Transactions on Microwave Theory and Techniques,* vol. 54, no. 6, pp. 2516-2526, June. 2006.

[19] A. Patrovsky and K. Wu, "Substrate Integrated Image Guide (SIIG) - A planar dielectric waveguide technology for millimeter-wave applications," *IEEE Transactions on Microwave Theory and Techniques,* vol. 54, no. 6, pp. 2872-2879, June. 2006.

[20] F.Shigeki, "Waveguide line," Japan Patent, 06-053 711 Feb. 25, 1994

[21] K. Wu, "Towards system-on-substrate approach for future millimeter-wave and photonic wireless applications," in *Asia-Pacific Microwave Conference Proceedings, APMC*, Japan, Dec. 2006, pp. 1895-1900.

[22] H. H. Meinel, "Applications of microwaves and millimeterwaves for vehicle communications and control in Europe," in *IEEE MTT-S International Microwave Symposium Digest*, Albuquerque, NM, USA, 1992, pp. 609-612.

[23] M.I.Skolnik, *Introduction to Radar Systems*, 2nd ed. New York: McGraw-Hill, 1962.

[24] I.V.Komarov and S.M.Smolskiy, *Fundamentals of Short-Range FM Radar*. Boston: Artech House, 2003.

[25] J. Wenger, "Automotive radar - status and perspectives," in *IEEE Compound Semiconductor Integrated Circuit Symposium*, Palm Springs, CA, USA, 2005, p. 4 pp.

[26] R. Schneider and J. Wenger, "System aspects for future automotive radar," in *IEEE MTT-S International Microwave Symposium Digest*, Anaheim, CA, USA, 1999, pp. 293-6.

[27] M. E. Russell, C. A. Drubin, A. S. Marinilli, M. J. Del Checcolo, and W. Gordon Woodington, "Integrated automotive sensors," *IEEE Transactions on Microwave Theory and Techniques,* vol. 50, no. 3, pp. 674-677, Mar. 2002.

[28] Z. Li and K. Wu, "24 GHz radar front-end for FMCW and spread spectrum radar applications," in *IEEE Radio and Wireless Symposium Digest*, San Diego, CA, USA, 2006, pp. 351-354.

[29] Z.-L. Li, K. Wu, and T. A. Denidni, "A new approach to integrated horn antenna," in *Proc. Intl Symp. on Antenna Technology and Applied Electromagnetics*, Ottawa, Canada, 2004, pp. 535-538.

[30] Z. Li, X. Chen, and K. Wu, "A Surface Mountable Pyramidal Horn Antenna and Transition to Substrate Integrated Waveguide," in *Signals, Systems and Electronics, 2007. ISSSE '07. International Symposium on*, 2007, pp. 607-610.

[31] Z. Li and K. Wu, "24GHz FMCW radar front-end system on substrate," in *IEEE Radio and Wireless Symposium Digest*, Long Beach, CA, USA, 2007, pp. 233-236.

[32] Z. Li and K. Wu, "On the leakage of FMCW radar front-end receiver," in *Global Symposium on Millimeter Waves*, China,Nanjing, 2008, pp. 127-130.

[33] J.Laskar, B.Matinpour, and S.Chakraborty, *Modern Receiver Front-Ends: Systems, Circuits, and Integration*. Hoboken, N.J: Wiley-Interscience, 2004.

[34] Hittite, "Mixer spur chart calculator," www.hittite.com.

[35] A.E.Bailey, *Microwave measurement*, 2nd. ed. UK:London: Peter Peregrinus Ltd., 1985.

[36] W.F.Egan, *Practical RF System Design*. Hoboken, N.J.: Wiley-IEEE Press, 2003.

[37] Q. Gu, *RF System Design of Transceivers for Wireless Communications*: Springer, 2005.

[38] B.Razavi, *RF Microelectronics*. Upper Saddle River, NJ: Prentice Hall, 1998.

[39] S.A.Maas, "Third-order intermodulation distortion in cascaded stages," *IEEE Microwave and Guided Wave Letters,* vol. 5, no. 6, pp. 189-191, June. 1995.

[40]   J.Tsui, *Microwave receiver and related components*: Peninsula, 1986.

[41]   W.L.Stutzman and G.A.Thiele, *Antenna Theory and Design*, 2nd ed. New York: J.Wiley, 1998.

[42]   A. D. Yaghjian, "Approximate formulas for the far field and gain of open-ended rectangular waveguide," *IEEE Transactions on Antennas and Propagation,* vol. AP-32, no. 4, pp. 378-384, Apr. 1984.

[43]   R.E.Collin, *Foundations for Microwave Engineering*, 2nd ed. New York: McGraw-Hill, 1992.

[44]   S.B.Cohn, "Optimum design of stepped transmission-line transformers," *IRE Transactions on Microwave Theory and Techniques,* vol. MTT-3, no. 3, pp. 16-21, Mar. 1955.

[45]   L.Yan, H. Wei, H. Guang, J. Chen, K. Wu, and T.-J. Cui, "Simulation and experiment on SIW slot array antennas," *Microwave and Wireless Components Letters, IEEE,* vol. 14, no. 9, pp. 446-448, Sept. 2004.

[46]   R. V. Gatti, R. Sorrentino, and M. Dionigi, "Equivalent circuit of radiating longitudinal slots in dielectric filled rectangular waveguides obtained with FDTD method," in *IEEE MTT-S International Microwave Symposium Digest*, Seattle, WA, 2002, pp. 871-874.

[47]   R.S.Elliott and L.A.Kurtz, "Design of small slot arrays," *IEEE Transactions on Antennas and Propagation,* vol. AP-26, no. 2, pp. 214-219, Feb. 1978.

[48] R.S.Elliott, "Improved design procedure for small arrays of shunt slots," *IEEE Transactions on Antennas and Propagation,* vol. AP-31, no. 1, pp. 48-53, Jan. 1983.

[49] A.F.Stevenson, "Theory of slots in rectangular wave-guides," *Journal of Applied Physics,* vol. 19, pp. 24-38, 1948.

[50] A. J. Sangster and A. H. I. McCormick, "Theoretical design/synthesis of slotted waveguide arrays," *IEE Proceedings, Part H: Microwaves, Antennas and Propagation,* vol. 136, pp. 39-46, 1989.

[51] R. S. Elliott, *Antenna Theory and Design.* Hoboken, N.J.: John Wiley & Sons, 2003.

[52] S.A.Mass, *Microwave Mixers,* 2nd ed. Boston: Artech House, 1993.

[53] S.A.Mass, *Noise in Linear and Nonlinear Circuits.* Boston: Artech House, 2005.

[54] "Beam lead Schottky diodes for mixers and detectors (1-26 GHz)," Agilent data sheet.

[55] M.-Y.Chen, F.-Y.Xu, and K.-Y.Zhao, *Electromagnetism and Microwave Technology (in Chinese).* Beijing: High-Education Publishing House, 1989.

[56] R.Levy, "Improved single and multi-aperture waveguide coupling theory, including explanation of mutual interactions," *IEEE Transactions on Microwave Theory and Techniques,* vol. MTT-28, pp. 331-338, 1980.

[57] P.Rizzi, *Microwave Engineering--Passive Circuits.* Englewood Cliffs, N.J.: Prentice Hall, 1987.

[58]   J.-X.Chen, W.Hong, Z.-C.Hao, H.Li, and K.Wu, "Development of a low cost microwave mixer using a broad-band Substrate Integrated Waveguide (SIW) coupler," *IEEE Microwave and Wireless Components Letters,* vol. 16, no. 2, pp. 84-86, Feb. 2006.

[59]   W. Van Moer and Y. Rolain, "Proving the Usefulness of a Three-Port Nonlinear Vectorial Network Analyzer Through Mixer Measurements," *IEEE Transactions on Instrumentation and Measurement,* vol. 52, no. 6, pp. 1834-1837, June. 2003.

[60]   "Series 37xxxC vector network analyzer operation manual," Anritsu, Morgan Hill, CA: Available online: www.anritsu.com.

[61]   "Measuring frequency conversion devices," in *Application Note* Anritsu, Morgan Hill, CA: Available online: www.anritsu.com.

[62]   R.J.King, *Microwave Homodyne System.* England: Peter Peregrinus Ltd, 1978.

[63]   B. L. Lewis, F. F. Kretschmer, and W. W. Shelton, *Aspects of Radar Signal Processing.* Norwood, Mass: Artech House, 1986.

[64]   B. D. Steinberg, *Modern Radar Analysis, Evaluation and System Design.* New York: John Wiley & Sons, 1965.

[65]   H. D. Griffiths, "New ideas in FM radar," *Electronics & Communication Engineering Journal,* vol. 2, pp. 185-194, Oct. 1990.

[66]   M.I.Skolnik, *Radar Handbook,* 2nd ed. New York: McGraw-Hill, 1989.

[67]   L.M.Tozzi, "Resolution in frequency-modulated radars," in *Electrical Engineering.* Ph.D. thesis College Park: University of Maryland, 1972.

[68]   F. J. O'Hara and G. M. Moore, "High performance CW receiver using feedthru nulling," *Microwave Journal,* vol. 6, pp. 63-71, 1963.

[69]   P. D. L. Beasley and A. G. Stove, "Pilot-an example of advanced FMCW techniques" in *High Time-Bandwidth Product Waveforms in Radar and Sonar, IEE Colloquium on,* 1991, pp. 10/1-10/5.

[70]   K. Lin, K. Lin, Y. E. Wang, C. K. Pao, and Y. C. A. S. Y. C. Shih, "A Ka-Band FMCW Radar Front-End With Adaptive Leakage Cancellation," *Microwave Theory and Techniques, IEEE Transactions on,* vol. 54, pp. 4041-4048, 2006.

[71]   S. Wang, H.-S. Wu, C.-H. Chang, and T. C. K. C., "Modeling and suppressing substrate coupling of RF CMOS FMCW sensor incorporating synthetic quasi-TEM transmission lines," in *IEEE MTT-S International Microwave Symposium Digest,* Honolulu, HI, USA, 2007, pp. 1939-42.

[72]   Z. Li and K. Wu, "24-GHz Frequency-Modulation Continuous-Wave Radar Front-End System-on-Substrate," *IEEE Transactions on Microwave Theory and Techniques,* vol. 56, no. 2, pp. 278-285, Feb. 2008.

[73]   J. Fuchs, K. D. Ward, M. P. Tulin, and R. A. York, "Simple techniques to correct for VCO nonlinearities in short range FMCW radars," in *IEEE MTT-S International Microwave Symposium Digest,* San Franscisco, CA, USA, 1996, pp. 1175-1178.

[74]   B. K. Kang, H. J. Kwon, B. K. Mheen, H. J. Yoo, and Y. H. Kim, "Nonlinearity compensation circuit for voltage-controlled oscillator operating in linear

frequency sweep mode," *IEEE Microwave and Guided Wave Letters,* vol. 10, no. 12, pp. 537-539, Dec. 2000.

[75] M. Roberton and E. R. Brown, "Integrated radar and communications based on chirped spread-spectrum techniques," in *IEEE MTT-S International Microwave Symposium Digest,* Philadelphia, PA, USA, 2003, pp. 611-14.

[76] H. D. Griffiths and W. D. Bradford, "Digital Generation of Wideband FM Waveforms for Radar Altimeters," in *IEE Conf. Radar,* 1987, pp. 325-329.

[77] W. K. Saunders, "Velocity-aided range acquisition and tracking in dual-mode CW/FM-CW radar," in *IEE Radar,* London, 1989, p. vol.4.

[78] M. Barrett, "An X-Band FM-CW Navigation Radar," in *IEE Radar,* London, 1987, pp. 448-452.

[79] M.M.Meinecke and H.Rohling, "Combination of LFMCW and FSK modulation principles for automotive radar systems," in *German Radar Symposium Digest,* Berlin, Germany, 2000.

[80] Y.Aoyagi, T.Fukuchi, H.Endo, M.Kusunoki, Y.Iso, K.Inoue, H.Ishizu, and R.Kohno, "76 GHz spread spectrum radar for autonomous intelligent cruise control," in *IEEE Conference on Intelligent Transportation Systems, Proceedings, ITSC,* Boston, MA, USA, 1997, pp. 677-680.